Investigation of microwave imaging and local dielectric characterization of materials by using a homemade interferometer-based near-field microwave microscope

Tianjun Lin

L'UNIVERSITE DE LILLE - FACULTE SCIENCES ET TECHNOLOGIES

Thèse

pour obtenir le grade de

Docteur de l'Université des sciences et technologies de Lille

Spécialité Electronique, microélectronique, nanoélectronique et micro-ondes

Présentée par

Tianjun LIN

INVESTIGATION OF MICROWAVE IMAGING AND LOCAL DIELECTRIC CHARACTERIZATION OF MATERIALS BY USING A HOMEMADE INTEFEROMETER-BASED NEAR-FIELD MICROWAVE MICROSCOPE

Soutenance prévue le 26 avril 2018 devant la commission d'examens

Hamid KOKABI	Professeur Sorbonne Universités	Rapporteur
Valérie VIGNERAS	Professeur ENSCBP Bordeaux	Rapporteur
Denis REMIENS	Professeur Université de Valenciennes	Examinateur
Marjorie GRZESKOWIAK	MCF Université Paris-Est	Examinateur
Pierre-Yves CRESSON	MCF Université d'Artois	Examinateur
Tuami LASRI	Professeur Université de Lille	Directeur de thèse

Acknowledgements

First, I would like to thank Mr Lionel BUCHAILLOT, Director of Institut d'Electronique de Microélectronique et de Nanotechnologie (IEMN) for having welcomed me into the laboratory.

I would like to express my deep and sincere appreciation to my advisor, Mr Tuami LASRI, Professor at University of Lille 1 and director of the SPI doctoral school at Lille 1, for providing me this PhD opportunity. It has been an honor to be his PhD student. I am really grateful for his patience, kindness, motivation and excellence guidance. The joy and enthusiasm he has for his research was contagious and motivational for me, even during tough times in the PhD pursuit.

Besides my advisor, I would like to thank my thesis committee, Mrs Valérie VIGNERAS, Professor at ENSCBP Bordeaux, and Mr Hamid KOKABI, Professor at Sorbonne University, for their insightful comments and suggestions. My thanks also go to Mr. Denis REMIENS, Professor at University of Valenciennes, Mr. Pierre-Yves CRESSON, Maitre de conférences at University of Artois, and Mrs Marjorie GRZESKOWIAK, Maitre de conférences at University of Paris-Est for having accepted to examine my work.

I would like to thank all the MITEC members for giving me the benefit of their relevant remarks and their knowledge. Especially, I would like to express my thanks to Sijia GU, for his help, support and advice. We had many interesting discussions in calculations and measurements. Without his precious encouragement it would have been difficult to conduct this research.

I would also like to express my gratitude to my colleagues, Ghizlane, Nadine, Hind, Amine, Soufiane, Louis, Abdallah, Abdel and Zahir, for the help they have given me and for their sympathy and friendship. It is a very nice experience to work with them.

I am also grateful to all my friends, Ma Enze, Zhang Tianchen, Zhu Tianqi, Li Shuo, Hao Jianping, Ding Xiaokun, Wei wei, Zhou Di, Du Yu, Chen Shiqi, Xu Tao, Li sizhe, Jiang Zhifang and et al. Unfortunately I cannot thank them all individually here, but be assured of my gratitude for all the good times spent together.

Last but not the least, I would like to thank my family for all their love and encouragement. For my parents who raise me with a love of science and supported me in all my pursuits. And most of all for my Ying, I am really appreciate for her understanding and faithful support during this PhD. Thank you.

Tianjun LIN

Mai 2018

Outline

List of figures

CHAPTER I

CHAPTER II

CHAPTER III

CHAPTER IV

List of tables

List of acronyms and abbreviations

ADC: ANALOG-TO-DIGITAL CONVERTER

ADS: ADVANCED DESIGN SYSTEM

AFM: ATOMIC FORCE MICROSCOPE

CMOS: COMPLEMENTARY METAL OXIDE SEMICONDUCTOR

DNA: DEOXYRIBONUCLEIC ACID

DSP: DIGITAL SIGNAL PROCESSOR

DUT: DEVICE UNDER TEST

EMP: EVANESCENT MICROWAVE PROBE

FWHM: FULL WIDTH AT HALF MAXIMUM

HFSS: HIGH FREQUENCY STRUCTURE SIMULATOR

IBMN: INTERFEROMETER BASED MATCHING NETWORK

IC: INTEGRATED CIRCUIT

IOT: INTERNET OF THINGS

IFBW: INTERMEDIATE FREQUENCY BANDWIDTH

INFMM: INTERFEROMETER-BASED NEAR FIELD MICROWAVE MICROSCOPE

LO: LOCAL OSCILLATOR

MEMS: MICRO-ELECTRO-MECHANICAL SYSTEM

MOS: METAL-OXIDE-SEMICONDUCTOR

NFMM: NEAR-FIELD MICROWAVE MICROSCOPE

NSOM: NEAR-FIELD SCANNING OPTICAL MICROSCOPE

SEM: SCANNING ELECTRON MICROSCOPE

SMM: SCANNING MICROWAVE MICROSCOPE

SPM: SCANNING PROBE MICROSCOPE

SRR: SPLIT RING RESONATOR

STM: SCANNING TUNNELING MICROSCOPE

VNA: VECTOR NETWORK ANALYZER

General introduction

Microelectronic technology covers almost every aspect of our lives, including consumer electronics, communications, computer-aided technologies and robotics. It also results in the incorporation of electronic devices into equipment specific to each industry. The continuous miniaturization of electronic components leads to more economic energy consumption and better performance but also to an increase of the difficulty to characterize them. The development of well-suited characterization means is therefore needed. Naturally, microscopies are considered as good candidates to respond to this requirement as they are known as the solution of choice to visualize small objects which are hard to be observed from naked eyes. However, the conventional optical microscope fails to observe the microscale and nanoscale devices because of the well-known Abbe diffraction limit [ABB 73]. The scanning probe microscope (SPM) has been therefore developed to bypass this resolution limit and leads to a variety of instruments that give spatial resolutions up to the nanometer. Actually, the scanning tunneling microscope (STM), atomic force microscope (AFM) and scanning electron microscope (SEM) are widely used in industrial and academic laboratories today. In fact, the microscopes mentioned above are characterization tools for materials surface vision. Sub-surface characterization such as subsurface biological anomalies imaging and more generally buried structures characterization cannot be realized. Thus, there is a strong need for new characterization tools to address these ever growing demands of instruments of high spatial resolution and multi-functionalities.

The near-field microwave microscope (NFMM) seems to meet all these requirements and is considered at the forefront of science and technology today because it combines the potentials of scanning probe microscope with the power of microwave sensing methods. Benefitting from the material penetration ability brought by the microwaves, non-destructive subsurface evaluation and materials properties (structural, topographic, electronic and magnetic) characterization become possible. The NFMM is based on the interaction between the material properties and the electromagnetic fields emitted by an evanescent microwave probe (EMP). To guaranty the high resolution of the NFMM, both

the probe dimensions and the probe to sample distance have to be much smaller than the free-space wavelength.

In this PhD work the main goal is to address applications in surface imaging, subsurface imaging and material properties measurement by means of a homemade NFMM.

The manuscript is made of four chapters. The first one is an introduction to the state of art of NFMM, where typical features, advantages and limitations are described. Applications including its ability in surface and subsurface imaging as well as its access to the samples under test physical properties are also illustrated. After that, a classical NFMM set-up is described. All the components including the signal generation system, the scanner and the data acquisition system are depicted. To address the sensitivity limitation, two of the most popular matching networks are described in details. We show that according to various types of probes, different applications at selected operating frequencies can be achieved.

In chapter II, a brief description of the NFMM developed at IEMN is firstly given. We show that thanks to an interferometer based matching network, the sensitivity limitation is bypassed and the system is able to operate at any frequency in the working frequency band [2-18 GHz]. The setting parameters are also studied and their influence on the measurement precision is estimated. The homemade interferometer-based NFMM (iNFMM) imaging performance is then evaluated both in surface and subsurface situations. Examples of 1D and 2D images are given to appreciate the strengths and weaknesses of the technique proposed. To improve the image quality, image treatment techniques such as position/signal difference method, adaptive robust statistic method and local regression, likelihood method are applied on raw images collected by the iNFMM.

To demonstrate that our homemade iNFMM owns the broad working frequency band feature, high measurement sensitivity and precision, we focus on the dielectric properties measurement of biological aqueous solutions in chapter III. Firstly, an introduction to different characterization methods to measure the glucose concentration of aqueous solutions is given and a well-established model to determine the complex permittivity of

different concentrations of glucose aqueous solutions is then selected. After that, two investigation modes are respectively presented: immersion mode and non-contact mode. With a careful study of the setting parameters and taking their measurement error rates into account, it is shown that different concentration ranges of glucose aqueous solutions can be characterized according to the two modes. As a demonstration, the dielectric permittivity of glucose aqueous solutions with concentrations ranging from 0 to 10 mg/ml is studied.

After the demonstration of liquids characterization possibility, in chapter IV we focus our attention on the improvement of our iNFMM in terms of integration. The wish to integrate the iNFMM is motivated by its large size and the relatively high cost of the components inside, typically the network analyzer and the impedance tuner. The replacement of the network analyzer is focused here. In fact, the network analyzer has two main functions in the NFMM. The first one is the broadband signal generation with a fixed power level. The second one is the measurement of the signal reflected from the probe with high precision. The signal generation requirement can be easily satisfied. To ensure the signal measurement, a six-port reflectometer can be advantageously envisaged. Compared to the conventional network analyzer, the six-port technique owns a major advantage, which is related to the simplicity of the microwave hardware. In this chapter, a six-port reflectometer configuration is selected to cover the large frequency band targeted [2-20 GHz]. The design procedure, fabrication methods and measurement results are presented and a simple one-port calibration method is also applied on the measurement results to further improve the measurement precision.

Chapter I

A brief description of near-field microwave microscopy

Chapter I : A brief description of near-field microwave microscopy

I.1 Introduction

Smart devices, connected objects or more generally, the Internet of Things (IOT) has become a sunrise industry to facilitate man's daily life and improve the living quality. The sensors, actuators and electronic circuits play a very important role in IOT since they are usually embedded in the objects to exchange data. Thanks to the rapid advances in the microelectronic technology, the miniaturization of electronic components leads to a much less power consumption and much higher performance. For instance, the semiconductor manufacturing processes for the complementary metal oxide semiconductor (CMOS) has been improved a lot for the size of gate from 10 µm in the early 1970s to 7 nm in nowadays. Thus, the difficulties to characterize these components increase. Furthermore, the spring up of new materials such as graphene, borophene, germanene and so on, results in an increasing demand of characterization in particular at the nanoscale. Consequently, to fulfil such requirement, the scanning probe microscope (SPM) is proposed in this general context of downscaling. This characterization mean is regarded as an innovative metrology tool which can answer to a large range of challenges at the nanoscale [TSE 05] [EFI 17].

In fact, the continuous development of SPM leads to a variety of instruments that are able to offer nanometer spatial resolutions. Scanning tunneling microscope (STM) is firstly introduced by G. Bining and H. Rohrer in 1981[BIN 82_a] [BIN 82_b]. By means of the tunneling current between the sample and the probe, it becomes the first one to present surface studies with atomic resolution. Nevertheless, the measurement principle limits its use only to conductors. Insulating samples could not be imaged until the advent of the alternating current STM (AC-STM) in 1989 [KOC 89]. At about the same time in the mid-1980s, the first generation of atomic force microscope (AFM) came up as a combination of a STM and a stylus profilometer (SP) [BIN 86]. The measurement concept focuses on detecting the interatomic or electromagnetic force between the probe tip and the sample surface. Without the limitation brought by the STM, AFM can be applied not only to conductors but also to insulators and semiconductors. Generally speaking, STM and AFM

can both operate in air and liquid conditions and offer a good resolution up to several Å for surface characterization [JUL 93].

Samples physical properties such as conductivity, dielectric constant and dopant intensity are of great interest especially for new materials [GAO 98] [IMT 03] [GU 17]. In addition, sub-surface characterization attracts more and more attention, for example in application fields like defects detection in metals [TAB 99_a], subsurface biological anomalies imaging [WU 04] [GAI 07] [REN 11] and buried structures discovering [HAD 11] [GRA 15] [CHI 12]. Microwave sensing techniques have shown a great potential in these domains thanks to the penetration ability offered which allows a non-destructive subsurface evaluation. In fact, traditional far-field microwave characterization techniques are limited by the low resolution which is in the order of $\frac{\lambda}{2}$ according to Abbe's criterion [ABB 73] [ABB 84]. Facing the increasing resolution requirement in the order of sub-millimetre or even the nanoscale, traditional far-field approach is no longer available. Thus, a method to overcome such resolution restriction is imperative. In 1928, Synge firstly came up with the near-field scanning idea to bypass the Abbe's criterion [SYN 28]. After that, research works have been established to complete this idea and contribute to set the basis of near-field microwave microscopy (NFMM) [FRA 59] [SOO 62] [BRY 65] [ASH 72] [WAN 90] [TAB 99_a]. Recently, the NFMM idea has been included in the atomic force microscope (AFM) and scanning tunnelling microscope (STM) and the AFM/STM based NFMM were therefore developed at the beginning of 21^{th} century [ANG 07] [HAN 08].

With the development of the NFMM from theoretical and application perspectives, it can be considered as an innovative and powerful metrology tool for the study of a large range of materials such as bulk samples [IMT 07], buried structures [WU 04] [PLA 11], thin films [TSE 13] [GU 17], electronic materials and devices [IMT 10] [FEN 11], liquids [GU 16_c] [LIN 17] and biological samples [FAR 12].

In this chapter, we firstly present the typical features including the advantages and limitations of the NFMM. Applications including its ability in surface and subsurface imaging as well as its access to samples' physical properties are also described. After that,

a classical NFMM set-up is under investigation. All the components including the signal generation system, the scanner and the data acquisition system are illustrated. To address the sensitivity limitation, two of the most popular matching networks are described in details. We show that according to various types of probes, different applications at selected operating frequencies can be achieved. Finally, we present a homemade interferometer-based NFMM developed in MITEC (Microtechnology and Instrumentation for Thermal and Electromagnetic Characterization) group [Bak 15] [GU 16_c].

I.2 NFMM features and applications

I.2.1 Introduction

As just mentioned in the introduction of the chapter, different kinds of SPM exist that can offer a spatial resolution up to several Å. However, most of them can only evaluate samples surface profile while the subsurface properties remain a challenge. Adversely, NFMM gives the possibility to characterize quantitatively the subsurface properties of the sample thanks to the penetration ability offered by microwaves. Actually, parameters such as the reflection coefficient, the transmission coefficient or the capacitance can be translated into different materials properties including dielectric constant, conductivity, characteristic impedance and so on, with a proper physical model. In the following sections, we firstly present the subsurface imaging ability brought by the NFMM. After that, materials properties determined from two approaches (semi-empirical method and probe-sample interaction method) are illustrated. The limitations of NFMM are discussed thereafter and finally a conclusion is given.

I.2.2 Subsurface imaging

As already said, the NFMM exhibits a pronounced advantage compared to the other types of SPM, thanks to the interrogating waves that have the ability to penetrate through materials and reflect the subsurface properties. Indeed, this phenomena relies on the fact that the embedded structures show different characteristic impedances compared to the cover layer. They interact with the microwave signal and affect its magnitude and phase

features. This can be observed for example by measuring the reflection coefficient in terms of amplitude and phase shift [TAB 04]. As a result, the NFMM can be used in several applications which have been briefly summarized in the introduction.

In order to better understand the subsurface imaging performance brought by the NFMM, a demonstration is given for a doped Si substrate that is partly covered by thin SiO_2 films.

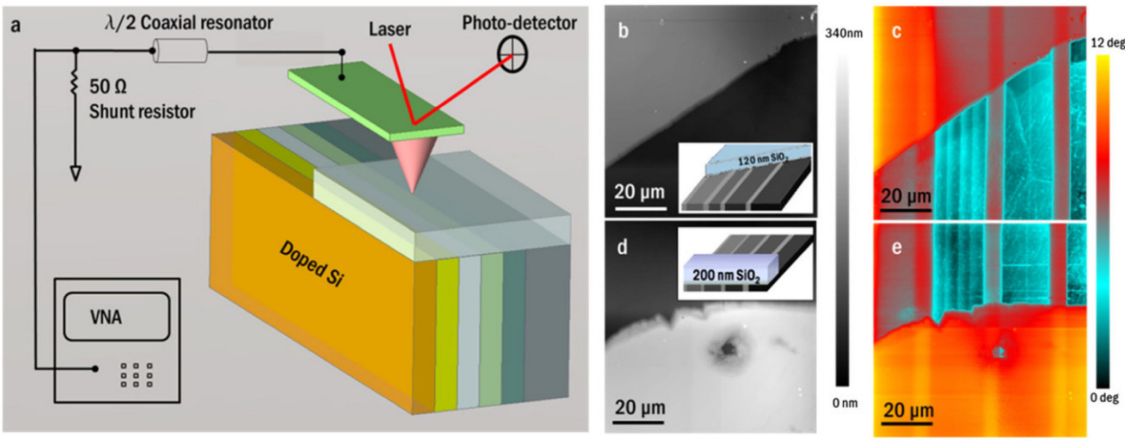

Figure I-1: Schematic of subsurface detection towards a doped Si substrate partly covered by SiO_2 films [GRA 15].

As illustrated in Figure I-1.a, the NFMM is build up with a vector network analyzer (VNA) and a commercial AFM. The sample under test is a flat doped Si substrate which consists of dopant stripes with different dopant density. SiO_2 films with two thicknesses (120 nm and 200 nm) are respectively placed on the dopant stripes to verify their influence on the measurement results (Figure I-1.b and Figure I-1.d). The reflection coefficient in terms of phase shift is therefore obtained in Figure I-1.c (120 nm) and Figure I-1.e (200 nm). One can note that the dopant stripes are clearly detected even with the oxide coverage.

Nevertheless, the measured sensitivity between the first and second dopant stripes decreases with the increase of the SiO_2 layer thickness. This phenomena gives rise to a discussion: what is the relationship between the measurement sensitivity and the thickness of the cover layer? To answer this question, Sun et al have designed an experiment to evaluate the influence of covers on the subsurface imaging quality [SUN 14].

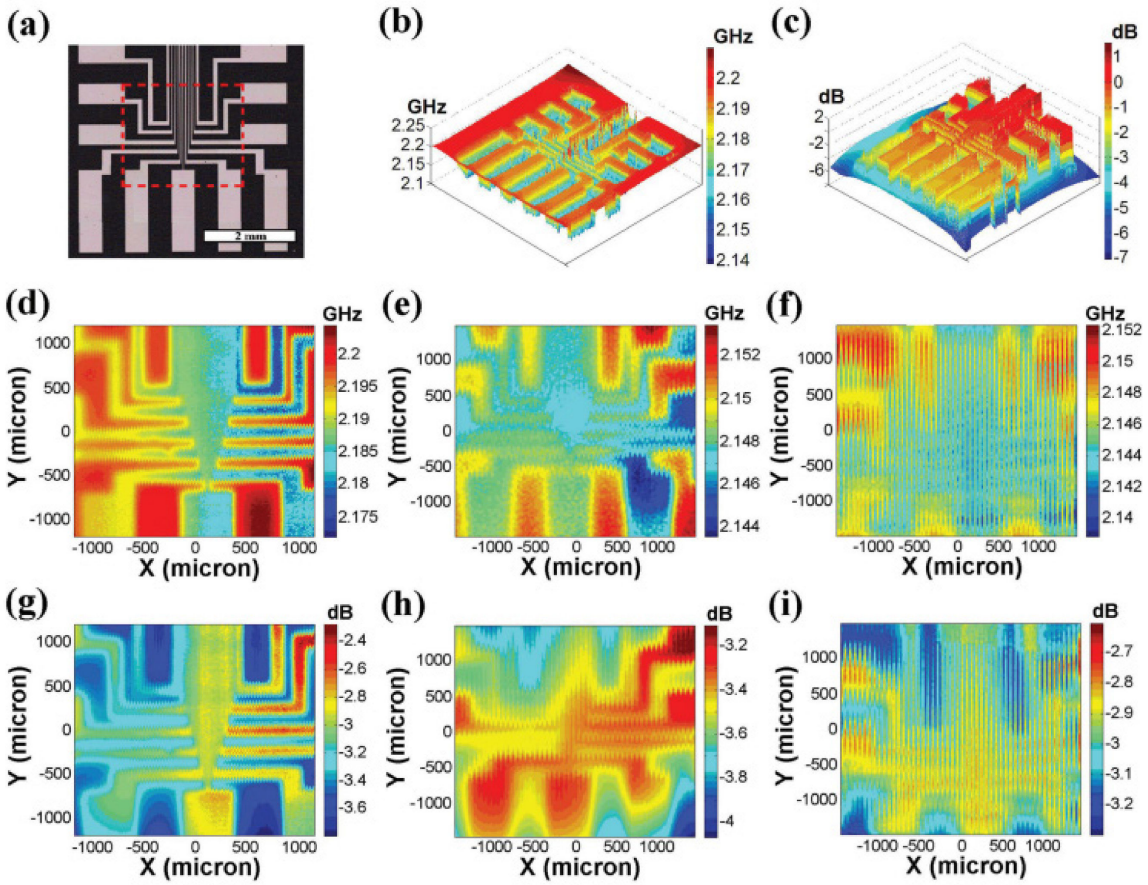

Figure I-2: Subsurface imaging results of a 100 nm thick gold thin film pattern on a glass substrate with different cover thicknesses ranging from 0 to 50 µm [SUN 14].

In this experimentation, the tip apex size is around 50 µm and the tip-sample distance is fixed to 10 µm. The optical image of a gold thin film pattern whose thickness is 100 nm is demonstrated in Figure I-2.a. With the NFMM measurement, the contour views of the pattern are shown in terms of resonant frequency and magnitude of the measured reflection coefficient in Figure I-2.b and Figure I-2.c. A resonant frequency shift of about 0.06 GHz and a magnitude sensitivity of 8 dB are observed.

To evaluate the influence brought by the dielectric cover, three configurations are investigated and for each of them the resonant frequency and the reflection coefficient are plotted. The first one does not include a cover (Figure I-2.d and Figure I-2.g) whereas a layer of SU-8 photoresist with a thickness of respectively 25 µm (Figure I-2.e and Figure

I-2.h) and 50 µm (Figure I-2.f and Figure I-2.i) is considered for the two other configurations.

From the measurement results, one can note that the contrast value (magnitude and resonance phase shift) decreases with the increase of the cover thickness, resulting in a worse lateral resolution and a degraded image quality. If we keep constant the distance between the tip and the cover, the increase of the cover thickness actually leads to a larger tip to sample of interest distance. Thus, the degradation of image quality is supposed to come from two parts: the increase of tip-sample distance and the influence of the dielectric layer. However, if the tip-sample distance is kept constant, the influence can be considered mainly due to the dielectric layer. In this case, the relationship between the measurement sensitivity and the thickness and nature of the cover layer is clearly demonstrated.

As a summary, the subsurface imaging is based on the physical properties difference (impedance, dielectric constant, etc.) between the target sample and its coverage layer. One can not only qualitatively observe this variation but also quantitatively obtain the physical properties of the material under the cover layer. In the next section, two important properties which are the dielectric constant and the characteristic impedance are determined by means of two methods.

I.2.3 Quantitatively imaging of materials properties

In this section, quantitative measurement of materials properties such as dielectric constant and characteristic impedance are demonstrated with NFMM. The imaging technique is mainly based on the knowledge of the electromagnetic interaction between the probe and the sample at microwave frequencies [ANL 07]. The mostly used methods to image the material physical properties are discussed in the following parts.

I.2.3.1 Probe-sample interaction method

The first technique is called probe-sample interaction method. This method relies on the investigation of the probe-sample interaction and aims to extract the sample physical

properties directly from the measured results. In this case, the modelling of the tip-sample interaction becomes very important. The established model together with the knowledge of the tip geometry helps for the sample properties determination [ANL 07]. For instance, this method has been used for complex optical constants characterization with an AFM-based NFMM [HIL 00].

Actually, the modelling of the tip-sample interaction is highly dependent on the probe type. For demonstration, two kinds of probe corresponding to a perfect conducting sphere and a magnetic split ring resonator (SRR) based probe are presented.

I.2.3.1.1 The perfect conducting sphere probe

Generally, the perfect conducting sphere probe is considered as the most classic one that is used in the NFMM system. As can be seen in Figure I-3.a, it is generally made up with a sharpened metal tip that is mounted on the center conductor of a coaxial connector. The metal tip is a sphere whose radius is the probe apex size D.

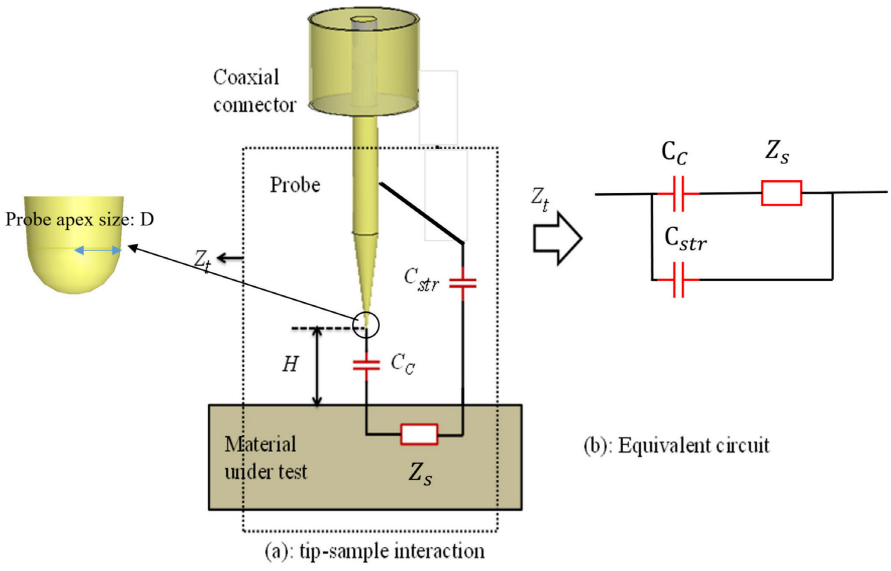

Figure I-3: (a) Lumped element model of tip-sample interaction (b) equivalent circuit [GU 16_c].

To describe the interaction between the tip and the sample, a lumped element model is given [GU 16_c]. The impedance Z_t is regarded as the probe impedance and can be

calculated by the equivalent circuit illustrated in Figure I-3.b. One can note that three parameters have an influence on the impedance Z_t, which are the tip-sample capacitance C_c, the sample 'near field' impedance Z_s ($R_s, L_s,\ C_s$) and the tip body to sample capacitance C_{str}. The sample impedance Z_s can be further divided into sample resistance R_s, inductance L_s and capacitance C_s [ANL 07] [GU 16_c].

$$Z_t{}^{-1} = (\frac{1}{j\omega C_c} + Z_s)^{-1} + j\omega C_{str} \qquad (I-1)$$

Z_S is related to the energy stored and/or dissipated in the sample. The tip-sample capacitance C_c and the tip body to sample capacitance C_{str} can be calculated with the distance between the tip and sample (H). To ensure a high sensitivity ($Z_t \sim Z_S$), the term $1/\omega C_c Z_S$ as well as the term $\omega C_{str} Z_S$ has to be much smaller than or at least on the order of unity. This condition is satisfied when H is much smaller than the probe apex size D [ANL 07]. If one consider the near-field impedance is according to a homogeneous bulk sample, the equation I-1 can be further transformed to equation I-2 in the near field region [ANL 07]:

$$Z_s = \frac{1}{j\omega\varepsilon_0\varepsilon_s D} \qquad (I-2)$$

From this equation, one can find it is basically the impedance of a capacitor with a geometrical capacitance $\varepsilon_0\varepsilon_s D$ filled up with a material of complex relative permittivity $\varepsilon_s = \varepsilon' - j\varepsilon''$. This concept can also be applied for different materials such as dielectrics, semiconductors and normal metals [ANL 07]. Thanks to this model, the relationship between the material dielectric permittivity and the probe characteristic impedance is clear when the tip apex size is known.

I.2.3.1.2 The magnetic SRR probe

Apart from the classic perfect conducting sphere probe, other types of probes are also able to evaluate the sample properties. Very recently, Dmitry Isakov and his colleagues

have proposed a SRR based probe for the relative dielectric permittivity determination [ISA 17]. As can be seen from Figure I-4.a, the SRR is inserted in between two magnetic loops which are connected to the two ports of the VNA. The size of the ring is expressed with an outer radius r, a width w, a height h and a gap width g.

In case of free space, the SRR excitation is a time-varying magnetic field which is parallel to the split ring axis. The SRR response comes from the resonant exchange of energy between the electrostatic fields in the capacitive gap and the inductive currents inside the split ring. Thus, the SRR can be considered as a LC circuit with an effective inductance L and a capacitance C with magnetic resonance frequency:

$$f_0 = (2\pi\sqrt{LC})^{-1} \qquad (I-3)$$

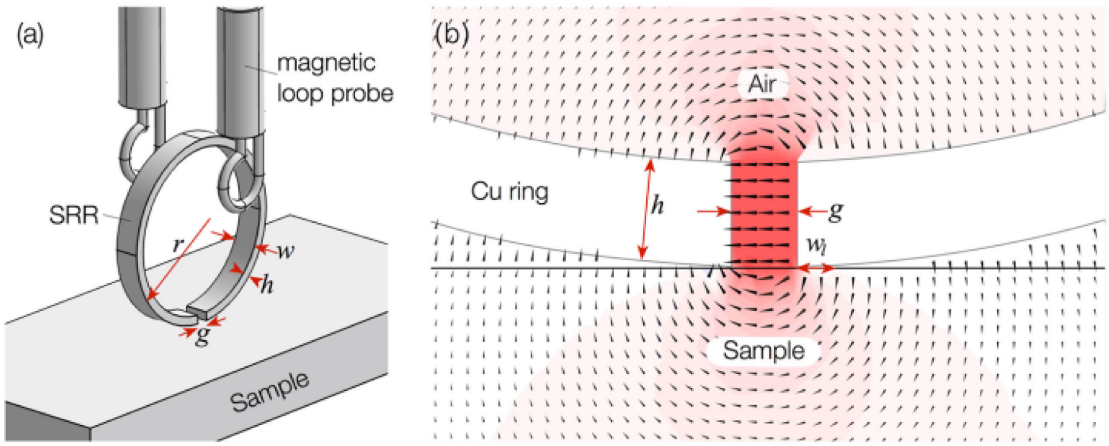

Figure I-4: (a) Schematic of a split ring resonator based probe (b) an example of a full wave electromagnetic simulation of the interaction between the probe and the sample at 15 GHz [ISA 17].

A full wave electromagnetic simulation of the interaction between the probe and sample is illustrated in Figure I-4.b when the SRR is in contact with the sample. The vectors and the color contours indicate the direction and intensity of the induced electric field in the cross section at the resonant frequency. In this case, the capacitance between the SRR and the sample can be assumed to be the sum of the gap capacitance C_{gap}, the ring surface capacitance C_{ring} and the sample capacitance C_{sample}.

$$C = C_{gap} + C_{ring} + C_{sample} \qquad (I-4)$$

The magnetic inductance L and the ring surface capacitance C_{ring} are taken from [SYD 09]:

$$L = \mu_0 R(log\frac{8R}{h+w} - \frac{1}{2})$$
$$C_{ring} = 2\varepsilon_0 \frac{h+w}{\pi} log\frac{4(r-h)}{g} \qquad (I-5)$$

Where the terms ε_0 and μ_0 are the free space permittivity and permeability and R is the mean ring radius (r-h/2).

The gap capacitance C_{gap} is regarded as a sum of a parallel plate capacitance due to the air in the gap and the fringing capacitance at the ring edges. It is expressed as:

$$C_{gap} = \varepsilon_0 \frac{hw}{g} + \varepsilon_0(h+w+g) \qquad (I-6)$$

When the SRR is in contact with the sample with a relative dielectric permittivity ε_r, the sample capacitance C_{sample} can be calculated by the conformal transformation method [YAN 16]:

$$C_{sample} = \varepsilon_0 \frac{l}{2}(\frac{K(k_0')}{K(k_0)} + \varepsilon_r \frac{K(k_1')}{K(k_1)}) \qquad (I-7)$$

Where l is the length of the plate of the parallel plate capacitor. The terms $K(k_0')$, $K(k_0)$, $K(k_1')$ and $K(k_1)$ are the complete elliptic integrals of the first kind with $k' = \sqrt{1-k^2}$. k_0 and k_1 are defined as:

$$k_0 = \frac{g}{2w_l + g}$$

$$k_1 = \frac{\tanh(\pi g/4S)}{\tanh(\pi(2w_l + g)/4S)} \qquad (I-8)$$

Where S is the thickness of the dielectric substrate slab and W_l is the contact length between the SRR and sample surface. It can be approximated as:

$$W_l = \sqrt{r^2 - (\frac{h}{32})^2} - \frac{g}{2} \qquad (I-9)$$

With the combination of the equations from I-3 to I-9, the analytical expression for the shift of the resonant frequency f_0 as a function of the sample relative dielectric permittivity ε_r can be achieved:

$$\varepsilon_r(f) = A + Bf_0^{-2} \qquad (I-10)$$

$$\text{Where} \quad A = \frac{-\left(C_{gap} + C_{ring} + \varepsilon_0 \frac{l}{2}\frac{K(k_0')}{K(k_0)}\right)}{\varepsilon_0 \frac{l}{2}\frac{K(k_1')}{K(k_1)}}$$

$$and \quad B = \frac{1}{4\pi^2 \varepsilon_0 L \frac{l}{2}\frac{K(k_1')}{K(k_1)}}$$

As can be seen from the equations previously given, the coefficients A and B are functions of C_{gap}, C_{ring} and the complete elliptic integrals of the first kind. These terms are defined with an outer radius r, a width w, a height h, a gap width g, the thickness of the dielectric substrate S and the contact length between the SRR and sample surface w_l. Thus, the coefficients A and B can be therefore determined.

With the theoretical analysis provided above, the relationship between the geometry of the split ring probe and the relative dielectric permittivity of the material under test is estimated. Hence, a measurement accuracy within 5% can be achieved [ISA 17].

As demonstrated with the two examples given above, the probe-sample interaction method is based on the combination of a well-defined probe model and the knowledge of the tip geometry to find out a relationship between known parameters and the sample properties.

I.2.3.2 Semi-empirical method

The principle of the semi-empirical method relies on mapping the samples with known physical properties. Actually, it firstly evaluates samples with known properties and establish a calibration model so that the physical property of an unknown sample can then be deduced from the measured quantity [FAR 11_c].

Unlike the probe-sample interaction method, the semi-empirical method owns the outstanding merit that the tip geometry analysis is no longer required [MON 17]. Indeed, it contributes to the simplification of the characterization method.

Thanks to this approach, the determination of the sample's inhomogeneity [MON 17], dopant density [GRA 15] or complex impedance [GRA 14] becomes possible. Moreover, the evaluation of dielectric/ferroelectric constants of solid materials [GAO 04_a], biological solutions [GU 16_a] [GU 16_b] or thin films [GAO 04_b] can be easily realized.

In fact, the core content of this approach relates to the creation of an interpolation routine that justifies the calibration procedure [ANL 07] [GU 16_c]. Hereafter we give an example for a better understanding.

As illustrated in Figure I-5, the idea is to convert the measured quantity, in this case the transmission coefficient (S_{21m}), into the parameter of interest, in this case the complex impedance. The procedure can be divided into two steps. The first step is normally based

on a well-defined calibration model. In this example, the authors make use of the one-port calibration to transfer the S_{21m} into impedance [AGI 02] [GU 16_c]. The calculation of the three complex error terms is done by choosing three samples with known impedance at a fixed frequency. Knowing this impedance and its corresponding S_{21m}, the three error terms are calculated. The second step is to deduce the impedance of an unknown sample using the obtained three error terms together with the measured S_{21m}.

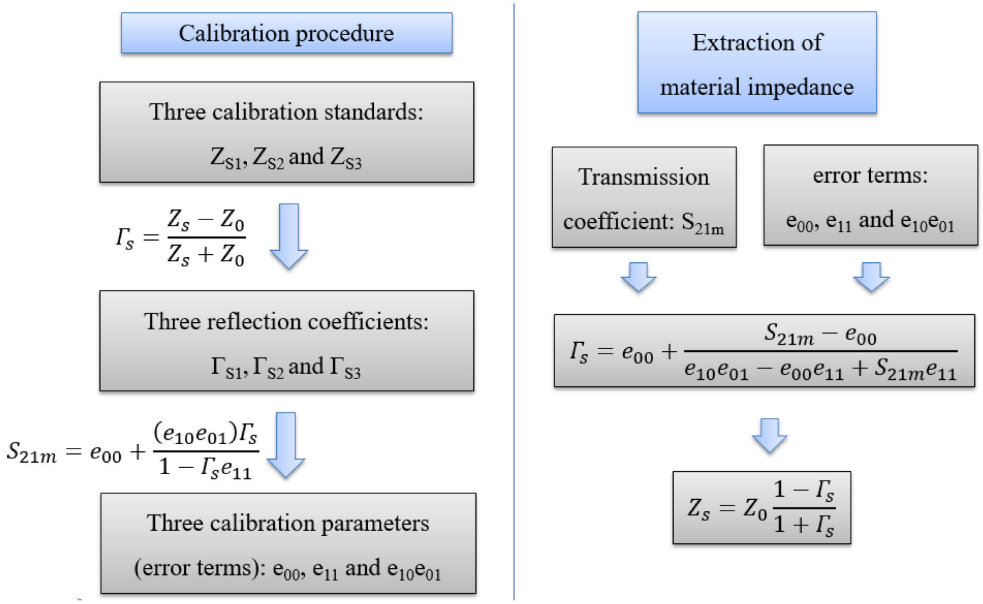

Figure I-5: A calibration procedure of an interferometer-based NFMM to measure the complex impedance [GU 16_c].

As a summary, the principle of the semi-empirical approach is to create a routine between the measured quantities and standard samples. Once this routine is verified, samples with unknown properties can be characterized. This approach is generally simple and efficient. However, it is sometimes difficult to find standard samples, which is considered as a limitation.

I.2.4 NFMM limitations

In the previous sections, several advantages of the NFMM are presented such as the subsurface imaging and the measurement of materials physical properties possibility.

Nevertheless, some limitations exist in the NFMM system, they are discussed in this section.

The first limitation is linked to the measurement sensitivity. Actually, when the VNA is directly connected to an evanescent microwave probe (EMP), a great impedance mismatch between the intrinsic impedance of the VNA (50 Ω) and the impedance of the EMP (tens or hundreds of KΩ) leads to an extremely small measurement sensitivity. This limitation can be overcome by inserting a matching network between the EMP and the VNA. This point is discussed in details in the section I.3.4.

The second limitation is related to the measurement noise. Actually, for a single EMP which is able to measure the signal in reflection mode, its functions are divided into two parts: transmission of the signal from the signal generator to the sample and reception of the signal reflected by the sample. When sharing the same electrode, the common-mode signal will lead to a large shot noise [LAI 07]. The measurement noise is also related to the setting parameters of the system. For instance, the Q factor of the matching network (Q factor for resonator based NFMM and zero level for interferometer based NFMM) adjusts the VNA noise floor and consequently leads to an impact on the system noise.

The third limitation appears only for the NFMM without the feedback system. Indeed, the resolution of the NFMM system is mainly governed by the EMP apex size as well as its position (stand-off distance). In our case, to ensure the NFMM works in the near field region, the stand-off distance between the EMP and the sample has to be much smaller than the EMP apex size. For a high resolution NFMM system, the EMP apex size has to be very small and the stand-off distance is therefore very short. However, without the feedback system, the sharp EMP has a chance to touch the sample and undergo a transformation of the tip at that short stand-off distance, leading to a degradation of the imaging quality [ANL 01].

The fourth limitation occurs when imaging a large area with a high resolution is desired. Because the microwave source suffers from a signal drift with time in terms of

frequency and magnitude, a compromise between a high resolution and the scanning duration has to be made. This limitation is discussed in details in chapter II.

However, even with these limitations, the NFMM system is considered as an innovative and an effective solution for surface/subsurface imaging and materials characterization.

I.2.5 Conclusion

As a summary, in this section, we firstly present one of the major advantages of the NFMM, which is its ability in subsurface imaging. A few applications relying on this feature are also presented. After that, a quantitative approach for the determination of the sample physical properties based on two techniques: the probe-sample interaction method and the semi-empirical method is discussed. Each of them is briefly described and examples are given. Finally, the limitations of the NFMM are also discussed. Since the NFMM shows outstanding merits compared to the other types of SPM, a typical NFMM setup is consequently reported in the next section for a more detailed presentation of its structure and operating principle.

I.3 A Typical NFMM setup

I.3.1 Introduction

In this section, a classical NFMM setup is described in details. Generally, a typical NFMM, no matter it is a homemade or a commercial one, includes a signal generation system/acquisition system, a XYZ scanner, a matching network and an evanescent microwave probe (EMP). Practically, the signal generation system can be a signal generator (for example a VNA or a frequency synthetizer). The data acquisition system is mostly a combination of a VNA and a control interface. The XYZ scanner determines the 3 dimensions resolution and the scan range while the matching network mainly gives the sensitivity and the operating frequency band. The last component but probably the most

important one is the EMP, which gives the intrinsic resolution of the NFMM. In the following part, these components are more finely described.

I.3.2 Signal generation and acquisition system

A signal generation/acquisition system should be the first component that has to be taken into account for the build-up of a NFMM system. Generally, the VNA is regarded as the perfect fit for this job because of both its signal generation function and its ability for the detection of signals with a high precision and a good sensitivity [GRA 14] [GAO 14] [WU 15]. However, a VNA is always expensive for a low cost homemade NFMM. With the advent of the multi-port technique, a replacement has been proposed by changing the VNA by a combination of a signal generation system (frequency synthesizer or a voltage-controlled oscillator phase-locked loop) and a multi-port based reflectometer [BEN 08] [HAD 11] [HAD 13].

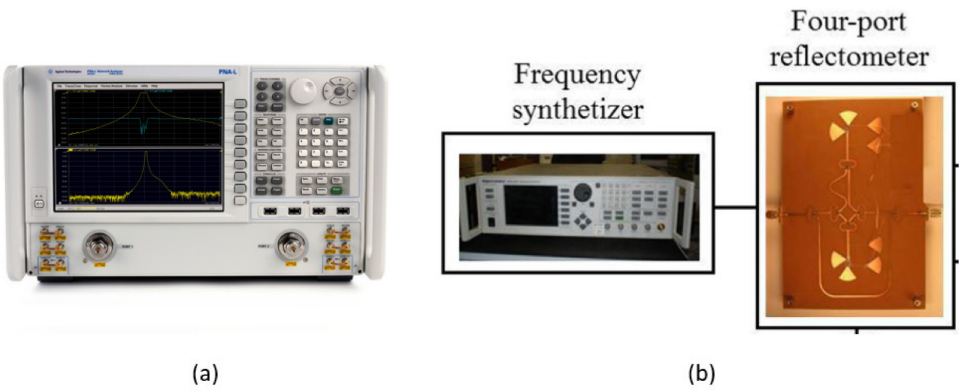

Figure I-6: Schematic of a signal generation/acquisition system: (a) VNA (b) a combination of a frequency synthesizer and multi-port based reflectometer [HAD 11].

For illustration, in the Figure I-6 above, one can find two solutions for the signal generation/ acquisition system. Indeed, the solution is chosen according to the design goals of the NFMM system, such as the cost, the sensitivity and so on.

I.3.3 XYZ scanner

Once the signal generation system is chosen, one will face the problem to control the tip-sample distance and move accurately the tip over the sample surface during the imaging (or inversely move the sample surface under the tip). This problem can be solved with the help of XYZ scanning elements.

In fact, the choice of a XYZ scanner is based on the resolution targeted and related to the NFMM applications. For instance, for a NFMM that works in nm scale, a very fine resolution is required for the XYZ scanner [CHI 12] [HAN 08]. In this case, the scanner is always made of piezoelectric materials and enables such fine resolution when an external electric field is applied [MIR 04]. Furthermore, several feed-back systems are commonly used in these NFMM set-ups to ensure a constant tip-sample distance. These feed-back systems are either AFM-based [BIN 86] or STM-based [WIL 89] as described in the references [HOW 96] [HAN 08]. However, when the application requests to scan a large area, such as in case of subsurface defect characterization [MAL 17], diagnosis of integrated devices [SAF 14] and 3D-printed circuit element investigation [COR 15], a coarser movement is needed and the resolution of the XYZ scanner is rather in µm scale or even larger to save scanning time.

The Figure I-7 presents two types of XYZ scanner corresponding to different resolutions. The first one (Figure I-7.a) is integrated in an Agilent 5400 SPM that presents a scanning range in three dimensions of 90 µm*90 µm*8 µm. Its resolution is in nm scale [HAN 08]. The second one (Figure I-7.b) enables a scanning surface of 7cm*7cm and a minimum scanning step in mm scale, which is suitable for large area imaging [REN 11].

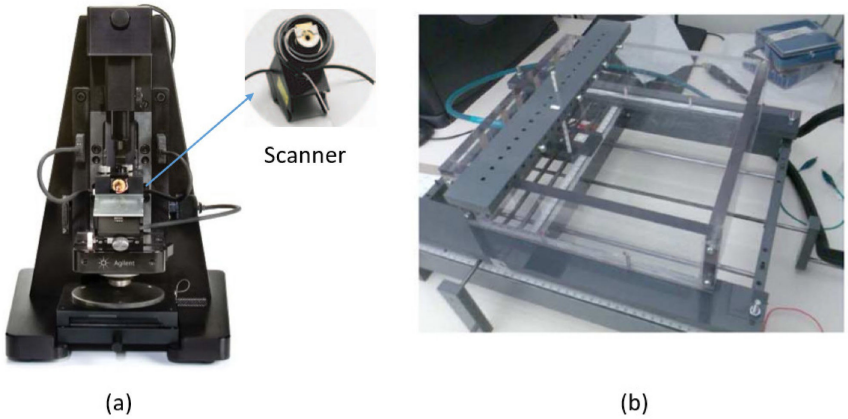

Figure I-7: Schematic of two types of XYZ scanner: (a) Scanner integrated in Agilent 5400 AFM/SPM [HAN 08] (b) Scanner designed for large area imaging [REN 11].

One has to mention that, during the movement of the scanning platform, imperfections caused by the vibration are hardly avoided. Nevertheless, this effect can be largely reduced by using an acoustic isolation chamber [CHI 12] or a marble isolation stage [GU 16_a].

I.3.4 Matching network

After the discussion about the XYZ scanner selection strategy, the matching network is now under investigation. As mentioned in section I.2.4, this latter plays a major role in the NFMM system since it is directly related to the measurement sensitivity. Actually, an important mismatch between the high impedance probe (from tens to hundreds of kΩ) and the intrinsic impedance of the VNA (50 Ω characteristic impedance) always exists in the NFMM systems [HAP 14] [GU 16_d]. To better observe the influence of such mismatch on the measured reflection coefficient, one can examine the case where a pure resistive impedance (DUT) is connected to a VNA.

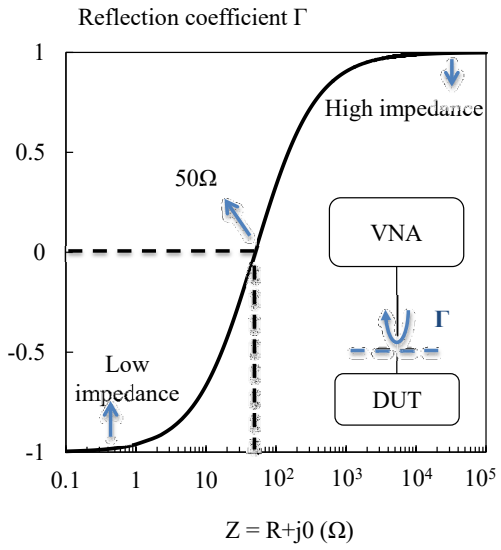

Figure I-8: Reflection coefficient Γ as a function of a pure resistive impedance (DUT). The VNA intrinsic impedance is 50 Ω [GU 16_c].

As illustrated in the Figure I-8, one can find out the sensitivity of the reflection coefficient is very small in two regions. These latter correspond to areas where the reflection coefficient is close to 1 or -1 which is respectively observed when a very high impedance or a very low impedance, compared to the intrinsic impedance of the VNA (Z_0 =50 Ω), is connected. On the contrary, if we adjust the impedance of the DUT (Z_{DUT}) to 50 Ω (reflection coefficient Γ close to 0), the reflection coefficient becomes very sensitive (the largest slope in the curve).

As a conclusion, the best matching occurs of course when the DUT shows an impedance which is identical to the VNA one. The reflection coefficient is expressed by the following equation [DAR 13] [WEB 14] [GU 16_c]:

$$\Gamma = \frac{Z_{DUT} - Z_0}{Z_{DUT} + Z_0}$$

In the following sections, we present two matching networks that are mostly used. They are respectively the resonator based and interferometer based matching networks.

I.3.4.1 Resonator based matching network

In this paragraph, the resonator based matching network is under investigation. Its basic structures, matching principle and targeted frequency band are briefly presented. Actually, different types of resonators have been applied in the NFMM systems such as resonant waveguide cavities [KIM 04], split-ring resonators [REN 11], resonant transmission lines [WAN 07] [Bar 14] [HUM 11] and resonant loaded apertures [MAL 16]. These resonators help to overcome the impedance difference between the probe and the 50 Ω VNA in order to reach a high measurement sensitivity. As already said this impedance difference can be huge.

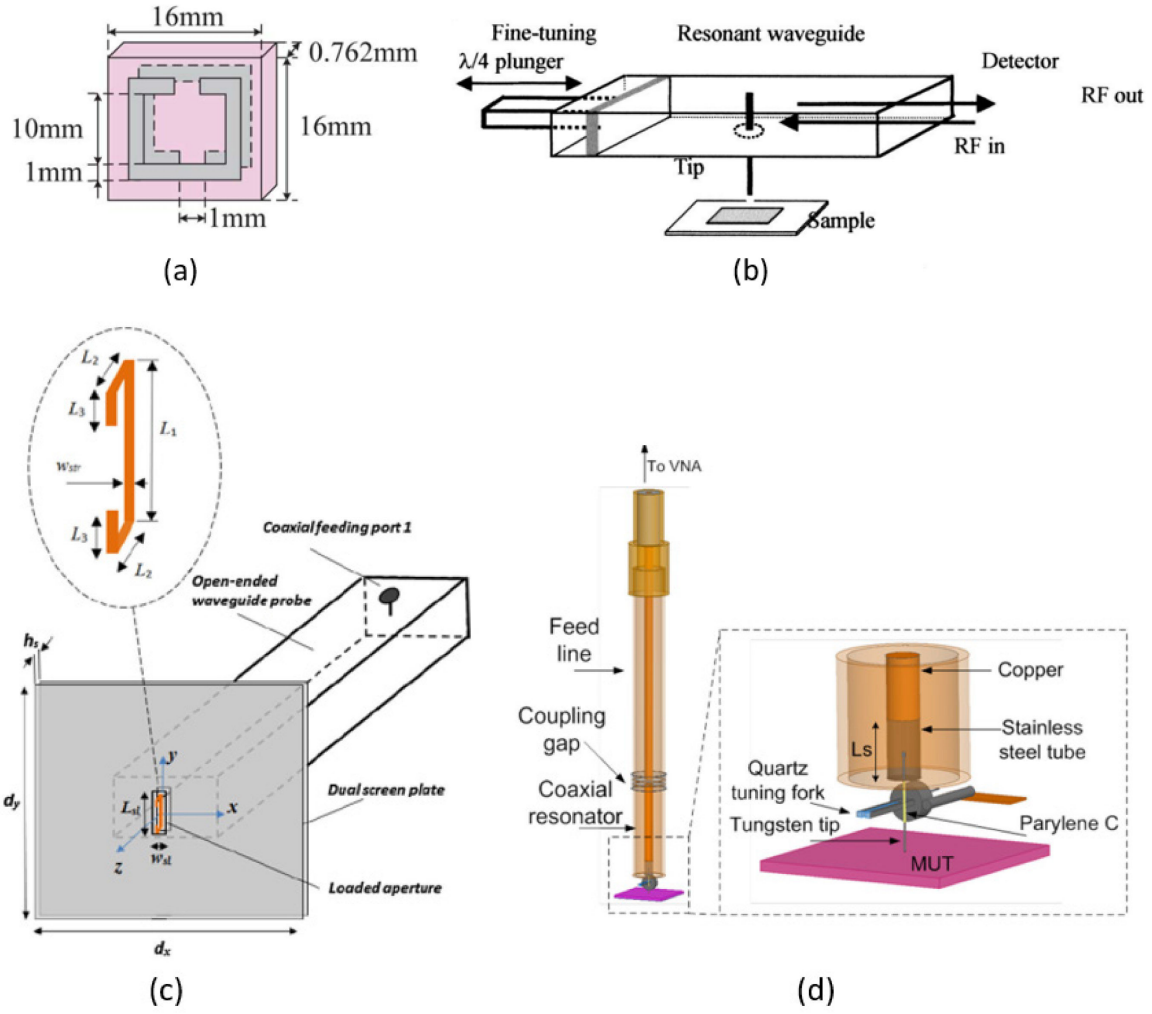

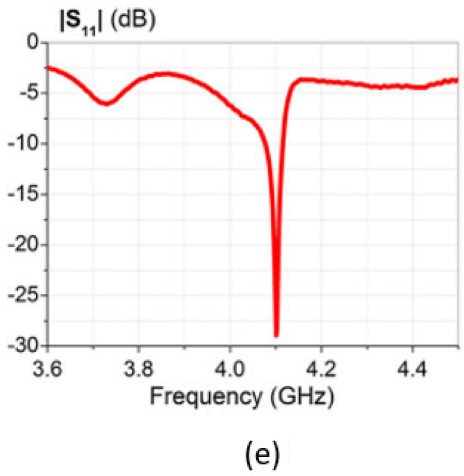

Figure I-9: Schematic of four typical resonator based matching networks and an example of a measured reflection coefficient: (a) a split-ring resonator [REN 11] (b) a resonant waveguide [KIM 04] (c) a loaded aperture probe [MAL 16] (d) a coaxial resonator [WAN 07] (e) The measured reflection coefficient in terms of magnitude at the resonance frequency (4.1 GHz) for the resonant waveguide [KIM 04].

The Figure I-9 presents four typical resonator based matching networks. Although the resonant structures are different, the design target is always the same: the achievement of a very low level in terms of magnitude of the reflection coefficient S_{11} at a particular resonance frequency (Figure I-9.e). Actually, this very low level indicates that there is nearly no reflection occurring at the resonance frequency, the matching is therefore achieved. Indeed, this very low level is quantified by the quality factor (Q factor). A higher Q factor results in a better sensitivity.

After a brief introduction of basic structures used as resonator based matching network, we give a non-exhaustive list of examples of resonator based NFMM in the following table.

Resonator structure	Operating frequency (GHz)	Application	Reference
Waveguide	60	Non-destructive imaging	[KIM 04]
Split-ring	1.2	Subsurface detection	[REN 12]
Split-ring	1.1	Lossy media detection	[REN 09]
¼ λ coaxial	1.8	Thin films permittivity	[BAR 14]
¼ λ coaxial	2.2	Subsurface imaging	[SUN 14]
¼ λ transmission line	2	Ferromagnet imaging	[WAN 07]
Coaxial transmission line	0.76	Subsurface detection	[CHI 12]
Coaxial transmission line	7.5	Sheet resistance imaging	[STE 98]
Coaxial transmission line	5	Subsurface imaging	[COR 15]
Stripline	1	Material nonuniformity	[TAB 99_d]
Microstrip	10	Semiconductor imaging	[TAB 99_c]
Load aperture probe	4.1	Defect characterization	[MAL 17]
Load aperture probe	2.3	Subsurface imaging	[MAL 15]

Table I-1: Examples of resonator structures as well as the traget applications.

From the Table.I-1, at wavelengths in the millimetre range, one can note that the waveguide is favoured thanks to its high frequency performance. The split-ring resonator works mainly around 1 GHz while the load aperture structure works below 5 GHz. The transmission line based resonator can be divided into four parts. The first one is the $\lambda/4$ transmission line that operates around 2 GHz. The second one is the coaxial based resonator, its operation frequency depends on the geometry of the coaxial line. The third type and the last one refers respectively to the stripline and microstrip based transmission line resonators. They are also able to work in different frequency bands. This feature is related to the dimension of the transmission line. Nevertheless, all of these resonator-based structures share the same restriction in terms of frequency bandwidth. This drawback makes it difficult for broadband applications as for example the broadband dielectric constant characterization of biological samples [GU 16_b]. Furthermore, the measurement sensitivity is strongly dependent on the resonator quality factor which falls rapidly when high-loss materials are involved in the tests [REN 09]. All these limitations have to be overcome. Thus, a novel matching technique based on interferometers is introduced in the next part.

I.3.4.2 Interferometer based matching network (IBMN)

Since very recently, the broadband characterization of materials physical properties is of interest by using the NFMM system [GU 16_a] [GU 16_b]. To achieve such test, the resonator based matching network is no longer appropriate since it is a narrow working frequency band system. In addition, it is not realistic to split the frequency band of interest in several pieces to make use of various resonators. Thus, a new broadband matching network is needed.

To this end, an interferometer-based matching technique has been introduced to efficiently adjust the electromagnetic coupling between the probe and the sample under test (SUT) to guarantee a high sensitivity in a broad frequency band [BAK 13] [HAD 12].

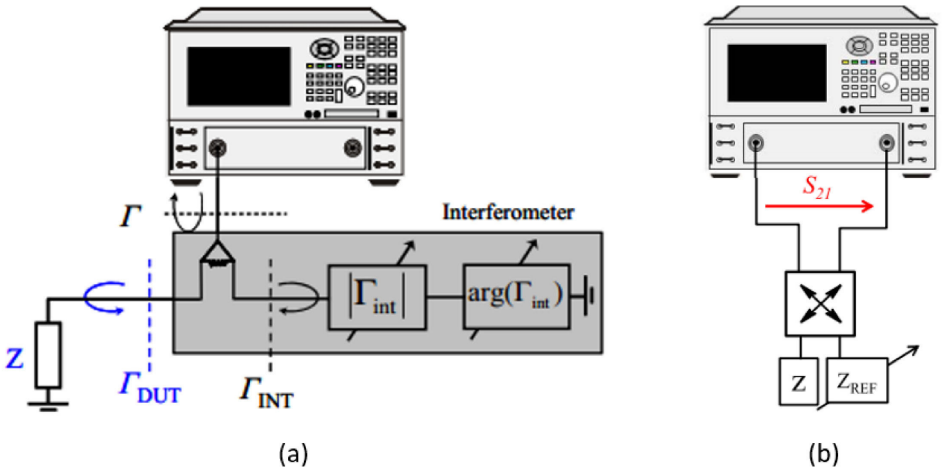

Figure I-10: Schematic of the IBMN in two modes; (a) The reflection mode with an impedance tuner and a power divider [BAK 13] (b) The transmission mode with an impedance tuner and a hybrid coupler [HAD 12].

As can be seen from the Figure I-10, basically, the IBMN can be achieved through two basis: transmission mode [HAD 14] [HOF 17] and reflection mode structures [BAK 13] [BAK 14]. The main difference between these two structures is that the transmission mode includes a hybrid coupler while the reflection mode relies on a power divider. Compare to the reflection mode, the transmission mode owns an advantage in terms of noise floor and directivity error when measuring small signals. Actually, these two

parameters are much lower in this case. These features help to increase the measurement sensitivity.

Inside the impedance tuner, one can find two components: an attenuator and a phase shifter. The operational frequency band of the IBMN is directly related to the impedance tuner characteristics. Furthermore, all these components should be highly stable, accurate and repeatable for a better performance of the IBMN.

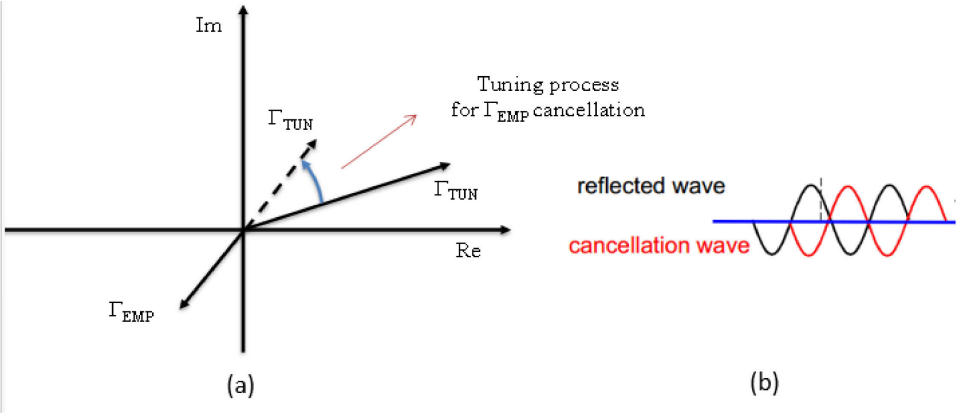

Figure I-11: The cancellation procedure; (a) the tuning process for the Γ_{EMP} cancellation (b) The combination of the reflected and cancellation waves [BAK 13], [GU 16].

After a brief introduction of the components which compose the IBMN, the matching process is now discussed by using the transmission mode structure as an example. The signal reflected by the EMP (Γ_{EMP}) and the one coming from the impedance tuner (Γ_{TUN}) are combined in the hybrid coupler. The two signals are combined as indicated in Figure I-11.a. Therefore, thanks to the coupler, the measured transmission coefficient resulting from the combination of these two signals is:

$$S_{21} = \frac{1}{2}(\Gamma_{TUN} + \Gamma_{EMP}) \qquad (I-11)$$

Thus, the tuner can be adjusted in order to null the transmission coefficient (*i.e.* Γ_{TUN} and Γ_{EMP} are equal in magnitude but opposite in phase). The very low level of S_{21} subsequent to this operation is called zero level or cancellation level (i.e. $S_{21} =$

$\frac{1}{2}(\Gamma_{TUN} + \Gamma_{EMP}) = 0$). This cancellation procedure can be easily understood with the help of the Figure I-11.

Recently, the IBMN has been integrated in commercial SMMs to perform a broadband matching package [DEB 11]. Its calibration procedure as well as the noise reduction method is also introduced in some research works [DAR 13] [MIC 15] [TUC 17].

I.3.5 NFMM probes

After talking about the signal generation system, the scanner, the data acquisition system (computer) and the matching network, a very important part of the NFMM, the evanescent microwave probe (EMP) is investigated in this section.

Basically, the probes can be classified whether they are resonant or not. For the resonant EMP, it normally combines a resonator structure with the probe to realize the impedance matching. As illustrated in the Figure I-9.c, the loaded aperture probe is a good example of a resonant EMP. The resonance occurs thanks to the dipole inserted inside the aperture and leads to a high level of EM coupling [MAL 17]. For the non-resonant EMP, different structures have been studied and compared in the thesis of GU [GU 16_c] and some review papers [ANL 07] [EI 17]. Examples of structures such as the coaxial line [CHI 12], the aperture based probe [GAL 14], the STM tip [FAR 11_a] [FAR 12_b], the parallel line [WIL 95], the magnetic loop probe [ISA 17] and the AFM tip [LAI 07] exemplify this kind of probe. These various structures are illustrated in the Figure I-12.

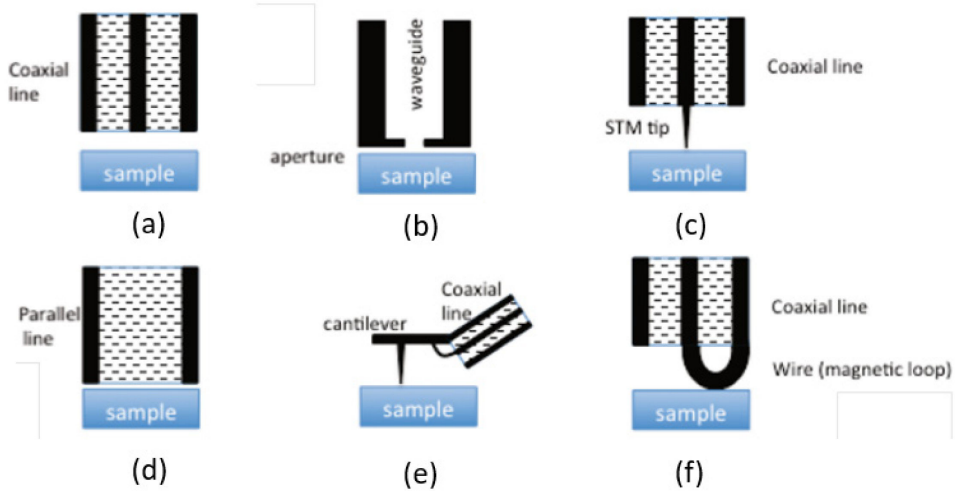

Figure I-12: Schematic of different types of EMP [EI 17]; (a) Coaxial line based probe (b) Aperture based probe (c) STM tip (d) Parallel line based probe (e) AFM probe (f) Magnetic loop probe.

The distinction can also be made from the material used to fabricate the tip. Indeed, different materials can be used to form the tip and will lead to various features. For instance, dielectric probes made of silicon or silicon nitride tips are commonly used in the AFM to detect defects buried in metallic samples [PLA 11].

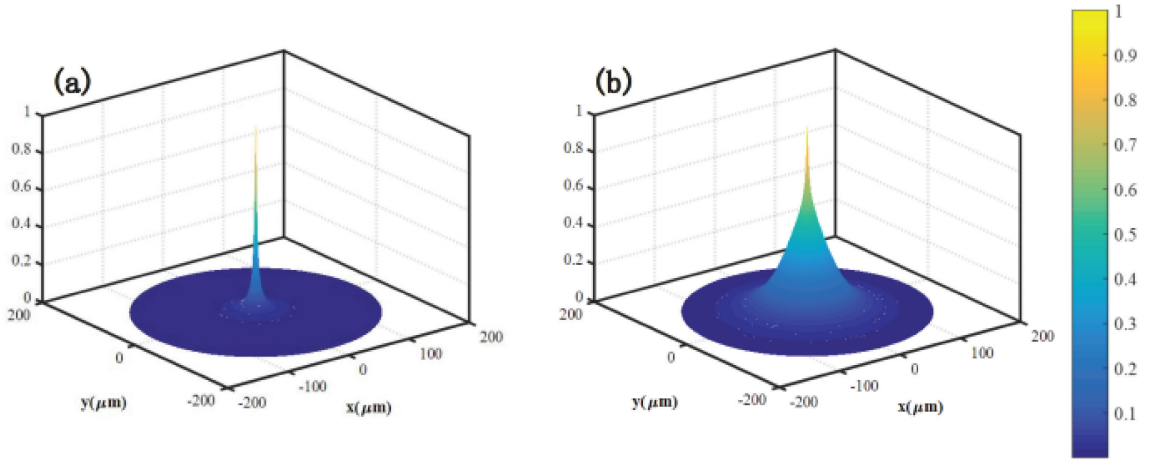

Figure I-13: Normalized electric field generated on a conducting substrate by EMP with different materials [WU 17]; (a) Titanium tip (b) Silicon tip.

The electric fields generated by dielectric and metallic probes are presented in the Figure I-13. From the figure one can summarize the difference in two points. The first point

is related to the electric field intensity around the tip apex. For the dielectric probe, the electric field is less localized at the tip apex than for the metallic one. This feature indicates that a better lateral resolution can be achieved by the metallic tip. The second point is linked to the E-field area of the tip. The dielectric probe presents a larger E-field area during the imaging application, which is sometimes regarded as an important feature. For example, to avoid the nonlinear behaviour of the SUT due to the strong local electric field of the metal tip, the dielectric probe is selected [WU 17].

I.3.6 Conclusion

In this section, the main components which compose the NFMM system are introduced. Practically, a typical NFMM setup can be divided into a signal generation system, a data acquisition system, a scanner, a matching network and an evanescent microwave probe. As discussed previously, the selection strategy of each component is mainly due to considerations on the SUT's physical properties, the targeted application, the applied frequency band, the cost of the system and so on.

I.4 Conclusion

In this chapter, some typical features of the NFMM including the advantages and limitations are presented firstly. The NFMM owns an outstanding merit compared to the other kinds of SPM, which is its ability for surface/subsurface imaging and measurement of the sample physical properties at the same time. These features are demonstrated with the help of examples extracted from research works published recently for most of them. After that, the main components that constitute a NFMM are investigated.

We have shown that according to the targeted applications, the working frequency and cost of the system, the choice of the signal generation system, the scanner and the data acquisition system is made. The two most popular matching networks are described in details to address the sensitivity limitation. Depending of various types of probes, different applications at selected operating frequencies can be achieved.

I.5 References

(92 references, Classified in alphabetical order)

[ABB 73] Abbe, E. (1873). Beiträge zur Theorie des Mikroskops und der mikroskopischen Wahrnehmung. *Archiv für mikroskopische Anatomie*, *9*(1), 413-418.

[ABB 84] Abbe, E. (1884). Note on the Proper Definition of the Amplifying Power of a Lens or Lens-system. *Journal of Microscopy*, *4*(3), 348-351.

[AGI 02] Agilent, A. N. (2002). 1287-3 applying error correction to network analyzer measurements. *Agilent Technologies, USA*.

[ANL 01] Anlage, S. M., Steinhauer, D. E., Feenstra, B. J., Vlahacos, C. P., & Wellstood, F. C. (2001). Near-field microwave microscopy of materials properties. In *Microwave Superconductivity* (pp. 239-269). Springer Netherlands.

[ANL 07] Anlage, S. M., Talanov, V. V., & Schwartz, A. R. (2007). Principles of near-field microwave microscopy. In *Scanning probe microscopy* (pp. 215-253). Springer New York.

[ASH 72] E. A. Ash and G. Nicholls (1972), "Super-resolution aperture scanning microscope.," Nature, vol. 237, n°. 5357, pp. 510–512.

[BAK 13] Bakli, H., Haddadi, K., & Lasri, T. (2013, May). Interferometric technique for scanning near-field microwave microscopy applications. In *Instrumentation and Measurement Technology Conference (I2MTC), 2013 IEEE International* (pp. 1694-1698).

[BAK 14] Bakli, H., Haddadi, K., & Lasri, T. (2014). Interferometric technique for scanning near-field microwave microscopy applications. *IEEE Transactions on Instrumentation and Measurement*, *63*(5), 1281-1286.

[BAK 15] Bakli, H. (2015). *Développement d'une plate-forme de microscopie champ proche hyperfréquence par interférométrie* (Doctoral dissertation, Lille 1).

[BEN 08] Benzaim, O., Haddadi, K., Wang, M. M., Maazi, M., Glay, D., & Lasri, T. (2008). Scanning near-field millimeter-wave microscope: Application to a vector-coding technique. *IEEE Transactions on Instrumentation and Measurement*, *57*(11), 2392-2397.

[BIN 82_a] Binnig, G., Rohrer, H. (1982). *U.S. Patent No. 4,343,993*. Washington, DC: U.S. Patent and Trademark Office.

[BIN 82_b] Binnig, G., Rohrer, H., Gerber, C., & Weibel, E. (1982). Surface studies by scanning tunneling microscopy. *Physical review letters*, *49*(1), 57.

[BIN 86] Binnig, G., Binnig, G., Quate, C. F., & Gerber, C. (1986). Atomic force microscope. *Physical review letters*, *56*(9), 930.

[BRY 65] C. A. Bryant and J. B. Gunn (1965), "Noncontact Technique for the Local Measurement of Semiconductor Resistivity," Rev. Sci. Instrum., vol. 36, p. 1614.

[COR 15] Córdoba-Erazo, M. F. & Weller, T. M. (2015). Noncontact electrical characterization of printed resistors using microwave microscopy. *IEEE Transactions on Instrumentation and Measurement*, *64*(2), 509-515.

[CHI 12] Chisum, J. D., & Popovic, Z. (2012). Performance limitations and measurement analysis of a near-field microwave microscope for nondestructive and subsurface detection. *IEEE Transactions on Microwave Theory and Techniques*, *60*(8), 2605-2615.

[DAR 13] T. Dargent, K. Haddadi, T. Lasri, N. Clement, D. Ducatteau, B. Legrand, H. Tanbakuchi, and D. Theron (2013), "An interferometric scanning microwave microscope and calibration method for sub-fF microwave measurements," Rev. Sci. Instrum., vol. 84, nº. 12.

[DEB 11] Debroucke, R., Gloria, D., Ducatteau, D., Theron, D., Tanbakuchi, H., & Gaquiere, C. (2011, June). attoF MOS varactor RF measurement VNA coupled with interferometer. In *Microwave Measurement Conference (ARFTG), 2011 77th ARFTG* (pp. 1-2).

[EFI 17] Efimov, A. E., Agapov, I. I., Agapova, O. I., Oleinikov, V. A., Mezin, A. V., Molinari, M & Mochalov, K. E. (2017). A novel design of a scanning probe microscope integrated with an ultramicrotome for serial block-face nanotomography. *Review of Scientific Instruments*, *88*(2), 023701.

[EI 17] El Matbouly, H. (2017). Review on Microwave Metamaterial Structures for Near-Field Imaging. In *Microwave Systems and Applications*.

[FAR 11_a] M. Farina, A. Lucesoli, T. Pietrangelo, A. di Donato, S. Fabiani, G. Venanzoni, D. Mencarelli, T. Rozzi, and A. Morini, (2011) "Disentangling time in a near-field approach to scanning probe microscopy," Nanoscale, vol. 3, nº. 9, pp. 3589–93.

[FAR 11_b] M. Farina, D. Mencarelli, A. Di Donato, G. Venanzoni, and A. Morini, (2011) "Calibration Protocol for Broadband Near-Field Microwave Microscopy," *IEEE Transactions on Microwave Theory and Techniques* vol. 59, nº. 10, pp. 2769–2776.

[FAR 11_c] M. Farina, Mencarelli, D., Di Donato, A., Venanzoni, G., & Morini, A. (2011). Calibration protocol for broadband near-field microwave microscopy. *IEEE Transactions on Microwave Theory and Techniques*, *59*(10), 2769-2776.

[FAR 12] M. Farina, Di Donato, A., Mencarelli, D., Venanzoni, G., & Morini, A. (2012). High resolution scanning microwave microscopy for applications in liquid environment. *IEEE Microwave and wireless components Letters*, *22*(11), 595-597.

[FEN 11] Fenner, M. A., Kienberger, F., Tanbakuchi, H., Huber, H. P., & Hinterdorfer, P. (2011, September). Quantitative measurement of electric properties on the nanometer scale using atomic force microscopy. In *Semiconductor Conference Dresden (SCD)*.

[FRA 59] Z. Frait (1959), "The use of high-frequency modulation in studying ferromagnetic resonance," Czechoslov. J. Phys., vol. 9, nº. 3, pp. 403–404.

[GAL 14] Galin, M. A., Demidov, E. V., & Reznik, A. N. (2014). Determination of the sheet resistance of semiconductor films via near-field microwave microscopy. *Journal of Surface Investigation. X-ray, Synchrotron and Neutron Techniques*, *8*(3), 477-483.

[GAI 07] Gaikovich, K. P. (2007). Subsurface near-field scanning tomography. *Physical review letters*, *98*(18), 183902.

[GAO 98] Gao, C., & Xiang, X. D. (1998). Quantitative microwave near-field microscopy of dielectric properties. *Review of scientific instruments*, *69*(11), 3846-3851.

[GAO 04_a] Gao, C., Hu, B., Takeuchi, I., Chang, K. S., Xiang, X. D., & Wang, G. (2004). Quantitative scanning evanescent microwave microscopy and its applications in characterization of functional materials libraries. *Measurement science and technology*, *16*(1), 248.

[GAO 04_b] Gao, C., Hu, B., Zhang, P., Huang, M., Liu, W., & Takeuchi, I. (2004). Quantitative microwave evanescent microscopy of dielectric thin films using a recursive image charge approach. *Applied physics letters*, *84*(23), 4647-4649.

[GAO 14] Gao, B., Zhang, H., Woo, W. L., Tian, G. Y., Bai, L., & Yin, A. (2014). Smooth nonnegative matrix factorization for defect detection using microwave nondestructive testing and evaluation. *IEEE Transactions on Instrumentation and Measurement*, *63*(4), 923-934.

[GOL 00] M. Golosovsky, a. F. Lann, D. Davidov, and a. Frenkel, (2000) "Microwave near-field imaging of conducting objects of a simple geometric shape," Rev. Sci. Instrum., vol. 71, nº. 10, p. 3927.

[GRA 14] Gramse, G., Kasper, M., Fumagalli, L., Gomila, G., Hinterdorfer, P., & Kienberger, F. (2014). Calibrated complex impedance and permittivity measurements with scanning microwave microscopy. *Nanotechnology*, *25*(14), 145703.

[GRA 15] Gramse, G., Brinciotti, E., Lucibello, A., Patil, S. B., Kasper, M., Rankl, C. & Kienberger, F. (2015). Quantitative sub-surface and non-contact imaging using scanning microwave microscopy. *Nanotechnology*, *26*(13), 135701.

[GU 16_a] Gu, S., Lin, T., & Lasri, T. (2016). Dielectric properties characterization of saline solutions by near-field microwave microscopy. *Measurement Science and Technology*, *28*(1), 014014.

[GU 16_b] Gu, S., Lin, T., & Lasri, T. (2016). Broadband dielectric characterization of aqueous saline solutions by an interferometer-based microwave microscope. *Applied Physics Letters*, *108*(24), 242903.

[GU 16_c] Gu, S. (2016). Contribution to broadband local characterization of materials by near-field microwave microscopy (Doctoral dissertation, Lille 1).

[GU 16_d] Gu, S., Haddadi, K., El Fellahi, A., & Lasri, T. (2016). Setting parameters influence on accuracy and stability of near-field scanning microwave microscopy platform. *IEEE Transactions on Instrumentation and Measurement*, *65*(4), 890-897.

[GU 17] Gu, S., Zhou, X., Lin, T., Happy, H., & Lasri, T. (2017). Broadband non-contact characterization of epitaxial graphene by near-field microwave microscopy. *Nanotechnology*, *28*(335702), 335702.

[HAD 11] Haddadi, K., Glay, D., & Lasri, T. (2011). A 60 GHz scanning near-field microscope with high spatial resolution sub-surface imaging. *IEEE Microwave and Wireless Components Letters*, *21*(11), 625-627.

[HAD 12] Haddadi, K., & Lasri, T. (2012, June). Interferometric technique for microwave measurement of high impedances. In *Microwave Symposium Digest (MTT), 2012 IEEE MTT-S International* (pp. 1-3).

[HAD 13] Haddadi, K., & Lasri, T. (2013). Scanning microwave near-field microscope based on the multiport technology. *IEEE Transactions on Instrumentation and Measurement*, *62*(12), 3189-3193.

[HAD 14] Haddadi, K., & Lasri, T. (2014). Interferometer-Based Microwave Microscopy Operating in Transmission Mode. *IEEE Sensors Journal*, *14*(7), 2226-2227.

[HAP 14] Happy, H., Haddadi, K., Theron, D., Lasri, T., & Dambrine, G. (2014). Measurement techniques for RF nanoelectronic devices: new equipment to overcome the problems of impedance and scale mismatch. *IEEE Microwave Magazine*, *15*(1), 30-39.

[HAN 08] Han, W. (2008). Introduction to scanning microwave microscopy. *Agilent application note*.

[HIL 00] Hillenbrand, R., & Keilmann, F. (2000). Complex optical constants on a subwavelength scale. *Physical Review Letters*, *85*(14), 3029.

[HOF 17] Hoffmann, K., & Baskakova, A. (2017, June). A new interferometric sensor for scanning near-field microwave microscopy. In *Microwave Measurement Conference (ARFTG), 2017 89th ARFTG* (pp. 1-4).

[HOW 96] Howland, R., Benatar, L., & Instruments, P. S. (1996). *A practical guide to scanning probe microscopy*. Park scientific instruments.

[HUM 11] Humer, I., Bethge, O., Bodnarchuk, M., Kovalenko, M., Yarema, M., Heiss, W., ... & Smoliner, J. (2011). Scanning microwave microscopy and scanning capacitance microscopy on colloidal nanocrystals. *Journal of Applied Physics*, *109*(6), 064313.

[IMT 03] Imtiaz, A., & Anlage, S. M. (2003). A novel STM-assisted microwave microscope with capacitance and loss imaging capability. *Ultramicroscopy*, *94*(3), 209-216.

[IMT 07] Imtiaz, A., Baldwin, T., Nembach, H. T., Wallis, T. M., & Kabos, P. (2007). Near-field microwave microscope measurements to characterize bulk material properties. *Applied physics letters*, *90*(24), 243105.

[IMT 10] Imtiaz, A., Wallis, T. M., Lim, S. H., Chisum, J., Popovic, Z., & Kabos, P. (2010, April). Near-field antenna as a scanning microwave probe for characterization of materials and devices. In *Antennas and Propagation (EuCAP), 2010 Proceedings of the Fourth European Conference on* (pp. 1-3). IEEE.

[ISA 17] Isakov, D., Stevens, C. J., Castles, F., & Grant, P. S. (2017). A Split Ring Resonator Dielectric Probe for Near-Field Dielectric Imaging. *Scientific Reports*, *7*.

[JUL 93] Julian Chen (1993). Introduction to Scanning Tunneling Microscopy (PDF). Oxford University Press. ISBN 0-19-507150-6.

[KIM 04] Kim, M., Kim, J., Kim, H., Kim, S., Yang, J., Yoo, H. & Friedman, B. (2004). Nondestructive high spatial resolution imaging with a 60 GHz near-field scanning millimeter-wave microscope. *Review of scientific instruments*, *75*(3), 684-688.

[KOC 89] Kochanski, G. P. (1989). Nonlinear alternating current tunneling microscopy. *Physical review letters*, *62*(19), 2285.

[LAI 07] Lai, K., Ji, M. B., Leindecker, N., Kelly, M., & Shen, Z. X. (2007, March). Near-field scanning microwave microscope with separated excitation and sensing probes. In *APS Meeting Abstracts*.

[LIN 17] Lin, T., Gu, S., & Lasri, T. (2017). Highly sensitive characterization of glucose aqueous solution with low concentration: Application to broadband dielectric spectroscopy. *Sensors and Actuators A: Physical*, *267*, 318-326.

[MAL 14] Malyuskin, O., & Fusco, V. (2014). Resonantly loaded apertures for sub-diffraction near-field imaging and surface probing. *IET Microwaves, Antennas & Propagation*, *9*(6), 533-540.

[MAL 16] Malyuskin, O., & Fusco, V. F. (2016). High-resolution microwave near-field surface imaging using resonance probes. *IEEE Transactions on Instrumentation and Measurement*, *65*(1), 189-200.

[MAL 17] Malyuskin, O., & Fusco, V. (2017). Super-Resolution Defect Characterization Using Microwave Near-Field Resonance Reflectometry and Cross-correlation Image Processing. *Sensing and Imaging*, *18*(1), 7.

[MIC 15] Michalas, L., Wang, F., Brillard, C., Chevalier, N., Hartmann, J. M., Marcelli, R., & Theron, D. (2015). Modeling and de-embedding the interferometric scanning microwave microscopy by means of dopant profile calibration. *Applied Physics Letters*, *107*(22), 223102.

[MIR 04] Mironov, V. L. (2004). Fundamentals of scanning probe microscopy. *Nizhniy Novgorod*, *38*.

[MON 17] Monti, T., Udoudo, O. B., Sperin, K. A., Dodds, C., Kingman, S. W., & Jackson, T. J. (2017). Statistical description of inhomogeneous samples by scanning microwave microscopy. *IEEE Transactions on Microwave Theory and Techniques Volume: 65, Issue: 6,* 2162 – 2170.

[PLA 11] Plassard, C., Bourillot, E., Rossignol, J., Lacroute, Y., Lepleux, E., Pacheco, L., & Lesniewska, E. (2011). Detection of defects buried in metallic samples by scanning microwave microscopy. *Physical Review B*, *83*(12), 121409.

[REN 09] Ren, Z., Boybay, M. S., & Ramahi, O. M. (2009, September). Near-field subsurface detection in lossy media using single split resonator probe. In *Wireless Sensing, Local Positioning, and RFID, 2009. IMWS 2009. IEEE MTT-S International Microwave Workshop on* (pp. 1-3). IEEE.

[REN 11] Ren, Z., Boybay, M. S., & Ramahi, O. M. (2011). Near-field probes for subsurface detection using split-ring resonators. *IEEE Transactions on Microwave Theory and Techniques*, *59*(2), 488-495.

[SAF 14] Safari, S., Castellazzi, A., & Wheeler, P. (2014). Experimental and analytical performance evaluation of SiC power devices in the matrix converter. *IEEE Transactions on Power Electronics*, *29*(5), 2584-2596.

[SOO 62] R. F. Soohoo (1962), "A Microwave Magnetic Microscope", vol. 33, pp. 1276, 1962.," J. Appl. Phys., vol. 33, p. 1276.

[SUN 14] Sun, W., Yang, Y., Wu, Z., Feng, T., Zhuang, Q., Peng, L. M & Ong, C. K. (2014). Penetrative imaging of sub-surface microstructures with a near-field microwave microscope. *Journal of Applied Physics*, *116*(4), 044904.

[STE 98] Steinhauer, D. E., Vlahacos, C. P., Dutta, S. K., Feenstra, B. J., Wellstood, F. C., & Anlage, S. M. (1998). Quantitative imaging of sheet resistance with a scanning near-field microwave microscope. *Applied physics letters*, *72*(7), 861-863.

[SYD 09] Sydoruk, O, Tatartschuk, E, Shamonina, E, & Solymar, L. (2009). Analytical formulation for the resonant frequency of split rings. *Journal of applied physics*, *105*(1), 014903.

[SYN 28] E. H. Sygne (1928), "A Suggested Method for Extending Microscopic Resolution into the Ultra- Microscopic Region," Philos. Mag., vol. 6, p. 356.

[TAB 99_a] Tabib-Azar, M., Pathak, P. S., Ponchak, G., & LeClair, S. (1999). Nondestructive superresolution imaging of defects and nonuniformities in metals, semiconductors, dielectrics, composites, and plants using evanescent microwaves. *Review of Scientific Instruments*, *70*(6), 2783-2792.

[TAB 99_b] Tabib-Azar, M., Akinwande, D., Ponchak, G., & LeClair, S. R. (1999). Novel physical sensors using evanescent microwave probes. *Review of Scientific Instruments*, *70*(8), 3381-3386.

[TAB 99_c] Tabib-Azar, M., Akinwande, D., Ponchak, G. E., & LeClair, S. R. (1999). Evanescent microwave probes on high-resistivity silicon and its application in characterization of semiconductors. *Review of Scientific Instruments*, *70*(7), 3083-3086.

[TAB 99_d] Tabib-Azar, M., Su, D. P., Pohar, A., LeClair, S. R., & Ponchak, G. (1999). 0.4 μm spatial resolution with 1 GHz (λ= 30 cm) evanescent microwave probe. *Review of Scientific Instruments*, *70*(3), 1725-1729.

[TAB 04] Tabib-Azar, M., & Wang, Y. (2004). Design and fabrication of scanning near-field microwave probes compatible with atomic force microscopy to image embedded nanostructures. *IEEE Transactions on Microwave Theory and Techniques*, *52*(3), 971-979.

[TUC 17] Tuca, S. S., Kasper, M., Kienberger, F., & Gramse, G. (2017). Interferometer Scanning Microwave Microscopy: Performance Evaluation. *IEEE Transactions on Nanotechnology*.

[TSE 05] Tseng, A. A., Notargiacomo, A., & Chen, T. P. (2005). Nanofabrication by scanning probe microscope lithography: A review. *Journal of Vacuum Science & Technology B: Microelectronics and Nanometer Structures Processing, Measurement, and Phenomena*, *23*(3), 877-894.

[TSE 13] Tselev, A., Lavrik, N. V., Kolmakov, A., & Kalinin, S. V. (2013). Scanning Near-Field Microwave Microscopy of VO2 and Chemical Vapor Deposition Graphene. *Advanced Functional Materials*, *23*(20), 2635-2645.

[WAN 90] M. S. Wang and J. M. Borrego (1990), "High-Resolution Scanning Microwave Electric-Field Probe for Dielectric Constant Uniformity Measurement," Mater. Eval., pp. 1106– 1109.

[WAN 07] Wang, R., & Tabib-Azar, M. (2007). Noncontact evanescent microwave magnetic dipole probe imaging of ferromagnets. *IEEE transactions on magnetics*, *43*(7), 3165-3170.

[WEB 14] J. C. Weber, P. T. Blanchard, A. W. Sanders, A. Imtiaz, T. M. Wallis, K. J. Coakley, K. A. Bertness, P. Kabos, N. A. Sanford, and V. M. Bright (2014). "Gallium nitride nanowire probe for near-field scanning microwave microscopy." Appl. Phys. Lett., vol. 104, 023113.

[WIE 94] Wiesendanger, R. (1994). *Scanning probe microscopy and spectroscopy: methods and applications*. Cambridge University Press.

[WIL 89] Williams, C. C., Hough, W. P., & Rishton, S. A. (1989). Scanning capacitance microscopy on a 25 nm scale. *Applied physics letters*, *55*(2), 203-205.

[WIL 95] Wilbur, J. L., Biebuyck, H. A., MacDonald, J. C., & Whitesides, G. M. (1995). Scanning force microscopies can image patterned self-assembled monolayers. *Langmuir*, *11*(3), 825-831.

[WU 04] Wu, X., & Ramahi, O. M. (2004, June). Near-field scanning microwave microscopy for detection of subsurface biological anomalies. In *Antennas and Propagation Society International Symposium, 2004. IEEE* (Vol. 3, pp. 2444-2447). IEEE.

[WU 15] Wu, Z., Sun, W. Q., Feng, T., Tang, S. W., Li, G., Jiang, K. L & Ong, C. K. (2015). Imaging of soft material with carbon nanotube tip using near-field scanning microwave microscopy. *Ultramicroscopy*, *148*, 75-80.

[WU 17] WU, B., SHENG, X. Q., & HAO, Y. (2017). Full-wave broadband modelling of near field scanning microwave microscopy. *Scientific Reports 7, Article number: 1606.*

[YAN 16] Yang, C. L., Lee, C. S., Chen, K. W., & Chen, K. Z. (2016). Noncontact measurement of complex permittivity and thickness by using planar resonators. *IEEE Transactions on Microwave Theory and Techniques*, *64*(1), 247-257.

Chapter II

Interferometer based near-field microwave microscope (iNFMM)

Chapter II : Interferometer based near-field microwave microscope (iNFMM)

II.1 Introduction

Despite the good performance in subsurface imaging and the ability to measure physical properties of materials, the NFMM faces several limits including the matching issue, the measurement noise, the probe robustness issue and the signal instability. These limitations are briefly discussed in chapter I and some promising approaches are proposed to solve them. For example, the matching issue describing the impedance mismatch between the high impedance EMP (tens or hundreds of kΩ) and the microwave measurement system (VNA with 50 Ω characteristic impedance) is one of the most important bottlenecks. Actually, without a matching system, the majority of the signal coming from the VNA is reflected by the probe, leading to a poor measurement sensitivity. To handle this problem, a matching network is therefore necessary. This kind of system can be divided into two categories: resonator based and interferometer based one. These two matching systems have been demonstrated theoretically in section I.3.4. Thanks to its broadband performance and adjustable Q factor, the interferometer-based matching network is selected to be part of our homemade NFMM.

Even though the matching problem is solved, the signal drift and noise issues still remain a huge challenge during the measurement and data analysis procedure. As mentioned in section I.3.3, one can use an acoustic isolation chamber [CHI 12] or a marble isolation stage [GU 16_a] together with a high precision XYZ scanner to minimize the influences brought by the environment and the mechanical vibration from the XYZ scanner. Nevertheless, the noise as well as the measurement uncertainties cannot be fully eliminated. A previous study has shown that they are also directly linked to the setting parameters of the NFMM system [GU 16_d]. Thus, a fine selection of parameters setting will help for the reduction of noise and improvement of measurement stability, which is described in details in this chapter.

Once the measurement stability as well as the measurement noise performance are improved, the last but the not least important problem related to the probe robustness issue is under evaluation. Generally speaking, the probe tip apex size as well as the stand-off distance (distance between the sample and the probe) dominate the imaging resolution (both the lateral and in-depth resolutions). To achieve a good imaging performance, a smaller tip apex size is always preferred and leads to a shorter stand-off distance. However, without a feedback system (for our homemade NFMM system), the stand-off distance cannot be constant and the probe has a risk to touch the sample. Moreover, the probe is always fragile when the tip is small. Thus, a compromise has to be considered between the probe tip apex size and the probe robustness.

In this chapter, a homemade interferometer-based NFMM is briefly described as a consecutive work to Bakli's and Gu's studies in MITEC group [Bak 15] [GU 16_c]. The iNFMM is introduced in two parts. The first one starts with a brief description of the iNFMM setup, where the main components are presented. Thanks to the characterization results of each component, the interferometer based system is simulated by ADS™. After that, since the measurement precision as well as the noise figure is related to the setting parameters, their influence is discussed. Finally, the measurement errors are carefully evaluated based on previous research works [GU 16_d]. The second part shows the imaging performance of the proposed iNFMM, in both surface and subsurface situations. The 1D and 2D images are constructed by considering the setting parameters previously determined. To improve the image quality, some image treatment methods such as position/signal difference method [KAN 03], adaptive robust statistic and local regression methods [CLE 79] and likelihood estimation method [TIB 89] are respectively applied to the images. With the help of these image treatment approaches, a better imaging quality is achieved.

II.2 Brief description of the iNFMM

II.2.1 Introduction

In this section, a brief description of the iNFMM is given for a better understanding of the system performance. Firstly, the configuration of the iNFMM including the setup and the components inside is demonstrated. In the second part, the interferometer-based matching network is simulated with the help of ADS™. After that, based on the previous research work [GU 16_d], the measurement precision and repeatability are carefully evaluated.

II.2.2 Configuration of the iNFMM

As mentioned in section I.3, the interferometer-based NFMM is made of an evanescent microwave probe (EMP), a broadband hybrid coupler, a high precision motorized XYZ stage, a camera, a vector network analyser (VNA), an impedance tuner and a data acquisition system with Labview™ integrated inside.

The configuration of the iNFMM is given in Figure II-1. The broadband hybrid coupler is connected to the port 1 and port 2 of the VNA (Keysight PNA-X 5242A / 10 MHz - 26.5 GHz). Its direct path is linked to the EMP while the coupling path is connected to the impedance tuner which is built up with a delay line and an attenuator. One can note that the signal generated by the VNA is transmitted separately into two parts by the 3 dB hybrid coupler. The first part arrives to the EMP to interact with the sample and results in a reflected signal (Γ_{EMP}). The second part reaches the impedance tuner and is reflected back to the hybrid coupler (Γ_{TUN}). These two reflected signals are combined in the hybrid coupler. The signal measured by the VNA can therefore be calculated simply by the following equation:

$$S_{21} = \frac{1}{2}(\Gamma_{TUN} + \Gamma_{EMP}) \qquad (II-1)$$

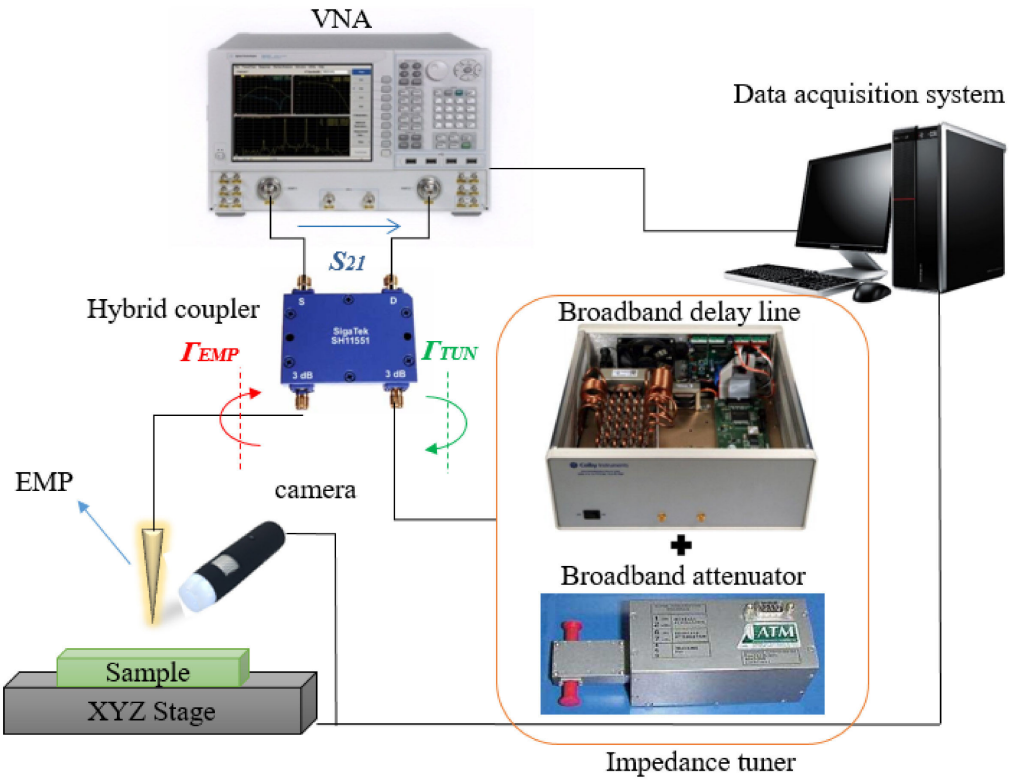

Figure II-1: Near-field microwave microscope configuration based on interferometry.

One has to note that the signal is measured in a transmission mode to overcome the main limitation encountered when using VNAs in terms of directivity errors, especially for the measurement of small signals. Furthermore, to achieve a high matching between the EMP and the VNA, one has to adjust the impedance tuner and null the transmission coefficient (S_{21}) by generating a signal (Γ_{TUN}) with equal magnitude but opposite phase compared to the signal reflected by the sample (Γ_{EMP}). This is the principle of the interferometer-based matching network as already mentioned in the section I.3.4.2.

The high precision XYZ stage helps to control the tip-sample distance and to scan accurately the sample during the imaging process. In our case, the EMP remains fixed while the sample is moved under the tip to keep a high measurement stability. Actually, in terms of precision, it is better to keep the microwave part of the system fixed. A camera is installed beside the EMP to help for the localization of the tip and sample interaction. In this setup, the data acquisition system has two functions. The first one acts as an interface to control the VNA and the XYZ stage with the help of Labview™. The second mission is

to collect the measurement data from the VNA. Finally, the measurement data are analysed according to the different applications.

As a summary, a brief description of the iNFMM configuration is given in this section. All the components as well as their functions are described. Thanks to the characterization of the components done by Gu [GU 16_c], the system simulation is performed by ADS™ in order to evaluate its performance. The results of this investigation is given in the next section.

II.2.3 Evaluation of the interferometric technique

Based on the characterization results of the components measured by Gu [GU 16_c], the operating frequency of the iNFMM is set from 2 to 18 GHz. This broadband frequency range is mainly governed by the working frequency range of the coupler and the impedance tuner. Concerning the coupler, in fact two couplers are used to cover this large frequency range. The first one covers the frequency range from 2 to 10 GHz and the other one operates in the range from 6 to 18 GHz. In the case of the impedance tuner, the attenuator and the phase shifter integrated inside work from 2 to 18 GHz. Thus, the working frequency range of the iNFMM spans from 2 to 18 GHz.

After the selection of the working frequency of the iNFMM system, its performance is evaluated both by simulation and measurement. In the tests presented thereafter, the EMP apex size is about 66 µm. The VNA generates an input signal with a power of 0 dBm and the intermediate frequency bandwidth (IFBW) is set to 100 Hz. Thanks to the transmission mode measurement, the noise floor of the VNA (Keysight™ PNA-X 5242A network analyzer) is reduced from -70 dB (reflection mode) to about -95 dB. For the demonstration, the frequency range is set from 2 to 3 GHz with a frequency step of 10 kHz. The measurement is carried out at room temperature (20°C).

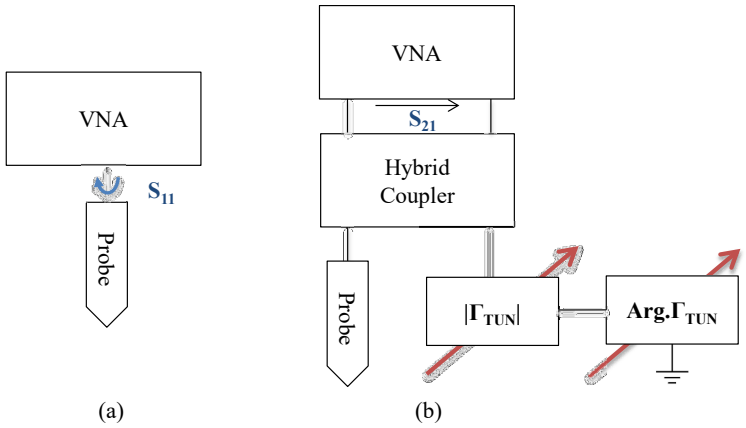

Figure II-2: Schematic of the different configurations simulated by Keysight™/ADS, (a): without interferometer, (b): with interferometer [GU 16_c].

With the conditions given above, two configurations are evaluated as illustrated in Figure II-2: with or without the interferometer. One has to note that the obtained signal is the reflection coefficient (S_{11}) for the case without the interferometer. Whereas in case of the setup including interferometer, the transmission coefficient (S_{21}) is measured. The measurement results obtained by GU are compared with the Keysight™/ADS™ simulation results in Figure II-3.

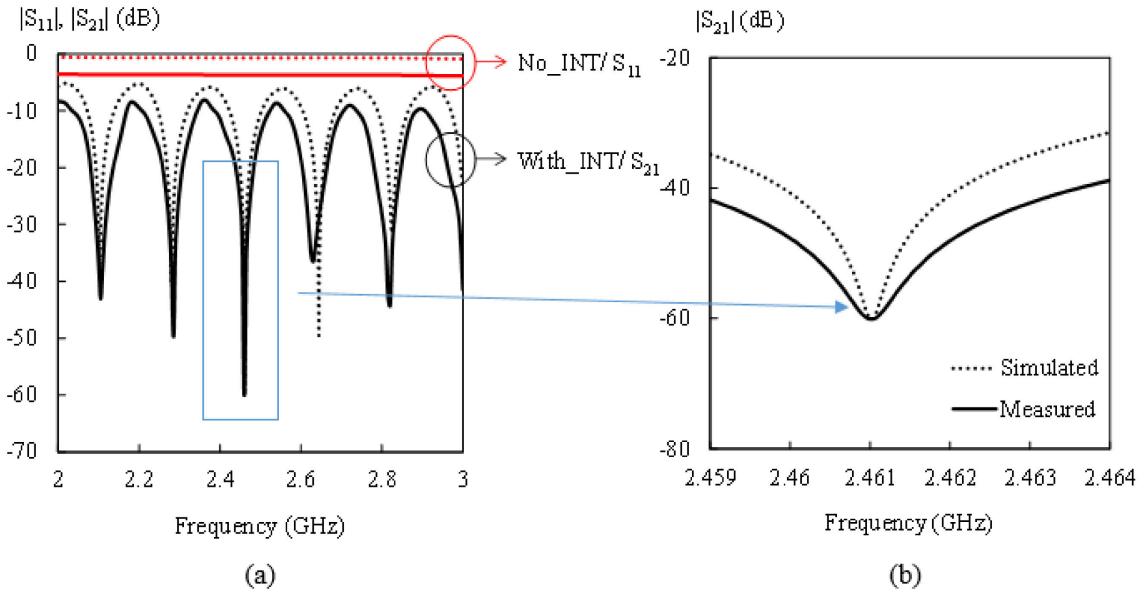

Figure II-3: (a) Measured (solid lines) and simulated (dotted lines) magnitude spectra in two cases: with (in black) and without (in red) interferometer; P_0 = 0 dBm, IFBW = 100 Hz, EMP apex size= 66 µm. (b) The close-up figure around 2.461 GHz [GU 16_c].

As can be seen in Figure II-3.a, in case of the setup without interferometer, the simulated reflection coefficient is almost constant, around -0.7 dB, and the measured one shows a magnitude level 3 dB lower. This difference is mainly due to the attenuation of the connection cables. Moreover, it indicates that the majority of signal is reflected by the EMP and leads to a low measurement sensitivity.

However, in case of the setup with interferometer, resonances appear in both simulation and measurement results. One can find out six resonances with a step of 170 MHz from 2 to 3 GHz and each of them gives different cancellation level (peak value). Furthermore, the difference between the simulation and measurement results is also around 3 dB, which corresponds to the case without interferometer. As already said, this difference is due to the attenuation of the connection cables. As can be seen from Figure II-2, two cables are connected between the coupler and the VNA whose loss is about 1.5 dB for each. In fact, the loss is not taken into account while it affects the measurement results during the simulation,

If we zoom the resonance around 2.461 GHz, we can observe the difference between the simulation and measurement results in terms of quality factor (Q factor). This latter represents the energy loss relative to the stored energy of the resonator. In our case, a higher Q factor indicates a lower cancellation level which means a better sensitivity towards to the variation of the sample physical property.

Compared to the simulation result which shows a Q factor of 10254, the one of the measured result is actually 4922 at the same cancellation level. In fact, this Q factor is not fixed and the resonance can be adjusted in terms of cancellation level and frequency by the combination of the attenuator and the delay line. Indeed, the attenuator adjusts the magnitude of the signal while the delay line changes its resonance frequency. These influences have been demonstrated by Gu [GU 16_b].

As mentioned in the previous part of this section, the operating bandwidth of our iNFMM system depends on the components working frequency. In our case, a working frequency range from 2 to 18 GHz can be achieved. Nevertheless, since the characteristic

of each component varies with the frequency, the Q factor of the system is not fixed for the entire frequency range. So, the evaluation of the Q factor in the entire frequency band becomes necessary. To this end, the measurement of the Q factor has to be carried out. Similar to the previous setup, the setting parameters including the IFBW, the power and the frequency points are selected. However, in this case the cancellation level is different, which is set around -75 dB. The reason to choose this value is due to the compromise between the signal stability and noise level. Actually, when the cancellation level is chosen close to the noise floor (-95 dB), the signal shift becomes more significant. Moreover, a proper signal to noise level should be considered to avoid the noise influence. So, based on these considerations, a cancellation level of -75 dB is selected by carefully adjusting the impedance tuner.

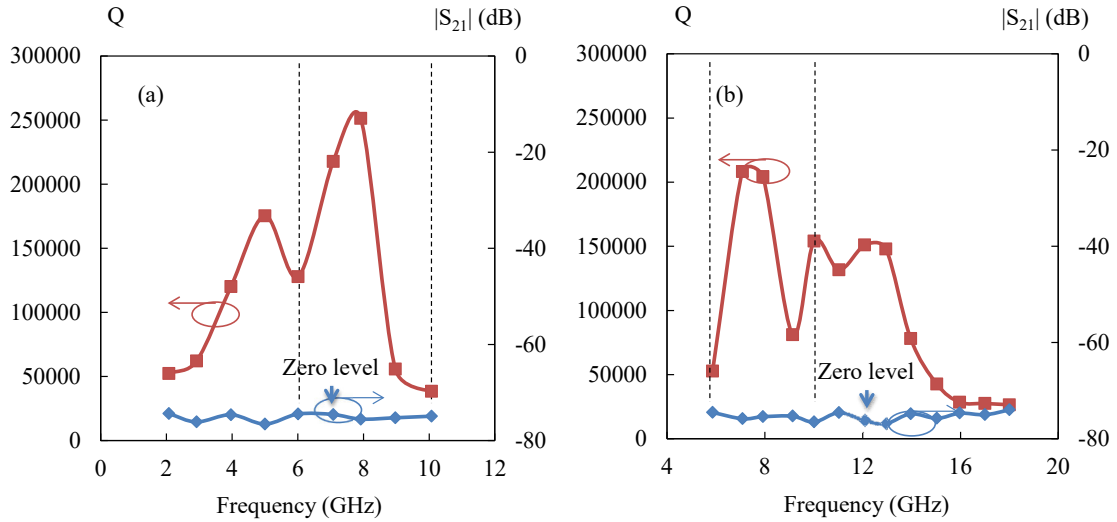

Figure II-4: Quality factors measured (in red) as a function of the frequency considering the zero level around -75 dB (in blue); (a): results when using the [2-10 GHz] coupler; (b): results when using the [6-18 GHz] coupler; the wave-cancelling process is done considering the probe in air [GU 16_c].

The measurement results of the Q factor in the entire frequency band is given in Figure II-4. As mentioned in the previous part, two couplers are used in our iNFMM whose frequency ranges help to cover the whole frequency band. Consequently, the Q factors are measured separately for these two couplers. For the first one which covers the frequency range from 2 to 10 GHz, the maximum Q factor is achieved near 8 GHz (260000) and the average value is about 100000. For the second coupler which works from 6 to 18 GHz, the

highest Q factor (200000) is also obtained round 8 GHz. All the Q factors are larger than 24000 in the entire frequency band. Compared to the Q factor measured by transmission line based structures in the order of 1000 or resonator based platforms in the order of 5000, the interferometer-based matching network shows a much higher value, which leads to a better measurement sensitivity [TAB 00], [KLE 06], [WEB 12], [SUN 14], [GRE 16].

II.2.4 Measurement repeatability study

The improvement of measurement sensitivity brought by the interferometer-based matching network was briefly introduced in the previous part. In this section, the measurement repeatability and uncertainty are investigated. In fact, the measurement repeatability can be ensured in two steps: the first step is to establish a proper measurement protocol and the second one is to study the parameters which influence the measurement results. In our case, for a NFMM, a similar work has been down by J.T Case and his colleagues. They have studied the influence of setting parameters including the stand-off distance and the scanning step size on the measurement results [CAS 11]. Inspiring by this work, the setting parameters in the iNFMM are well identified and their influences on the measurement repeatability and precision are studied in the following part.

II.2.4.1 The setting parameters

In our iNFMM system, the setting parameters are mainly divided into two parts: the VNA setting parameters and the platform parameter. Indeed, as shown in Figure II-5, they can be found in the control interface which is programmed by Labview™ and inserted in the data acquisition system.

The platform parameters are defined including the scanning step size S, the sampling surface (displacement in X and Y directions) and the stand-off distance H. The scanning step size S describes the horizontal distance between each displacement of the scanner, which can be seen as a pixel. Its minimum value is equal to the minimum increment step of the XYZ stage, which is 1µm. The sampling surface defines the sample scanning surface. In our case, the maximal scanning surface is 25 cm*25 cm in XY plane. The stand-off

distance is the separation between the probe and the sample, which varies in our case from 1 µm to 1 cm in Z axis.

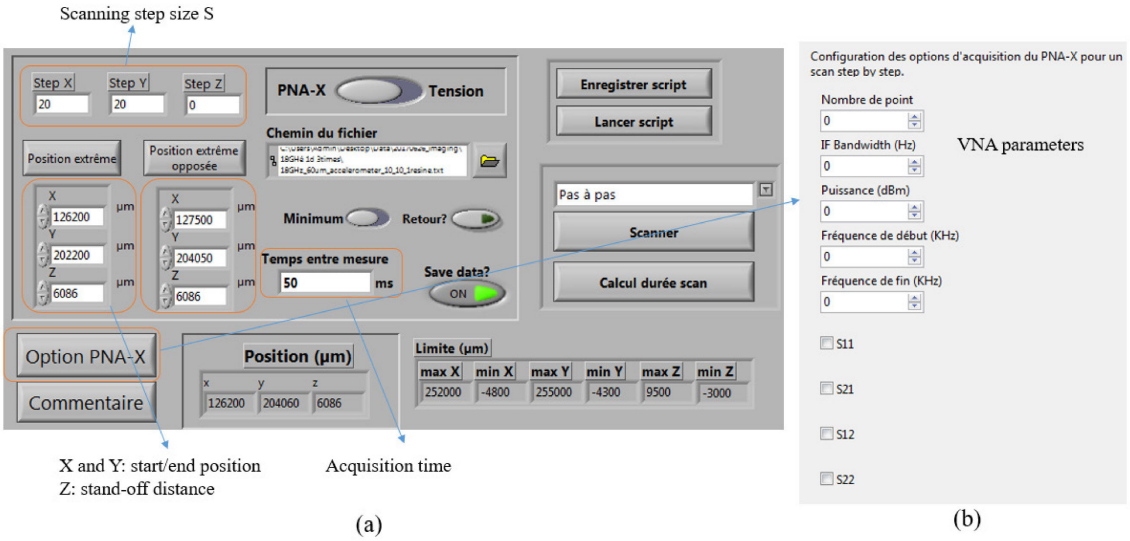

Figure II-5: The control interface inserted in the data acquisition system (a) platform parameters (b) VNA parameters.

After talking about the platform parameters given in Figure II-5.a, the VNA setting parameters are listed in Figure II-5.b, where the number of frequency points, IFBW, power, acquisition time, frequency range and the measurement mode can be found.

The number of frequency points is to construct the curve of the measured transmission coefficient in the selected frequency band. When this number increases, the response becomes more accurate. The IFBW, as already said, is the intermediate frequency bandwidth. For a conventional VNA, the receiver mix the detected microwave signal to a lower intermediate frequency (IF) by means of a local oscillator (LO). The obtained IF signal is bandpass filtered which narrows the receiver bandwidth and greatly improves the sensitivity, dynamic range and precision. The power is the power level of the signal delivered by the VNA. The acquisition time describes the time to collect the measured results. The frequency range is the frequency band where the measurements are performed and the measurement mode is set to the transmissions mode for a better signal to noise ratio.

The cancellation level (zero level) already introduced in the section II.2.2, is a very low level of the transmission coefficient S_{21} obtained when matching the high EMP impedance to the VNA impedance. This parameter can be adjusted manually thanks to the impedance tuner.

In this section, the setting parameters are introduced including the VNA setting parameters and the platform parameters. Their influences on the measurement precision are summarized in the next two parts.

II.2.4.2 Evaluation method of the setting parameters influence

In this section, the measurement precision influenced by the setting parameters is briefly summarized according to the work of GU [GU 16_d].

First of all, the standard deviation calculation is used as the evaluation method to estimate this influence. It is calculated from the obtained complex transmission coefficient and is given as:

$$Std(S_{21}) = \left(\frac{1}{n-1} \sum_{i=1}^{n} \left[\left(S_{21_i} - \overline{S_{21}} \right) \times \left(S_{21_i} - \overline{S_{21}} \right)^{*} \right] \right)^{\frac{1}{2}} \qquad (II-2)$$

The relative standard deviation is given by:

$$Std(S_{21})\% = 100\,\% \times \frac{std(S_{21})}{|\overline{S_{21}}|} \qquad (II-3)$$

Once the evaluation criterions are defined, the measurement precision, influenced by the setting parameters, can be evaluated quantitatively.

In fact, the measurement precision and repeatability of the iNFMM are mainly influenced by two error sources.

The first error source is related to the electrical part of the system including the VNA, coupler, impedance tuner and connection cables. At a fixed frequency, the coupler as well as the connection cables remains fixed during the measurement, so the error mainly varies with the setting parameters coming from the VNA and the impedance tuner. As mentioned in the previous section, the setting parameters for the VNA are the IFBW, the number of frequency points, the acquisition time whereas for the impedance tuner it is the zero level. Consequently, the measurement errors due to the variation of these parameters are evaluated individually.

The first setting parameter under estimation is the IFBW. According to the definition given in the section II.2.4.1 and the research results from GU [GU 16_d], the decreasing of IFBW leads to a lower noise floor but a longer acquisition time and finally results in a higher drift error. This error is calculated with the measurement conditions given as: the power is set to 0 dBm, the zero level is around -50 dB at 2 GHz when the probe is in free-space, the number of frequency points is 60, the acquisition time is set to 60 seconds and the IFBW varies from 1 Hz to 1000 Hz.

IFBW (Hz)	Std (S_{21} module) (%)	Std (S_{21} amplitude) (%)	Std (S_{21} phase) (%)
1	0.47	0.4	0.14
10	0.62	0.4	0.28
50	0.79	0.49	0.35
100	0.83	0.53	0.37
500	0.89	0.55	0.4
1000	1.46	0.91	0.66

Table II-1: Standard deviation of the transmission coefficient S_{21} as a function of IFBW; power = 0 dBm, zero level = -50 dB, f = 2 GHz, acquisition time = 60 s, number of frequency points = 60.

The standard deviation calculated for the transmission coefficient as a function of the IFBW ranging from 1 Hz to 1000 Hz is given in Table II-1. The errors due to the magnitude and the phase shift are also given separately for the complex transmission coefficient. Based on these results, one can note that the standard deviation increases with the increase of IFBW.

Once the influence due to the IFBW is determined, the influence of the number of frequency points is now under evaluation. As previously mentioned, a higher IFBW leads to a shorter acquisition time and a faster sampling speed. Thus, keeping the same measurement conditions, we vary the number of frequency points from 60 to 32000 according to different IFBW (1 to 1000 Hz). The obtained standard deviations as a function of number of frequency points are listed in the Table II-2.

IFBW (Hz)	Number of point	Std (S_{21}) (%)	Std ($\|S_{21}\|$) (%)	Std (arg.S_{21}) (°)
1	60	0.47	0.4	0.14
10	600	0.58	0.4	0.24
50	3000	0.73	0.43	0.32
100	6000	0.75	0.49	0.33
500	30000	0.78	0.49	0.35
1000	32001	0.89	0.69	0.35

Table II-2: Standard deviation of the transmission coefficient S_{21} as a function of the number of frequency points; power = 0 dBm, zero level = -50 dB, f = 2 GHz, acquisition time = 60 s.

When comparing the results from table II-2 to those given in table II-1, one can notice that the standard deviation of the transmission coefficient for a given IFBW decreases with the increase of the number of frequency points when the other conditions remain fixed.

After the determination of the influence of the IFBW and number of frequency points, the effect of the acquisition time is evaluated. For the demonstration, the number of frequency points is set to 600 and the IFBW is set to be 100 Hz. The other measurement conditions remain the same except for the acquisition time which varies from 5 minutes to 5 hours. The standard deviation of the transmission coefficient is given in the table II-3:

Acquisition time	Std (S_{21}) (%)	Std ($\|S_{21}\|$) (%)	Std (arg.S_{21}) (°)
5 min	0.52	0.35	0.29
5 hours	5.19	3.81	2.01

Table II-3: Standard deviation of the transmission coefficient S_{21} as a function of acquisition time; zero level = -50 dB, f = 2 GHz, number of frequency points = 600 and IFBW=100 Hz.

It is clear that the standard deviation of the transmission coefficient increases with a longer acquisition time when the others parameters are fixed. In fact, this conclusion is particularly important for imaging applications as a long acquisition time is sometimes

needed for a high resolution image. It is due to the fact that the signal acquisition time of each pixel is fixed, a high image quality can be reached only by obtaining larger number of pixels. However, this longer acquisition time, as demonstrated in table II-3, will result in a higher standard deviation of the results. Thus, a compromise should be considered between the acquisition time and the signal deviation (image quality).

Once the influence of the acquisition time is evaluated, the last parameter, zero level, is now investigated. By carefully adjusting the impedance tuner, the zero level can be set from -30 dB to -70 dB. For this study, the other parameters are kept the same as for the previous evaluation (power: 0 dBm, IFBW: 100 Hz, acquisition time: 5 mins and the number of frequency points: 600). The obtained standard deviation of the transmission coefficient as a function of zero level is listed in the following table.

Zero level (dB)	Std (S_{21}) (%)	Std ($\|S_{21}\|$) (%)	Std (arg.S_{21}) (°)
-30	0.12	0.10	0.04
-50	0.52	0.35	0.29
-70	5.36	4.28	1.85

Table II-4: Standard deviation of the transmission coefficient S_{21} as a function of the zero level; f = 2 GHz; P_0 = 0 dBm, IFBW = 100 Hz, acquisition time = 5 minutes, number of frequency points = 600.

It is retrieved in the table II-4 that the standard deviation increases with the decrease of zero level. When the zero level decreases from -30 dB to -70 dB, the signal deviation increases from 0.12% to 5.36%.

Another important source of error is related to the vibration of the XYZ scanner and its own scanning error. To minimize the stage vibration effect we have chosen to fix the microwave part of system during the experimentation to reduce this kind of error. However, the stage scanning error cannot be avoided and always occurs during the displacement of the scanner. According to the performance of our motorized XYZ stage, a 0.1 µm positioning uncertainty is theoretically estimated for each movement in X, Y and Z directions. To better understand the scanning error influence on the measurement repeatability, an experimentation is carefully conducted considering the setting parameters given in table II-5.

IFBW (Hz)	Acquisition time	Number of frequency points	Power	Frequency	Zero level
100	2 hours	600	0 dBm	2 GHz	-50 dB

Table II-5: Setting parameters for the test of measurement repeatability according to the scanning error of the XYZ scanner.

Once the setting parameters are defined, the experimentation is made according to two configurations as illustrated in the Figure II-6.

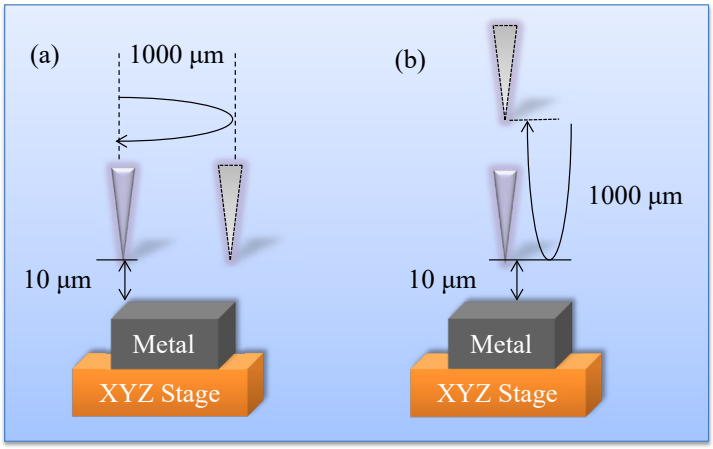

Figure II-6: Repeatability tests of the motorized stage in X/Y directions (a) and in Z direction (b), the displacement is performed by considering a step of 1000 µm.

The first configuration aims to test the measurement repeatability in X and Y directions while the second one concerns the Z direction of the motorized stage. For both configurations, the probe is positioned 10 µm over a metallic sample. The principle of these two configurations is that the sample is firstly displaced 1000 µm away from its original position and then moved back. This operation is repeated 10 times during 2 hours for both configurations. Based on the measurement results, the repeatability is estimated in table II-6.

Std (S_{21}) in X direction (%)	Std (S_{21}) in Y direction (%)	Std (S_{21}) in Z direction (%)
5.2	5.44	5.74

Table II-6: The estimated measurement repeatability in terms of standard deviation in X, Y and Z directions.

One can note that the standard deviations for the X, Y and Z directions are respectively equal to 5.2%, 5.44% and 5.74%.

As a summary, the measurement precision is mainly governed by the setting parameters including the IFBW, number of frequency points, acquisition time and zero level. For a specific application, these setting parameters have to be chosen according to the application requirements. For example, for a large surface imaging application, the acquisition time is long. Thus, to decrease the signal drift error and keep a good imaging quality, a low IFBW is preferred. On the other hand, with fixed setting parameters, the measurement repeatability is largely dependent on the performance of the motorized XYZ stage. The standard deviation for the three axis during 2 hours displacement is estimated around 5.5% (Table II-6).

II.2.5 Conclusion

As a conclusion, in this section the measurement repeatability is estimated. According to the study of the two main error sources which are related to the setting parameters and to the motorized stage, the impact on the measurement results is evaluated, which helps for the error estimation when different kinds of applications are targeted. For instance, imaging applications that are described in details in the following sections can be therefore carried out relying on these results.

II.3 The iNFMM imaging performance

II.3.1 Introduction

For all kinds of microscopy, the basic function is to image the sample under test. As introduced in the first chapter, unlike the traditional microscopy such as AFM and STM, the NFMM gives the opportunity for both surface and subsurface observations. Besides such an advantage, non-destructive and non-contact features are also considerable assets.

Generally, the sensitivity and spatial resolution are examined when talking about the imaging performance of a microscopy. Thus, in this section the sensitivity and spatial resolution of our iNFMM are evaluated both in surface and subsurface situations.

Indeed, the improvement of the iNFMM imaging performance is directly linked to the enhancement of the spatial resolution and measurement sensitivity. Thanks to the interferometer-based matching network, the sensitivity improvement is demonstrated in the work of Gu [GU 16_c]. The main routes to enhance the spatial resolution consist in decreasing the radius of the probe apex [IMT 06] and reducing the stand-off distance between the probe and the sample [GU 15]. Apart from these two possibilities, many groups have demonstrated various techniques to further increase the spatial resolution. For instance, J. Kim proves that the hybrid probe is a good candidate to avoid the low transmission efficiency of the miniaturized probe tip by a properly designed tapered part at 4.46 GHz [KIM 03]. A. Karbassi has proposed a quadaxial probe to remove the parallel effect of the coaxial shields which surrounds the center conductor at around 1 GHz [KAR 06]. Based on this configuration, the probe allows better electromagnetic localization compared to the conventional coaxial one. By taking advantage of an accurate analytical modelling and a careful choice of the optimal frequencies, G. Sardi shows the possibility of dielectric samples evaluation with maximum sensitivity at around 20 GHz [SAR 15].

Complementary to these methods for surface imaging, there is a strong interest for the characterization of buried structures. Indeed, one of the main advantages of microwave is its penetrating ability in materials. For instance, the group of Z. Ren has shown a significant enhancement of evanescent field energy by using a split-ring resonator for the subsurface detection [REN 11]. The transmission mode analysis which has been investigated by A. O. Oladipo shows that a more detailed information can be acquired compared to the reflection mode [OLA 14].

However, as the electromagnetic field is mainly located at the end of the probe, larger is the probe apex size, stronger is the penetration depth but poorer is the resolution. To overcome this dilemma and keep a good in-depth spatial resolution, Kantor and Shvets proposed a data treatment technique called position/signal difference (PSD) method [KAN

03]. This solution relies on the subtraction of the results obtained at two different stand-off distances in the near-field region. But, even with this resolution enhancement method, images are still noisy and easily contaminated by the test environment such as the VNA drift errors [GU 16_c] and the slight vibrations of the platform during the measurement. Another factor that decreases the image quality is the errors due to the sample tilt in particular when the scanning area is large. According to the adaptive robust statistical (ARS) method presented by K. J. Coakley [COA 15], the errors mentioned above could be reduced and the distorted images have a better chance to be corrected.

In this section, we firstly give the results of the investigation of the measurement precision as well as the lateral resolution in case of surface imaging. With the help of several numerical methods, the distortion caused by the noise and the sample tilt is largely reduced. Two examples including on chip test and large surface sample imaging are demonstrated thereafter. For the subsurface situation, different thicknesses of resins are deposited on the sample to investigate their influence on the imaging performance. The ARS imaging treatment method is applied to the obtained results and conclusions are drawn.

II.3.2 Surface imaging performance

II.3.2.1 1D imaging

In this section, we are mainly interested in the measurement precision and the lateral resolution of our homemade near-field microwave microscope. To improve its performance, the first idea is to consider the probe features. Actually, as already said, the radius of the probe apex and the distance between the probe and the sample under test have a strong influence on the measurement precision and the spatial resolution [IMT 06], [GU 15]. As mentioned, specific probes, such as hybrid and quadaxial probes have been used in order to improve the transmission efficiency and remove the parallel effect of the coaxial shields [KIM 03], [KAR 06]. However, based on cost and fabrication complexity consideration, these probes are not suitable for our iNFMM. Actually, a priority is given to the use of simple probes.

Thus, by carefully analysing the influence of the key parameters including the stand-off distance, the working frequency and the probe apex size, the best configuration is chosen to achieve a high measurement precision. Then, the position/signal difference (PSD) method is applied to further enhance the precision. After that, the lateral resolution of our iNFMM is investigated. The results of this investigation are described thereafter.

II.3.2.1.1 Sample preparation and measurement method

The sample preparation and the measurement method are introduced in this section. As depicted in Figure II-7.a, the experimental investigation to estimate the measurement precision is realized by measuring the width of gold lines (300 nm thickness) deposited on silicon substrate. The resistivity of the silicon substrate is about 5 KΩ.cm and the conductivity of the gold lines is $4.2 * 10^7$S/m. This huge impedance difference between the gold lines and the substrate makes that the lines can be easily detected. The width of the gold lines varies from 10 to 100 µm while the spacing between each line is fixed to 200 µm except for the one between the line of 10 µm and 20 µm, which is 100 µm.

For the lateral resolution, the evaluation is made by studying the possibility to distinguish two adjacent gold lines with different spacing as depicted in Figure II-7.b. The spacing between two gold lines is no longer the same but varies from 10 to 100 µm. The width of gold lines is fixed to 100 µm.

The interaction between the probe and the sample is illustrated in Figure II-7.c. The stand-off distance is fixed to 1 µm and the probe is set above the gold line with a width of 100 µm to set the zero level to -55dB. The probe is then displaced beside the gold line and the scanning direction is also indicated.

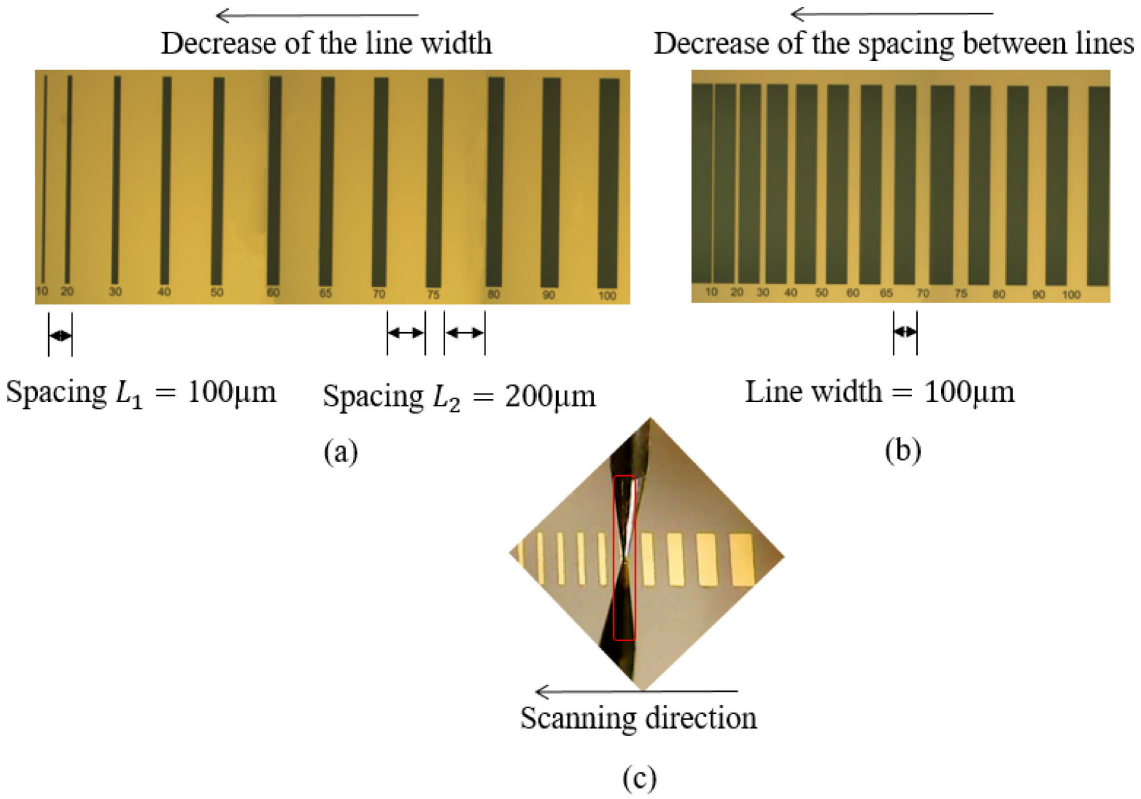

Figure II-7: Description of the sample under test: (a) gold lines with various width for the evaluation of measurement precision (b) gold lines with fixed width but different spacing for the lateral resolution study (c) the interaction between the probe and sample.

For demonstration of the measurement method, the sample chosen is indicated in Figure II-7.a. The parameters are a stand-off distance of 1 µm, an apex size of 70 µm and a frequency of 10 GHz. Since the test consists in the scan of a line of 100 µm, the scanning duration takes not very long time (less than 1 min for a scanning step size of 1 µm). In this study the zero level is chosen to be -55 dB. The VNA setting parameters are selected as 0 dBm for the power and 100 Hz for the IFBW.

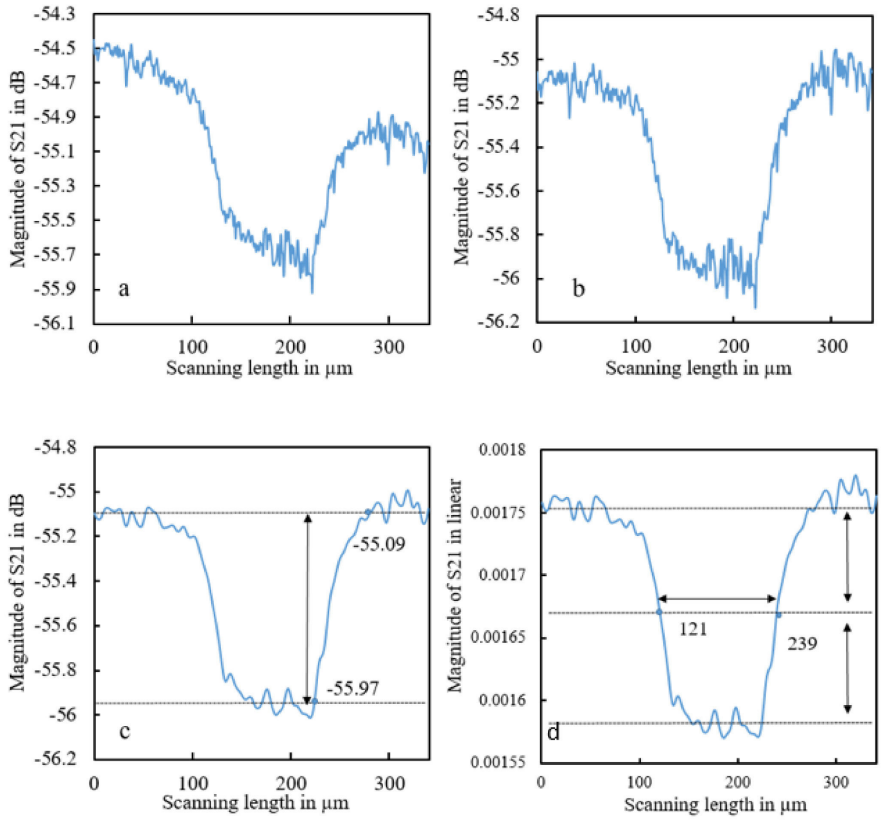

Figure II-8: Measured magnitude of the transmission coefficient S_{21} for a gold line of 100 µm width: (a) raw data, (b) balanced data, (c) denoised data, (d) linear balanced and denoised data.

Firstly, as shown in Figure II-8.a, the gold line is clearly detected. The returned S_{21} coefficient is slightly distorted due to the existence of measurement noise and tilt error coming from the sample. To remove the distortion, a simple algorithm is used to balance the signal (Figure II-8.b).

For the measurement noise consideration, the average option of VNA is set to be 20 times (measurement repeated 20 times and averaged at each point) to overcome the measurement instability. In addition, as shown in Figure II-8.c, a local regression and likelihood algorithm is applied to further reduce the noise without disturbing the original signal. The scanning contrast measured here is 0.88 dB. This value is considered as the signal sensitivity. We can also transform the magnitude of the transmission coefficient to linear values as illustrated in Figure II-8.d. In this plot, the measured line width is defined

by the full width at half maximum (FWHM) approach, where the width corresponds to the half of maximum amplitude [CAM 86]. In this case the width obtained is 118 µm.

As a conclusion, the 100 µm gold line can be clearly detected by means of our iNFMM. The major part of the noise can be eliminated and the sample tile problem is solved. The obtained signal reflects a line width of 118 µm according to the setting parameters and measurement condition. We show that this measurement precision can be further improved by acting on the measurement conditions.

II.3.2.1.2 Measurement precision study

After the demonstration of the measurement method and the gold line width determination, the measurement precision of the iNFMM is now under evaluation. Generally speaking, a high measurement precision can be reached by decreasing the probe apex size and reducing the stand-off distance. In our study the probe is an evanescent microwave probe (EMP) which means that the microwave signal vanishes very rapidly at the probe output. The simulation that demonstrates this effect is given in Figure II-9.a. In this study the tip apex size is 70 µm.

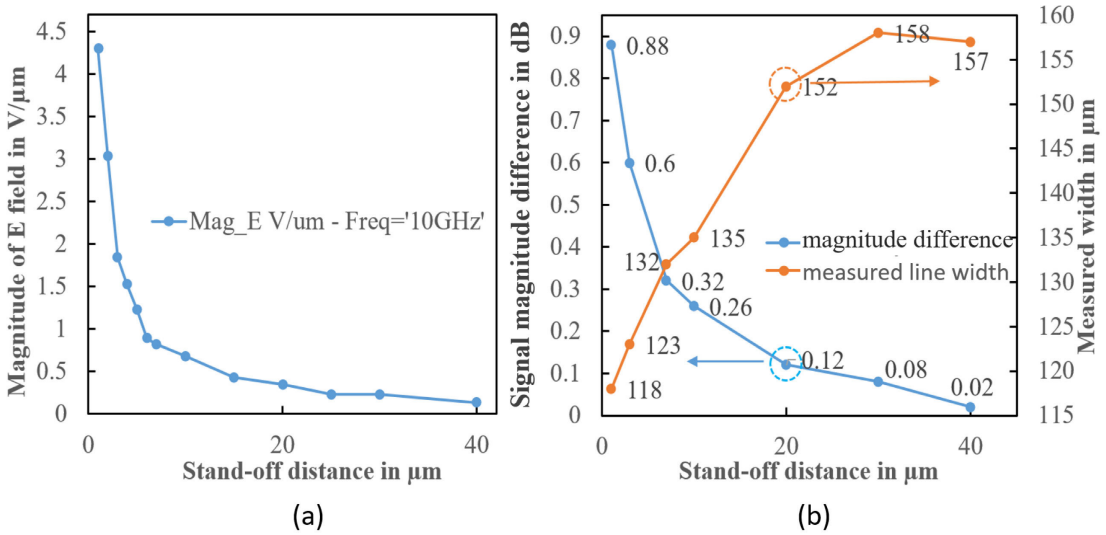

Figure II-9: (a) HFSS simulation of the electric field magnitude around the 70 µm probe tip for different stand-off distances H from 1 to 40 µm at 10 GHz (b) Signal magnitude difference measured with the iNFMM for different stand-off distances H from 1 to 40 µm and the corresponding width measured for a 100 µm-width line at 10 GHz.

The magnitude of the E-field tends to zero very quickly as a function of the stand-off distance. Thus, it is expected that the signal magnitude difference will also be affected in the same extent. To confirm this observation the sensitivity is measured for the same range of stand-off distances (0 to 40 µm).

As shown in Figure II-9.b, the measured signal magnitude difference obtained goes from 0.88 dB at 1 µm to 0.02 dB at 40 µm (almost undetectable). The corresponding calculated width raises with respect to a higher stand-off distance, which indicates a larger error rate compared to the original line width. Thus, to keep a good measurement precision on the width, a small stand-off distance has to be chosen. In the following test, the stand-off distance H is set at 1 µm.

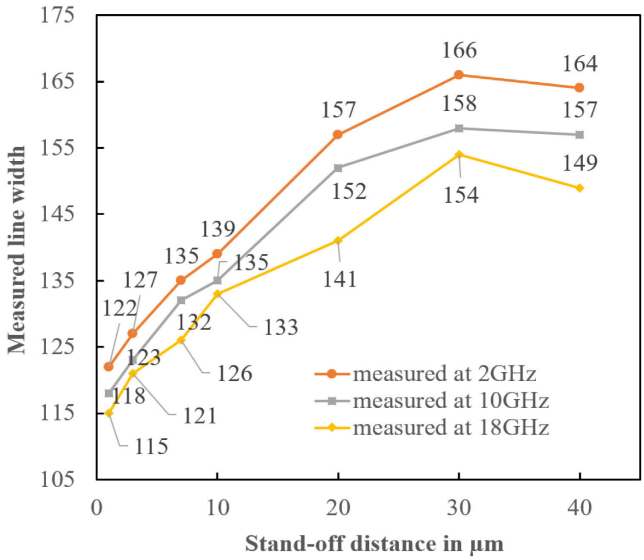

Figure II-10: Measured gold line width at different stand-off distances from 1 µm to 40 µm at 2, 10 and 18 GHz with a 70 µm EMP.

Since the measurement precision is also influenced by the wave length (λ), the working frequency f is an important parameter related to the measurement precision. Thanks to the broadband matching network, we can adjust the interaction between the probe and the sample under test at any frequency from 2 to 18 GHz with a high sensitivity [GU 16_b]. The impact of the frequency on the measurement precision is evaluated and the results are presented thereafter. For demonstration, three testing frequencies are

investigated: two values at the frequency band limit (2GHz and 18 GHz) and one at the middle of the working frequency band offered by the instrument (10 GHz). For these three frequencies the width of the gold line (100 µm) is evaluated as a function of the stand-off distance. The measurement results are given in Figure II-10.

As expected, the best result is obtained at the highest frequency (18 GHz) and the lowest stand-off distance (1 µm). Therefore, the working frequency of 18 GHz is retained for the following tests.

Apart from the two important parameters mentioned above (frequency, stand-off distance), the measurement precision is mainly governed by the tip apex size. Smaller the tip apex size better is the measurement precision. In this section, the improvement of measurement precision is assessed by using a smaller probe whose apex size is 30 µm. In this case we scan a set of lines with different width ranging from 10 µm to 100 µm. The sample under test for this experiment is the one described in Figure II-7.a. The stand-off distance H is fixed at 1 µm but the working frequency is set to 18 GHz.

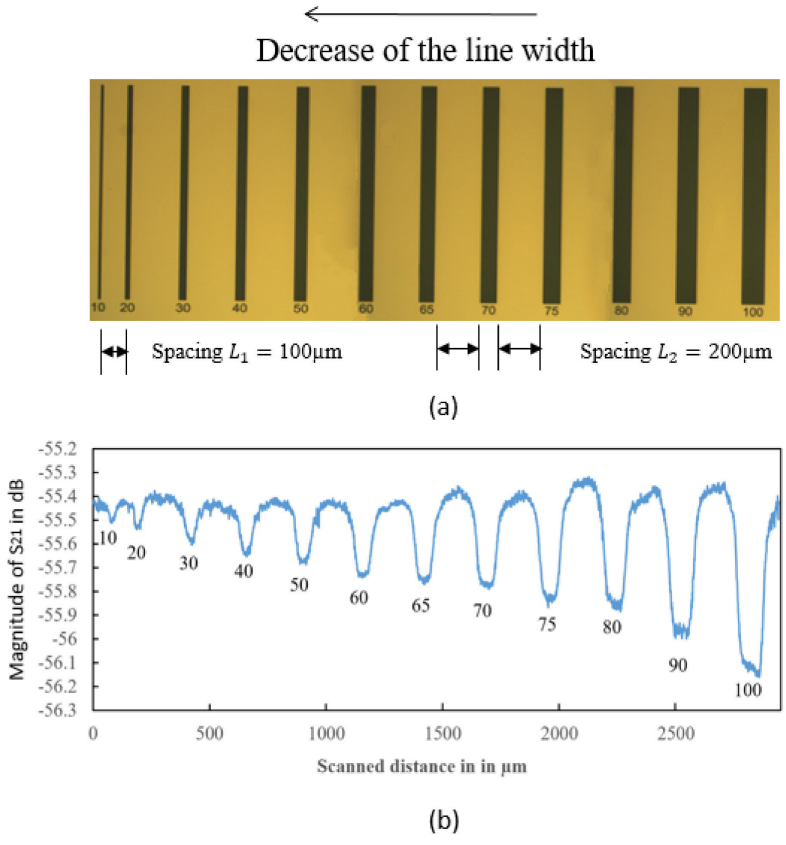

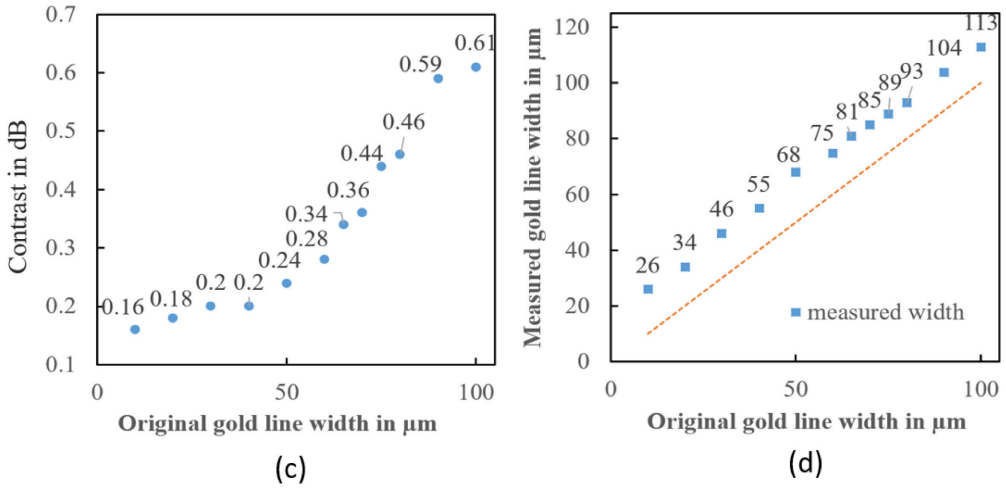

Figure II-11: (a) gold lines with various widths (b) Measured magnitude of the transmission coefficient S_{21} over a set of lines with different widths ranging from 10 to100 µm, tip apex= 30 µm, F= 18 GHz, H=1 µm (c) Measurement contrast for different gold lines (d) line width measured for each gold line compared to the original width.

As shown in Figure II-11.b, all the lines are detected and can be easily distinguished. One can also note that the probe with apex of 30 µm effectively detects the narrowest line width (10 µm) available on the sample. Obviously, it is observed that larger is the gold line width higher is the signal contrast (Figure II-11.c). When comparing the results obtained from the two probes (Figure II-10 and Figure II-11.b), one can note that the value returned for a line of 100 µm width is 115 µm and 113 µm respectively at 18 GHz. It is verified that the small probe gives a width slightly closer to the actual width. Thus, it is expected that a better precision is achievable if the size of tip is decreased even more.

Nevertheless, to ensure the robustness of the tip, particularly in case of 2D scanning, the minimum size for the tip is chosen to be 30 µm. So, in order to further improve the measurement precision, the choice is made to use signal processing tools and in particular the PSD method is applied.

As already mentioned and demonstrated in Figure II-12.a, the electric field is mainly focused around the tip apex. Nevertheless, the parasitic electric field coming from the other parts (middle section of the probe, coaxial shielding) also contributes in some extent to the interaction between the probe and the sample, which leads to a decay of measurement

precision. To remove such parasitic effect, the position/signal difference method is proposed. The model used to describe the probe sample interaction is given in Figure II-12.b [KAN 03].

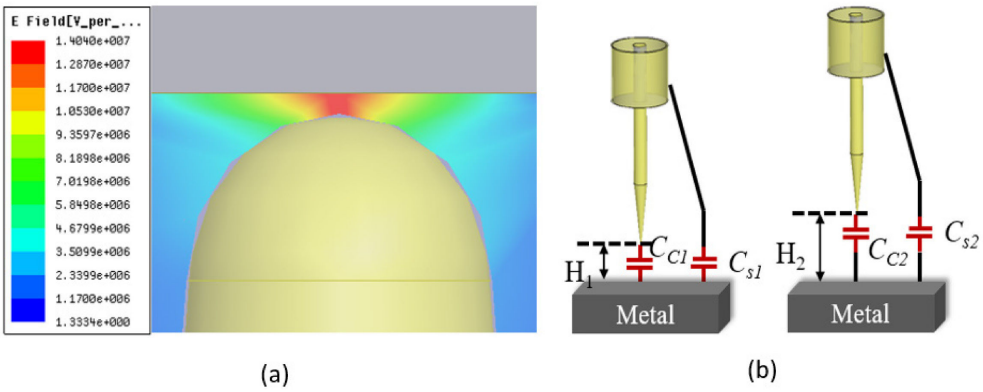

Figure II-12: (a) Simulation of the electric field magnitude for the probe tip in free space with Ansys™/HFSS. The image is taken at the cross-section along the probe, f = 18 GHz. (b) Model of probe and sample interaction with different stand-off distances.

Based on the model of the probe-sample interaction, the subtraction of the two signals collected at two stand-off distances is obtained by the following expression:

$$I_1 - I_2 = (C_{c1} + C_{s1}) - (C_{c2} + C_{S2})$$

C_{ci} (i = 1, 2) represents the capacitance between the probe and the sample and $C_{si}(i = 1,2)$ is the capacitance between the other parts of the probe and the target. The variation of C_{si} (i = 1, 2) with different stand-off distance H is considered very small. Thus this term can be ignored in the formula. In this way, the subtraction of the two signals leaves only the capacitance difference caused by the tip apex.

To apply this method two stand-off distances are selected. The first one is the smallest available (1 µm), which gives the most information on the sample. The second one is chosen close to the apex size (30 µm). To observe the improvement of the measurement precision brought by this method, three lines whose widths are chosen to be close to the probe apex size (20, 30 and 40 µm) are characterized by the method proposed.

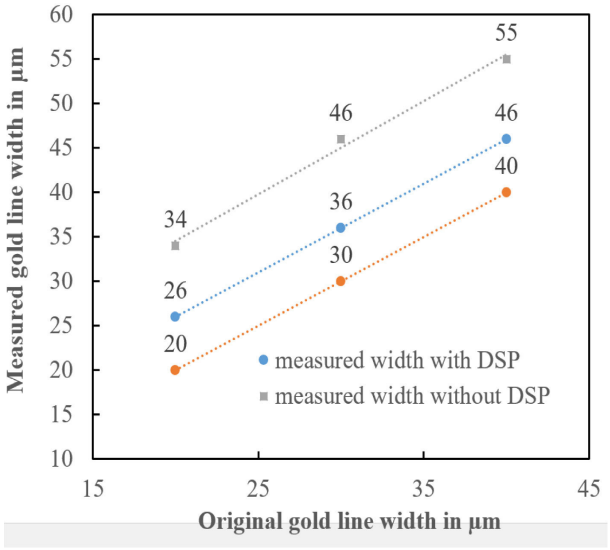

Figure II-13: Measured line width compared to the original width of gold lines from 20 µm to 40 µm with and without the DSP method.

Compared to the test without the DSP method (same condition as the results in Figure II-11), one can note that this solution reduces the difference between the measured width and the original width from about 15 µm to 6 µm as shown in Figure II-13.

As a conclusion of this section, an experimental investigation of the measurement precision is performed. Numerical signal treatment methods are applied to remove the sample tilt and to decrease the measurement noise. Afterward, the full width at half maximum (FWHM) approach is used to estimate the line width. The measurement precision is therefore analysed in terms of critical parameters such as stand-off distance, tip apex size and working frequency. Regarding the system characteristics, maximum available frequency (18 GHz) and smallest stand-off distance (1 µm), and considering the probe robustness (D = 30 µm), the solution to furthermore improve the measurement accuracy without decreasing the tip apex size consists in applying a signal processing technique. The position/signal difference method has been selected for its easy implementation. After the evaluation of the measurement precision, the lateral resolution study is performed in the next section.

II.3.2.1.3 Lateral resolution study

Generally, with the same conditions (a low zero level, a minimal stand-off distance, a reduced scanning step size and a tiny probe) to those retained for the measurement precision, a high lateral resolution can be reached. Nevertheless, attention has to be brought to the scanning duration and scanning area during the procedure establishment to obtain a high spatial resolution. In fact, often a compromise has to be found to ensure the best performance. In this investigation we are interested in the 1D lateral resolution of our iNFMM. The scanning duration is less than 5 minutes and the drift error is therefore considered very small (1%) as previously demonstrated (Table II-3).

In the following part, the lateral resolution mainly defined by the tip apex size is demonstrated. With the other setting parameters fixed (zero level = -55 dB, IFBW = 100 Hz, power = 0 dBm and stand-off distance = 1 µm), two EMP whose tip apex size are respectively 50 µm and 30 µm are used in this experimentation.

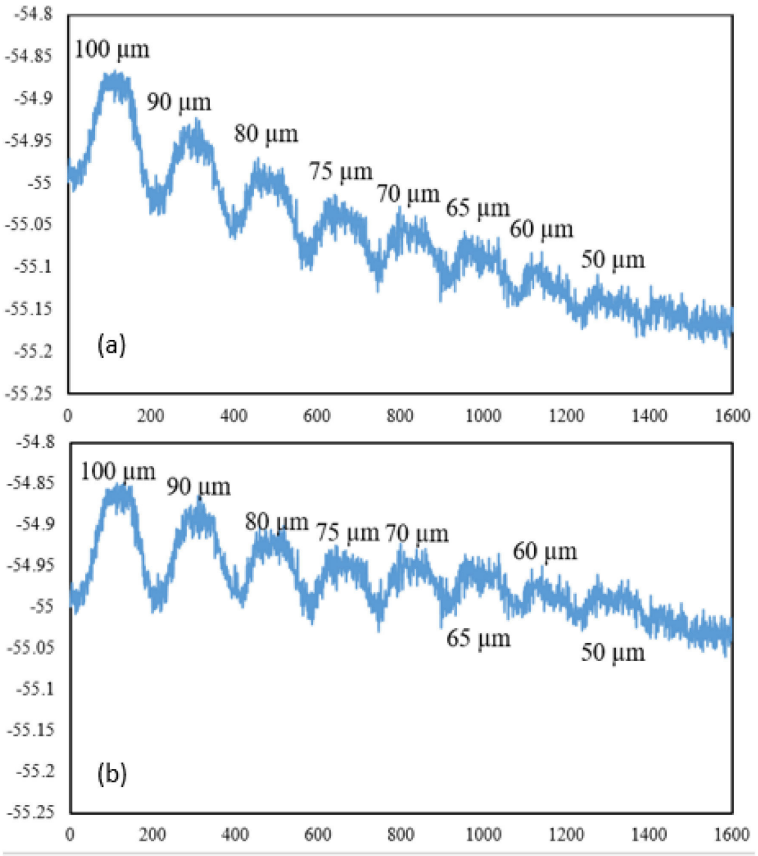

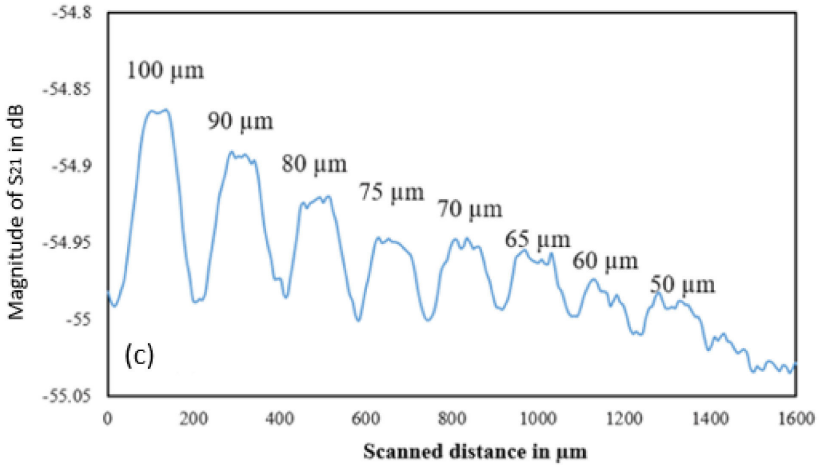

Figure II-14: Measured magnitude of the transmission coefficient S_{21} by an EMP of 50 µm tip apex size (a) raw data, (b) balanced data, (c) balanced and denoised data. Zero level = -55 dB, F = 18 GHz, H= 1 µm.

The results obtained are depicted in Figure II-14 for the first EMP (50 µm tip apex size). The sample under test is the one presented in Figure II-7.b. The raw data of the measured transmission coefficients magnitude are displayed in Figure II-14.a. The obtained signal is clearly distorted because of the existing sample tilt and the measurement noise. With such a result, the gold lines whose spacing varies from 100 to 60 µm can be distinguished according to the presence of clear peaks. The one with 50 µm width cannot be clearly distinguished since it is immersed into the noise.

After applying the balancing and denoise algorithms on the raw data, one can note that the obtained signal (Figure II-14.b) is balanced, which means each wave trough is set at the same signal level. Moreover, each signal peak represents a spacing between each two gold lines whose width varies from 100 to 50 µm. Based on this test, the lateral resolution in this case is found close to the tip apex size (50 µm).

We continue to reduce the tip apex size and observe its influence on the lateral resolution. In this case, the tip apex size varies from 50 to 30 µm. The same test is conducted by using the tip of 30 µm width. The results are given in Figure II-15.

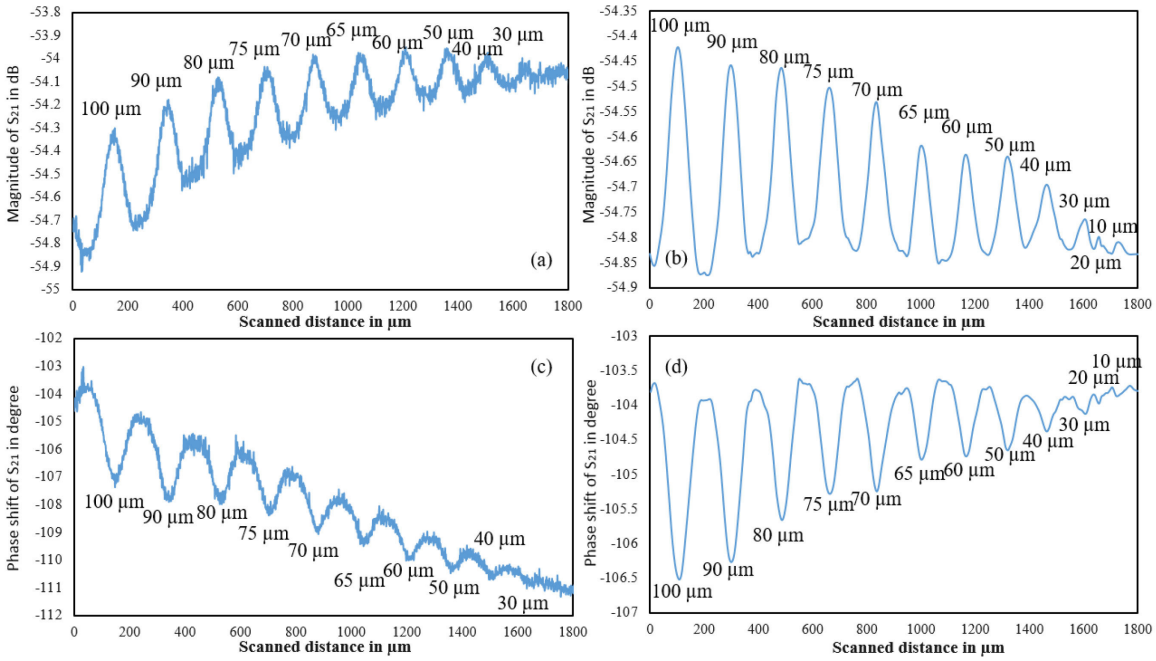

Figure II-15: Measured magnitude and phase shift of the transmission coefficient S_{21}, Zero level = -55 dB, F = 18 GHz, H= 1 µm, EMP= 30 µm (a) raw data in magnitude (b) balanced and denoised data in magnitude (c) raw data for phase shift (d) balanced and denoised data for phase shift.

The raw data in terms of magnitude and phase shift of the transmission coefficient are shown in Figure II-15.a and Figure II-15.c while the treated data are given in Figure II-15.b and Figure II-15.d. One can see that we are able to detect the gold lines whose width spans from 100 to 30 µm. In this test, the phase shift is firstly registered and the variation tendency can be seen much clearer compared to the obtained magnitude.

Based on the obtained results, one can note two points as a summary of the iNFMM lateral resolution study. First of all, the lateral resolution is approximatively equal to the tip apex size of the EMP when the other parameters are optimized. Secondly, the noise and other influences (such as sample tilt problem) can hide the useful signal and decrease the lateral resolution. With the proposed signal treatment techniques, these influences can be effectively reduced.

In fact, the lateral resolution study has also been evaluated with a smaller tip apex (7 µm). However, the result is not as good as the 30 µm one since a smaller probe is very easy to contact the sample and leads to a transformation of the tip, leading to an inaccurate result.

Consequently, the tip apex size cannot be further reduced. So, based on the probe robustness consideration, the size obtained is 30 µm and consequently the lateral resolution cannot be smaller than 30 µm. The resolution is estimated as λ/555 in this case.

Since the 1D lateral resolution is evaluated, we are now interest in the 2D imaging performance of our iNFMM which is investigated in the next section.

II.3.2.2 2D imaging

After the determination of the iNFMM lateral resolution, the 2D imaging performance of our iNFMM is under investigation in this section. As previously mentioned, the lateral resolution is directly linked to the EMP apex size and we have chosen to limit it to 30 µm because of the lack of feedback system and consideration on the probe robustness. We have to say that this limitation makes some studies like the cellular imaging and DNA studies of biological materials very difficult to realize [KIM 05], [TAB 99], [FRI 05], [FAR 12]. However, several applications for example large surface imaging and on wafer device testing are expected when considering the sampling speed and the resolution achievable.

In this section the large surface imaging possibility is firstly under evaluation. The sample under test is an euro cent (diameter of 16.25 mm). To cover all the coin surface, the scanning surface is selected as 17.05*17.05 mm^2.

Once the scanning surface is determined, one has to choose the other setting parameters. As mentioned before, the signal drift is more important with longer image acquisition time which is calculated according to the scanning step size and the sampling speed. Consequently, a compromise between the drift error and the image quality (resolution) has to be chosen. The sampling speed is fixed to 12 points per second for our iNFMM. The only factor that influences the image acquisition time is the scanning step size. Because a very large surface has to be imaged in this case, the scanning step size is selected as 50 µm to avoid too much sampling points. Thus, the EMP apex size is chosen to 70 µm which is slightly larger than the scanning step size to assure the best resolution.

According to the measurement stability study in section II.2.4.3, the image acquisition time is therefore estimated at around 3 hours and the signal drift error is about 5 %.

The measurement conditions are listed in the following table:

Zero level	Frequency	Scanning step size	Acquisition time	IFBW	Stand-off distance	Probe apex size
-55 dB	18 GHz	50 µm	2.8 hours	100 Hz	10 µm	70 µm

Table II-7: Setting parameters for the large surface imaging of a one cent euro coin.

According to the measurement conditions given above, the raw data are presented in Figure II-16.b and compared to the original image (Figure II-16.a).

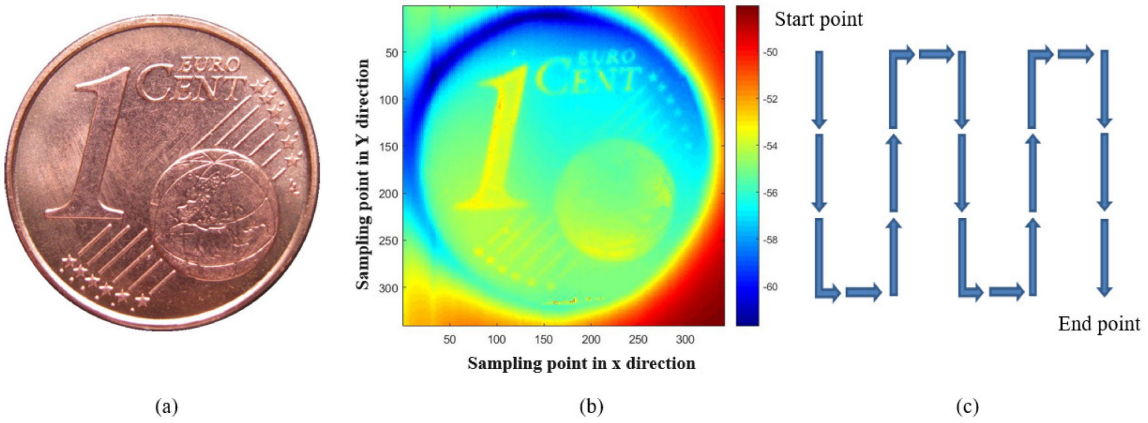

Figure II-16: The original and acquired image of an euro cent coin: (a) Original image (b) The acquired image in terms of magnitude of transmission coefficient S_{21} (c) Scanning path of the acquired image.

As indicated in Figure II-16.c, the image is acquired by scanning the sample line by line. It is very obvious that a magnitude difference between the start point and the end point, which is about 4.75 dB exists. This magnitude variation is mainly due to the signal drift and the sample tilt problem. When comparing the obtained image to the original one, it is noticed that the number '1' and the letter 'euro cent' are clearly visible. However, the stars and lines at the image lower right part are more subjected to the signal drift and the sample tilt and only the contour of the 'earth' can be observed.

To improve the image quality, an algorithm is proposed to reduce the noise and to completely balance the magnitude distribution on the entire scanned surface. This algorithm is based on the method proposed by K. J. Coakley [COA 15] that can further correct these imperfections. The solution describes an adaptive and robust implementation of local regression and local likelihood models to improve the image quality.

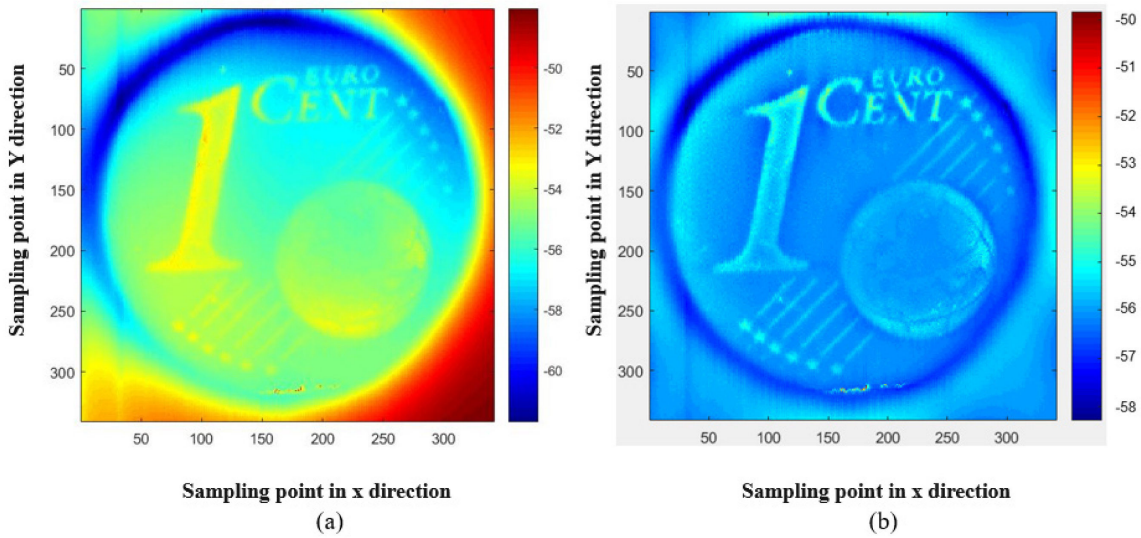

Figure II-17: The acquired image of an euro cent coin before/after treatment: (a) The raw data (b) The treated image with the proposed algorithm.

As depicted in Figure II-17.b, firstly the magnitude difference between the start point and the end point is corrected. The contrast of the number '1' and the letters 'euro cent' is also improved at the image upper left part. Moreover, the stars, lines and the 'European Union's place on the globe' can be clearly distinguished, which is considered as a large improvement compared to the raw data.

Compared to the probe apex size of 70 µm, this diameter of an euro cent coin is 230 times larger and takes about 3 hours for the imaging. Apart from the large surface imaging, our iNFMM is also able to image small object like a device on wafer. For example, in this case an accelerometer is chosen as the imaging target because of its particular shape.

The optical image of the fabricated accelerometer is presented in Figure II-18.a. The left part of the accelerometer is the fixed plates and the right part is the moveable plates.

With the same scanning path as indicated in Figure II-16.c, the raw data of the transmission coefficient S_{21} in terms of magnitude are acquired and shown in Figure II-18.b. One can note that all the plates appear in the image but the spacing between each plate is not very clear, which is mainly due to the signal drift and the sample tilt error. Moreover, the two patches at each side show a different magnitude level compared to the middle plates, which is considered incorrect since their material as well as the stand-off distance are the same.

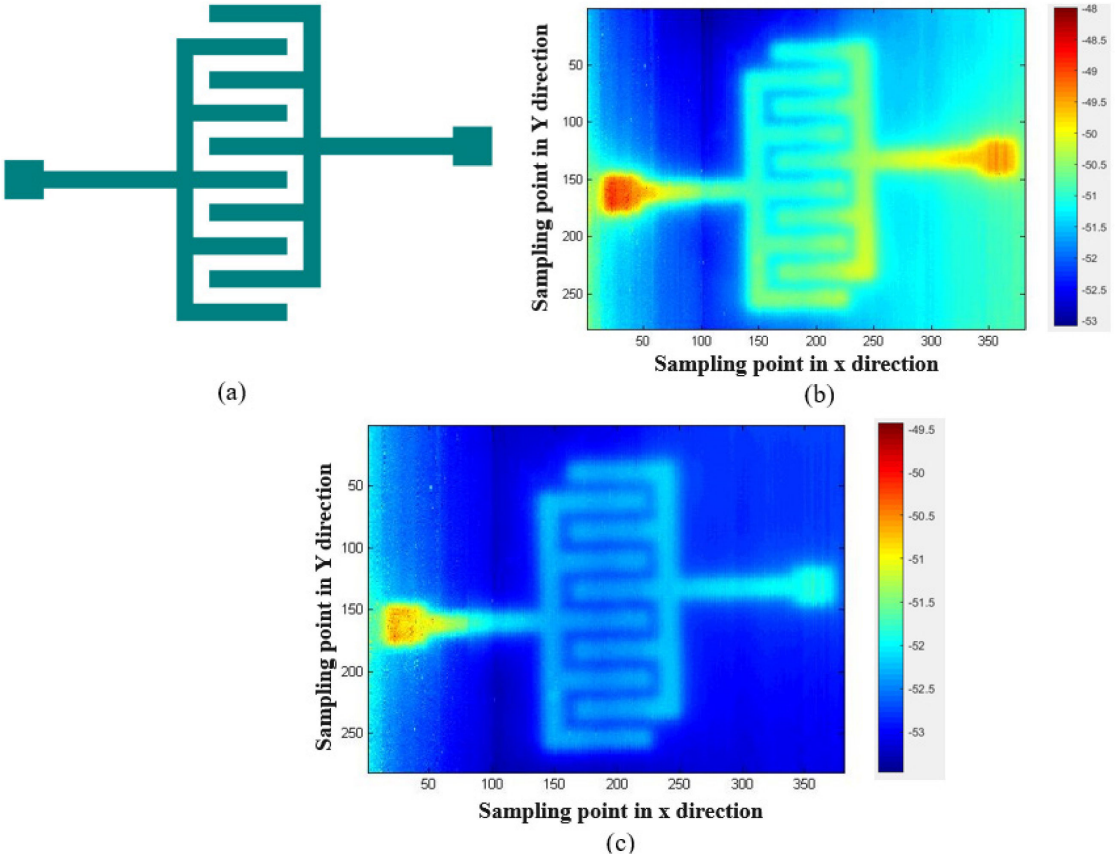

Figure II-18: The image from the fabricated accelerometer on wafer: (a) The image of the accelerometer (b) The raw image (c) The treated image with the proposed algorithm.

After applying the proposed algorithm described previously, the new image obtained is given in Figure II-18.c, where the spacing between each plate can now be clearly distinguished. Furthermore, the difference in magnitude between the patch at the extremity and the middle plates is reduced. However, this difference cannot be completely removed.

II.3.2.3 Conclusion

In this part, the surface imaging performance of our iNFMM is presented respectively for 1D and 2D scenario. The measurement precision as well as the lateral resolution is introduced in the part of this chapter dedicated to 1D study. These results can also be extended to the 2D imaging case because the 2D imaging is realized by scanning the sample line by line. In the section dedicated to 2D characterization, surface imaging applications including large surface imaging and on wafer device tests are given as examples. For the large surface imaging case, an one euro cent coin is selected whose surface is about 17.05*17.05 mm^2. This test proves the large surface mapping feasibility proposed by our iNFMM. For the on wafer device, an accelerometer is chosen for demonstration. The obtained result indicates that the structure of device can be ensured with the proposed characterization means. Furthermore, with a proper selection of setting parameters and a signal processing method to be implemented, a better image quality can be therefore obtained in terms of noise and the contour clarity. Once the surface imaging are tested, we focus on the evaluation of iNFMM subsurface performance.

II.3.3 Subsurface imaging performance

As mentioned in the introduction, the iNFMM is also able to perform subsurface characterization of samples thanks to the penetration ability brought by microwaves. Consequently, the 1D and 2D imaging performance in case of subsurface situations are evaluated in this section.

II.3.3.1 1D imaging

First of all, the 1D subsurface imaging performance is studied. The sample under test chosen is the one illustrated in Figure II-7.a, on which different thicknesses (2, 7, 12 µm) of cover layers are deposited. The cover layer is made of SPR 200 photoresist resin because of its excellent uniformity at a range of thickness from 1 to 12 µm with only a single-coat process. Similarly to the previous studies, the setting parameters should be carefully

determined. For this study, the zero level is set to -55 dB, the IFBW is 100 Hz, the power is 0 dBm and the stand-off distance is kept to 1 µm above the cover layer.

Since the thickness of the cover layer is no more than 12 µm, the tip apex size is chosen to 30 µm. Two reasons are considered for this selection. The first one is to ensure the sample can be detected in the near-field region, which means the tip-sample distance has to be smaller than the tip apex size. The second reason is considered for a better resolution. This is why a 50 µm EMP (or even larger for example 70 µm EMP) is not selected. In addition, the experimentation is carried out at 18 GHz. The scanning results of the gold lines whose widths vary from 10 µm to 90 µm are depicted in Figure II-19.

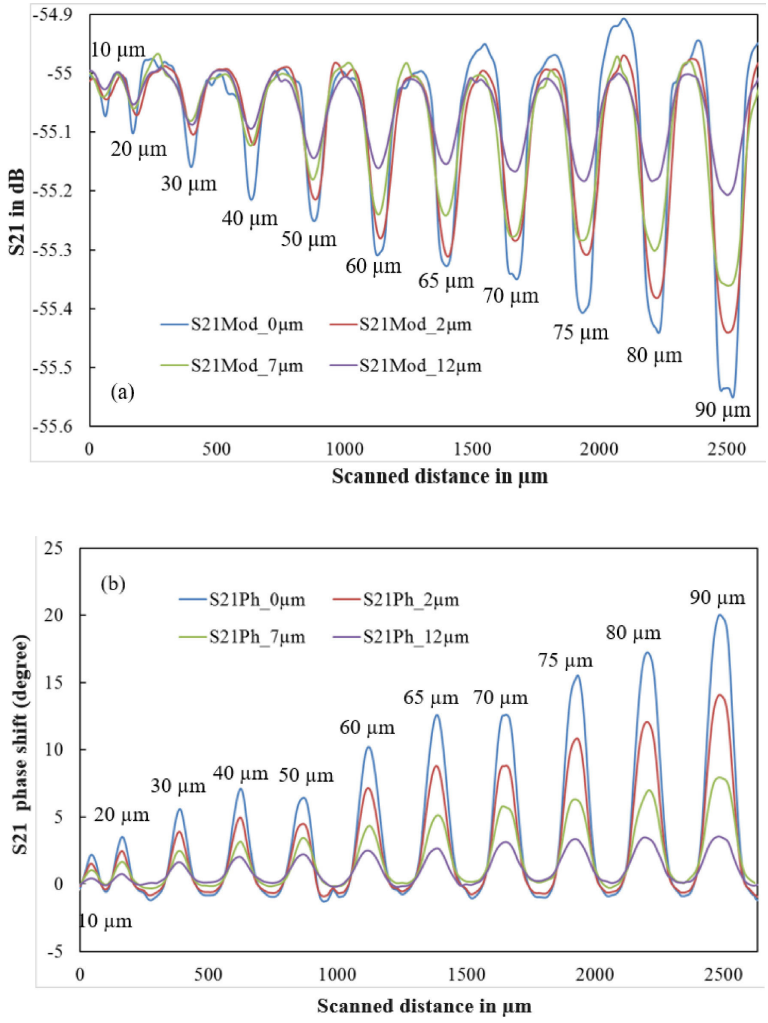

Figure II-19: Measured magnitude and phase shift of the transmission coefficient S_{21} by an EMP whose tip apex size is 30 µm in case of different thicknesses of cover layer: (a) magnitude of the transmission coefficient (b) phase shift of the transmission coefficient.

The measured transmission coefficients (S_{21}) in terms of magnitude and phase shift corresponding to the scan of different gold line widths covered by resin layers of different thicknesses is shown in Figure II-19.

As expected, the transmission coefficient sensitivity decreases with the presence of a thicker cover layer, both in magnitude and phase shift. In more details, one can note that the measured magnitude sensitivity increases from 0.05 to 0.45 dB for the gold line width going from 10 to 90 µm with a 2 µm thick cover layer. This sensitivity range changes from 0.04 to 0.33 dB when considering a thicker cover layer of 7 µm. If we continuous to increase this cover thickness to 12 µm, this value varies from 0.02 to 0.18 dB. One can also find out that the obtained phase shift varies from 0.2 to 3.2 degrees when a 12 µm thickness cover layer is deposited on the sample. This sensitivity range changes from 0.7 to 7.2 degrees once the cover layer is slightly thinner (7 µm). Without cover layer, the sensitivity range of measured phase shift turns from 2.3 to 21.3 degrees.

If we consider only the 90 µm gold line, it is more obvious to find out that the transmission coefficient sensitivity increases with the decease of the cover layer thickness, it goes from 0.18 to 0.62 dB for layers' thickness ranging from 12 to 0 µm.

As a summary of these results, the increase of cover layer thickness leads to an expected increase of the difficulty to detect the sample under test. It is demonstrated that with a 30 µm EMP, the iNFMM is still able to detect the sample which is covered by a 12 µm thick SPR 200 photoresist resin layer. Theoretically, the cover layer thickness is not only limited to 12 µm but can be extended up to the tip apex size (30 µm here). However, due to the photoresist uniformity, it is difficult to produce a thicker layer than this value with a single-coat process. So considering the measurement condition, thicker coatings could be envisaged.

II.3.3.2 2D imaging

Following the 1D imaging study, the 2D cases are carried out by considering the fabricated accelerometer on wafer (Figure II-18.a) in this section, As for the 1D subsurface

imaging case, the setting parameters remain fixed and two cover layers with the thickness of 2 µm and 12 µm are deposited on sample. The obtained images are treated with the implementation of local regression and local likelihood models algorithm. The results are shown in the Figure II-20.

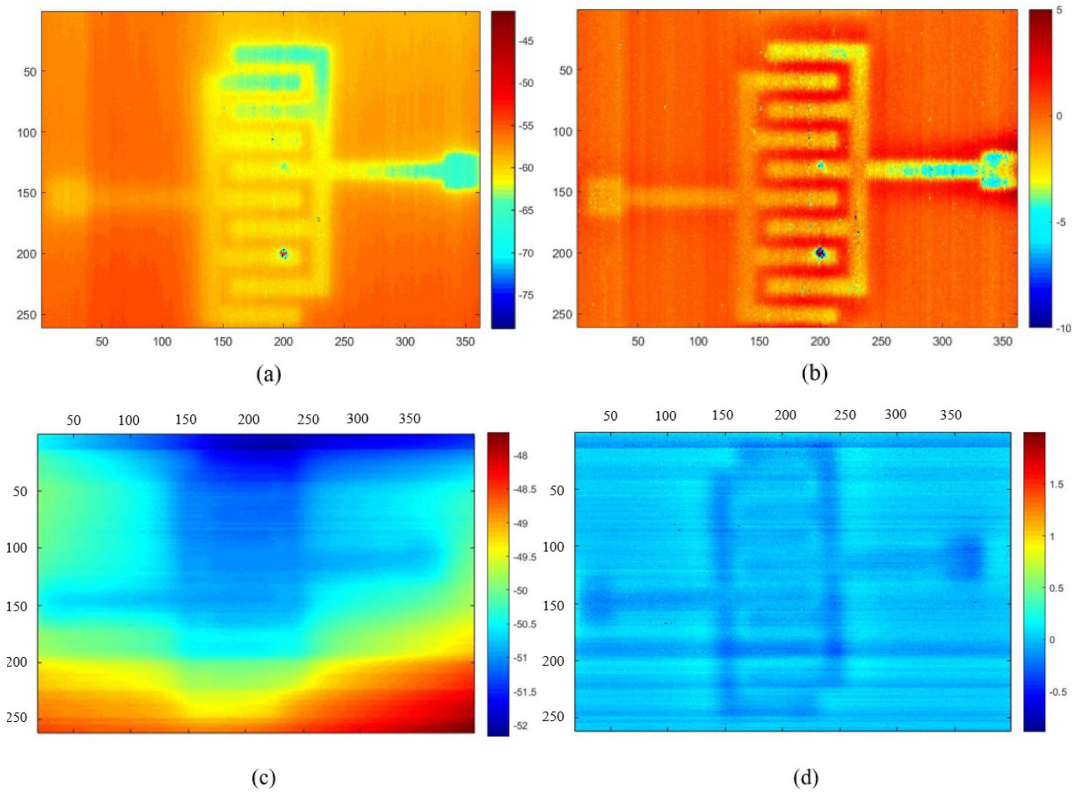

Figure II-20: The acquired image from the fabricated accelerometer on wafer: (a) The raw image with the cover layer of 2 µm (b) The treated image with the cover layer of 2 µm (c) The raw image with the cover layer of 12 µm (d) The treated image with the cover layer of 12 µm.

The raw data of the scanned accelerometer under a 2 and 12 µm thick resin layer are presented respectively in Figure II-20.a and Figure II-20.c. For the Figure II-20.a, the plates appear clearly but the spacing between each plate at the top part of image is blurry. The reason is the same than for the 1D case. For the Figure II-20.c, only the misty contour of the accelerometer can be seen, which is caused of course by the existence of the 12 µm thick resin layer and the existed signal drift.

To reduce these distortions and improve the image quality, the proposed algorithm is applied on the two raw images and the treated images are finally given respectively in

Figure II-20.b and Figure II-20.d. From the Figure II-20.b, one can find out that the spacing between each plate is much clearly distinguished compared to Figure II-20.a. Furthermore, the plates and the spacing can be found in Figure II-20.d. However, the sensitivity between the plate and the spacing is still quite small (0.15 dB), which is due to the attenuation caused by the resin layer.

As a summary for this test, the quality of the obtained image becomes worse when the cover layer is thicker. However, when the proposed algorithm is applied on the raw image, better quality in terms of contour definition and background uniformity can be therefore obtained, which helps to enhance the subsurface imaging performance.

II.3.4 Conclusion

In this section the imaging performance of our iNFMM is evaluated both in surface and subsurface condition. For the surface imaging case, the measurement precision as well as the lateral resolution is studied in the 1D case. Two examples respectively for large surface imaging and on wafer device test are imaged in the 2D scenario. Both of them are well detected and the applied algorithms gives a better imaging quality. For the subsurface imaging case, different thicknesses of photoresist resin ranging from 2 to 12 μm are deposited on wafer to evaluate their influence on the imaging quality. It is noted that thicker layer is surely leading to a poor measurement sensitivity and contour clarity.

II.4 Conclusion

In this chapter, two parts are mainly introduced for the better understanding of our iNFMM. The first part starts with a brief description of the iNFMM setup, where the main components are presented. After that, since the measurement precision as well as the noise figure is related to the setting parameters, their influences are discussed. Finally, the measurement errors are carefully evaluated based on the previous research work [GU 16_d].

The second part shows the imaging performance of the proposed iNFMM system, in both surface and subsurface situation. The 1D and 2D images are illustrated by using the setting parameters previously determined. To improve the image quality, some image

treatment methods such as position/signal difference method, adaptive robust statistic method and local regression and likelihood estimation method are respectively used. With the help of these image treatment approaches, a better imaging quality is achieved.

II.5 References

(28 references, Classified in alphabetical order)

[BAK 15] Bakli, H. (2015). *Développement d'une plate-forme de microscopie champ proche hyperfréquence par interférométrie* (Doctoral dissertation, Lille 1).

[CAM 86] Campbell, I. H., & Fauchet, P. M. (1986). The effects of microcrystal size and shape on the one phonon Raman spectra of crystalline semiconductors. *Solid State Communications*, *58*(10), 739-741.

[CAS 11] Case J.T, Ghasr M.T, Zoughi R (2011), "Optimum Two-Dimensional Uniform Spatial Sampling for Microwave SAR-Based NDE Imaging Systems," *IEEE Transactions on Instrument and Measurement*. vol. 60, n°.12, pp. 3806-3815.

[CHI 12] Chisum, J. D., & Popovic, Z. (2012). Performance limitations and measurement analysis of a near-field microwave microscope for nondestructive and subsurface detection. *IEEE Transactions on Microwave Theory and Techniques*, *60*(8), 2605-2615.

[CLE 79] Cleveland, W. S. (1979). Robust locally weighted regression and smoothing scatterplots. *Journal of the American statistical association*, *74*(368), 829-836.

[COA 15] Coakley, K. J., Imtiaz, A., Wallis, T. M., Weber, J. C., Berweger, S., & Kabos, P. (2015). Adaptive and robust statistical methods for processing near-field scanning microwave microscopy images. *Ultramicroscopy*, *150*, 1-9.

[FAR 12] Farina, M., Di Donato, A., Monti, T., Pietrangelo, T., Da Ros, T., Turco, A & Morini, A. (2012). Tomographic effects of near-field microwave microscopy in the investigation of muscle cells interacting with multi-walled carbon nanotubes. *Applied physics letters*, *101*(20), 203101.

[FRI 05] Friedman, B., Gaspar, M. A., Kalachikov, S., Lee, K., Levicky, R., Shen, G., & Yoo, H. (2005). Sensitive, label-free DNA diagnostics based on near-field microwave imaging. *Journal of the American Chemical Society*, *127*(27), 9666-9667.

[GRE 16] Gregory A. P, Blackburn J. F, Lees K, R. N. Clarke, T. E. Hodgetts, S. M. Hanham, and N. Klein (2016), "Measurement of the permittivity and loss of high-loss materials using a Near-Field Scanning Microwave Microscope," Ultramicroscopy, vol. 161, pp. 137–145.

[GU 15] Gu, S., Haddadi, K., El Fellahi, A., & Lasri, T. (2015, September). Near-field scanning microwave microscope for subsurface non-destructive characterization. In *Microwave Conference (EuMC), 2015 European microwave week* (pp. 155-158). IEEE.

[GU 16_a] Gu, S., Lin, T., & Lasri, T. (2016). Dielectric properties characterization of saline solutions by near-field microwave microscopy. *Measurement Science and Technology*, *28*(1), 014014.

[GU 16_b] Gu, S., Lin, T., & Lasri, T. (2016). Broadband dielectric characterization of aqueous saline solutions by an interferometer-based microwave microscope. *Applied Physics Letters*, *108*(24), 242903.

[GU 16_c] Gu, S. (2016). Contribution to broadband local characterization of materials by near-field microwave microscopy (Doctoral dissertation, Lille 1).

[GU 16_d] Gu, S., Haddadi, K., El Fellahi, A., & Lasri, T. (2016). Setting parameters influence on accuracy and stability of near-field scanning microwave microscopy platform. *IEEE Transactions on Instrumentation and Measurement*, *65*(4), 890-897.

[IMT 06] Imtiaz, A., & Anlage, S. M. (2006). Effect of tip geometry on contrast and spatial resolution of the near-field microwave microscope. *Journal of applied physics*, *100*(4), 044304.

[KAN 03] Kantor, R., & Shvets, I. V. (2003). Method of increasing spatial resolution of the scanning near-field microwave microscopy. *Journal of applied physics*, *93*(9), 4979-4985.

[KAR 06] Karbassi, A., Paulson, C. A., Kozyrev, A. B., Banerjee, M., Wang, Y., & van der Weide, D. W. (2006). Quadraxial probe for high resolution near-field scanning rf/microwave microscopy. *Applied physics letters*, *89*(15), 153113.

[KIM 03] Kim, J., Kim, M., Kim, H., Song, D., Lee, K., & Friedman, B. (2003). Improving images from a near-field scanning microwave microscope using a hybrid probe. *Applied physics letters*, *83*(5), 1026-1028.

[KIM 05] Kim, S., Yoo, H., Lee, K., Friedman, B., Gaspar, M. A., & Levicky, R. (2005). Distance control for a near-field scanning microwave microscope in liquid using a quartz tuning fork. *Applied physics letters*, *86*(15), 153506.

[KLE 06] Kleismit R. A, Kazimierczuk M. K. and Kozlowski G. (2006). "Sensitivity and resolution of evanescent microwave microscope." *IEEE Transactions on Microwave Theory and Techniques*. 54, nº. 2, pp. 639-647.

[OLA 14] Oladipo, A. O., Lucibello, A., Kasper, M., Lavdas, S., Sardi, G. M., Proietti, E & Panoiu, N. C. (2014). Analysis of a transmission mode scanning microwave microscope for subsurface imaging at the nanoscale. *Applied Physics Letters*, *105*(13), 133112.

[REN 11] Ren, Z., Boybay, M. S., & Ramahi, O. M. (2011). Near-field probes for subsurface detection using split-ring resonators. *IEEE Transactions on Microwave Theory and Techniques*, *59*(2), 488-495.

[SAR 15] Sardi, G. M., Lucibello, A., Kasper, M., Gramse, G., Proietti, E., Kienberger, F., & Marcelli, R. (2015). Optimization of the imaging response of scanning microwave microscopy measurements. *Applied Physics Letters*, *107*(3), 033107.

[SUN 14] Sun, W., Yang, Y., Wu, Z., Feng, T., Zhuang, Q., Peng, L. M & Ong, C. K. (2014). Penetrative imaging of sub-surface microstructures with a near-field microwave microscope. *Journal of Applied Physics*, *116*(4), 044904.

[TAB 99] Tabib-Azar, M., & Katz, J. L. (1999). Evanescent microwaves: A novel super-resolution noncontact nondestructive imaging technique for biological

applications. *IEEE Transactions on Instrumentation and Measurement*, *48*(6), 1111-1116.

[TAB 00] Tabib-Azar M and S. R. Leclair (2000), "Applications of evanescent microwave probes in gas and chemical sensors," Sensors Actuators, B Chem., vol. 67, nº. 1, pp. 112–121.

[TIB 89] Tibshirani R.J, Local Likelihood Estimation (Ph.D. thesis 1989), Department of Statistics, Stanford University.

[WEB 12] Weber J. C, Schlager J. B, Sanford N. A, A. Imtiaz, T. M. Wallis, L. M. Mansfield, K. J. Coakley, K. A. Bertness, P. Kabos, and V. M. Bright (2012), "A near-field scanning microwave microscope for characterization of inhomogeneous photovoltaics," *review of scientific instruments*, vol. 83, nº. 8.

Chapter III

Dielectric characterization of glucose aqueous solutions with iNFMM

Chapter III : Dielectric characterization of glucose aqueous solutions with iNFMM

III.1 Introduction

In recent years, the knowledge of the dielectric properties of biological aqueous solutions has attracted increasing attention due to its importance in a spread range of applications in different fields such as biomedical research [ZHA 14], clinical monitoring [KAR 13] and food processing [LAM 06]. Among the solutions of interest, glucose aqueous solution is considered as one of the most important since it plays a fundamental role in a wide range of biological processes [GYO 98]. For instance, the diabetes is due to the uncontrolled increase of the glucose concentration in blood, which is either caused by the inability of pancreas to produce the insulin (Type 1 diabetes) or the body is still able to produce insulin but becomes resistant (Type 2 diabetes). Based on the research data provided by International Diabetes Federation (IDF) Diabetes Atlas, to date 415 million adults are confirmed to have diabetes and this number will rise to 642 million by 2040 [INT 15]. Furthermore, one over two adults with diabetes is undiagnosed and 5 million people died from this disease in 2015 [INT 15]. As one of the largest health emergencies, the only method to improve the diagnosis and management of diabetes mellitus is to continuously monitor the glucose level in blood. The world health organization gives a criteria for this diagnosis. The glucose concentration should be no more than 126 mg/dl (1.26 mg/ml) during fasting and this level should not exceed 200 mg/dl (2 mg/ml) two hours after eating [INT 15]. Thus, diagnosis methods which are fast, costless and of high precision to characterize the glucose concentration in blood are necessary.

In the following sections, different characterization methods to distinguish the glucose concentration are briefly introduced in the section III.2. In section III.3, the high measurement precision of the interferometer-based matching network is under investigation. The error rate due to different modes of characterization is discussed in section III.4. A well-established first order Debye model to determine the complex

permittivity of different concentrations of glucose aqueous solutions is illustrated in section III.5.

Afterwards, we present the investigation of glucose aqueous solutions with the NFMM system based on two modes: immersion mode and non-contact mode. It has to be mentioned that in a previous study NaCl aqueous solutions have been successfully investigated in immersion mode by the interferometer based NFMM proposed [GU 16_a], [GU 17]. However, in the frequency range of interest (2 GHz to 18 GHz), NaCl solutions show larger variation on the complex permittivity than glucose solutions for the same level of concentration. This phenomenon is due to the fact that NaCl is an ionic compound while glucose performs strong hydration capability in bulk water [SHI 15]. Hence, the distinction between glucose aqueous solutions based on the variation of permittivity come up much more challenging.

In section III.6, the characterization of the glucose concentration in immersion mode is demonstrated. In our study, glucose concentrations from 0 to 10 mg/ml (physiological range) with a step of 1 mg/ml are firstly investigated to prove the measurement feasibility. After that, the non-contact mode is discussed and compared with the immersion mode in section III.7. With a careful control of the measurement procedures, the glucose concentration ranging from 0 to 3 mg/ml with a step of 0.6mg/ml is prepared for the non-contact mode. This small resolution is to meet the typical day-variation level ranging from 50 to 250 mg/dl [INT 15]. Finally in section III.8, the conclusions related to these two measurement modes are given.

III.2 Different characterization methods

III.2.1 Introduction

Different characterization methods to figure out the glucose concentration in blood have been proposed [YAN 11], [VAS 12], [HAY 03]. One of the most promising methods to evaluate solutions concentration in biological samples is the enzyme oxidation technique [He 01]. Nevertheless, despite its high accuracy, it has shown some limitations like

instability and invasive character [YAN 11]. Studies have also shown the variation of glucose concentration changes the complex permittivity of the solution which directly influences its impedance [TUR 07]. Therefore, the glucose concentration can be identified by estimating the corresponding complex permittivity. Among the different instruments candidate for this kind of characterizations, one can find tools based on microwave techniques. Owing to the advantages provided by microwaves, including features such as non-invasive character and label-free approach, the differentiation of the glucose concentration as well as the establishment of dielectric spectra of glucose aqueous solutions attract a great attention [VAS 12], [LEE 12]. Nevertheless, to be accepted as a reference technique, the characterization method has to be able to distinguish solutions of small concentration and answer to requirements such as rapidity, simplicity of operations, high selectivity and sensitivity, which are still an open challenge.

III.2.2 Characterization by microwave techniques

III.2.2.1 Open-ended coaxial probe method

In fact, numerous studies in the microwave range have been dedicated to several sensing techniques and modalities to distinguish glucose aqueous solutions in different concentrations. The first approach is the well-known open-ended coaxial probe method [SEN 16] [NOT 06]. An illustration is given in Figure III-1.

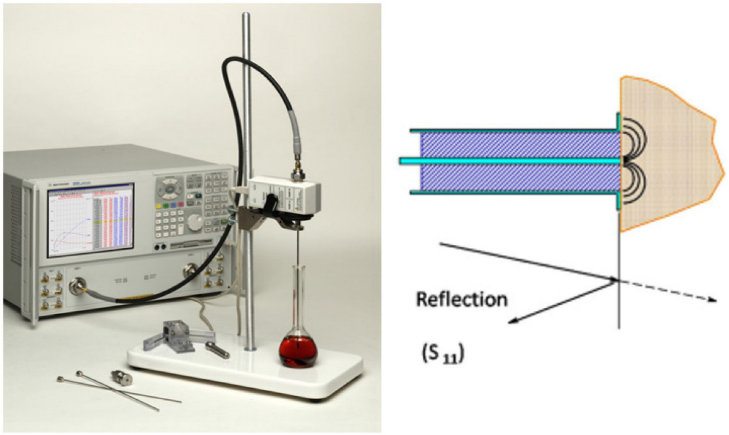

Figure III-1: Keysight 85070e open-ended coaxial probe [NOT 06].

The principle of this technique is to measure the magnitude and phase of the signal reflected at the open-ended coaxial probe which is immersed into the sample under test. The probe size is typically 3.5 mm, which means that it needs a large volume of sample for the test. Except this drawback, the advantages are clear. Indeed, it is already successfully commercialized, the calibration method as well as the supporting software make it simple to use. This broadband technique can work from several Hz to tens of GHz. According to the measurement results presented in [SEN 16], the precision is 1 mg/ml for the D-glucose in Ringer Lactate solution.

III.2.2.2 Resonator technique

The second method is based on the resonator technique which is mainly presented as a microstrip ring [SCH 13], a lambda/2 resonator [SCH 14] and a whispering gallery [GUB 15]. These structures are presented in Figure III-2.

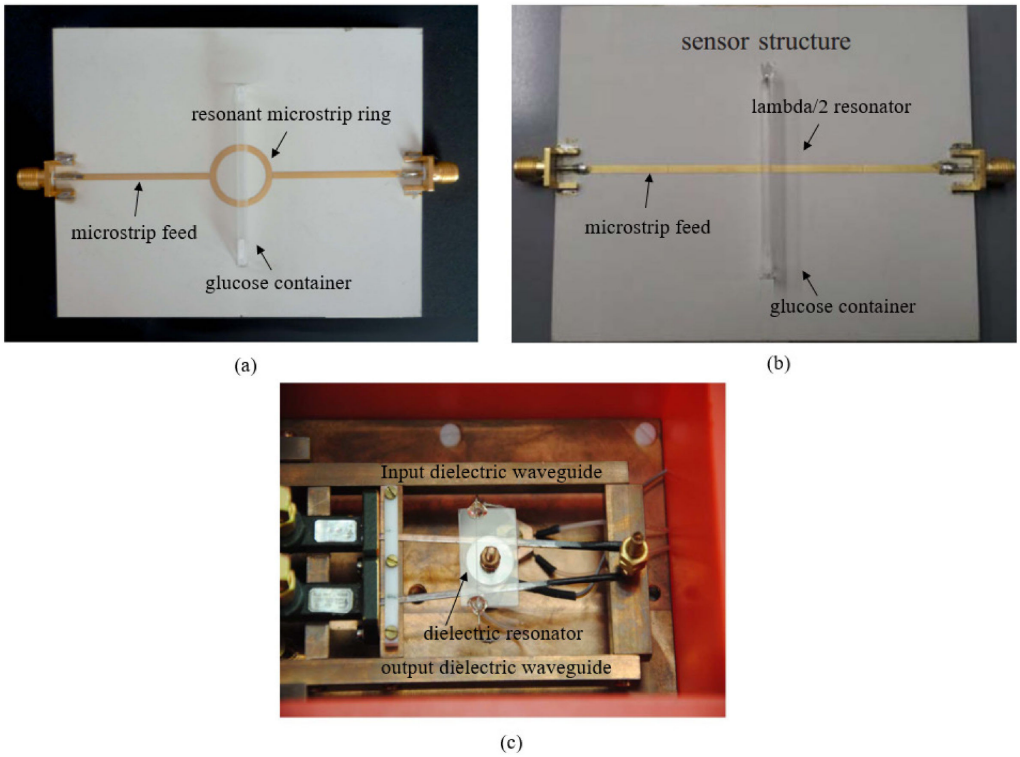

Figure III-2: (a) Microstrip ring resonator [SCH 13] (b) Lambda/2 resonator [SCH 14] (c) Whispering gallery mode resonator [GUB 15].

The principle of this method is to detect the frequency shift from the reference resonant frequency, due to the concentration level variation. By this characterization means a glucose concentration variation of about 0.5 mg/ml can be distinguished [SCH 13], [SCH 14]. Nevertheless, the resonator-based structure presents some restrictions in terms of frequency bandwidth, which means the working frequency of a resonator-based sensor can only function around its resonance frequency. Furthermore, the measurement sensitivity is strongly dependent on the resonator quality factor but this latter falls rapidly when high-loss materials are involved in the tests.

III.2.2.3 MEMS sensors

Recently, new characterization means have emerged. Actually, taking benefits from the modern micro-electromechanical system (MEMS) fabrication technique, several mediator-free sensors have been realized on chip as shown in Figure III-3 [DHK 15].

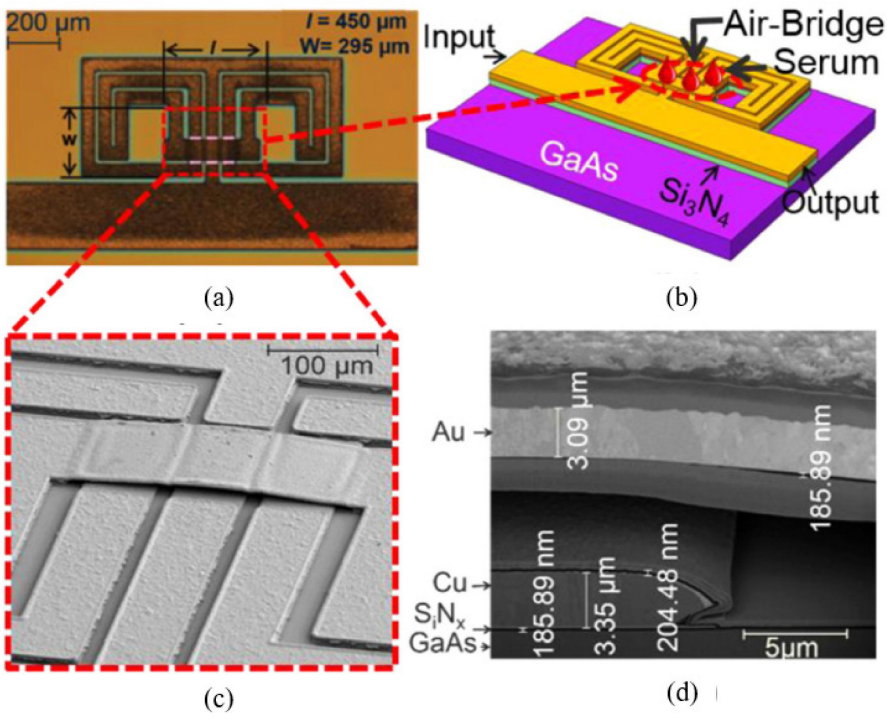

Figure III-3: (a) Schematic diagram of the fabricated glucose sensor. (b) 3-D view of the glucose sensor. (c) Scanning electron microscope (SEM) picture of the capacitive air-bridge structure by IPD technology. (d) Forced ion beam (FIB) picture of the cross-sectional view of the fabricated glucose sensor [DHK 15].

This method which requires a small volume of sample offers a better sensitivity (around 0.2 mg/ml) compared to the previous technique. However, this kind of sensors based on relatively complicated structures such as air-bridge capacitors and microfluidic channels are still quite challenging for fabrication and measurement.

III.2.2.4 Finger sensing structure

It is worth noting that considerable efforts have been made in non-invasive measurement of glucose in blood which relies on the interaction between the finger and the sensing structure [BAG 15].

Figure III-4: (a) Fabricated prototypes with two different dimensions (b) Scattering parameters measurements of the filter with the VNA (c) Placement of the thumb on the filter [BAG 15].

As illustrated in Figure III-4, this non-invasive sensor is actually a microstrip band pass filter. By placing the thumb on the sensor, the glucose concentration can be monitored continuously. This approach is expected simple, painless and cost effective for the diabetes patients. Nevertheless, studies have shown that the finger positioning as well as the pressure level on the sensing structure influence the results, which turns to be inaccurate [TUR 16], [TUR 17].

III.2.2.5 NFMM system

Since very recently, near field microwave microscopy is regarded as a promising method to address some of the limitations of the sensing techniques mentioned above [LEE

08], [BAB 06], [GU 16_a] and [GU 16_b]. This kind of technique takes advantage of the high sensitivity and label-free capability. However, according to the matching networks, the working frequency band is not the same. Matching networks based on the resonator technique can only operate at a fixed frequency (Figure III-5 [LEE 08]). To achieve a broadband matching performance, one can apply the interferometer-based matching network which has been demonstrated in a large frequency band (2-18 GHz) [GU 14], [GU 16_c]. This method provides a high sensitivity at any frequency in the frequency band covered by the interferometer.

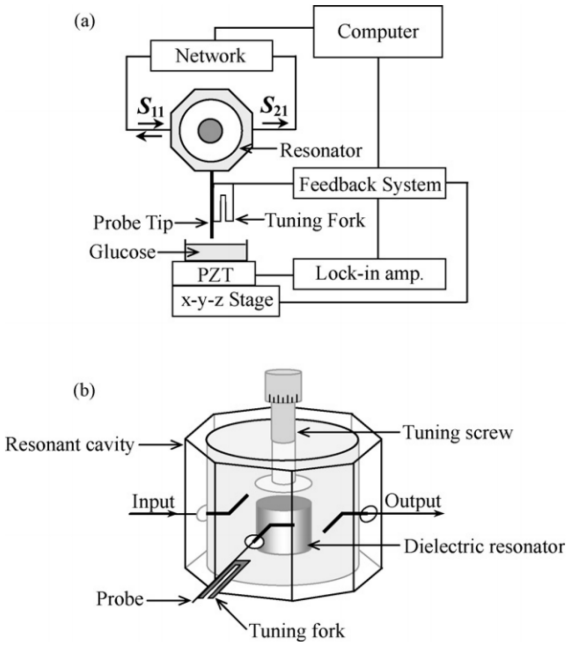

Figure III-5: (a) Block diagram of NFMM with tuning fork distance control. (b) NFMM microwave resonator and probe tip assembly [LEE 08].

Additionally, the volume needed for the tests is relatively small thanks to the evanescent microwave probe (EMP) employed whose size is in the order of several microns. Finally, overall the measurement process is rather simple and fast.

III.2.3 Conclusion

In this part, different characterization methods based on microwave techniques to measure the glucose concentration have been illustrated. These methods are considered to

be sensitive enough to distinguish small glucose concentration (1 mg/ml or even less). However, among these existing characterization means, only NFMM technique manifests advantages such as broad operating frequency band, high sensitivity, measurement simplicity and small volume of sample needed.

III.3 Interferometer based matching network evaluation

Compared to the other measurement methods, our NFMM system takes the advantage of the high precision and broad frequency band brought by the interferometer-based matching network [GU 16_a]. In this part, the high precision of this technique is demonstrated. Firstly, to appreciate the benefit of the system proposed, simulations are conducted without the presence of the interferometer-based matching network. A schematic of the systems with or without the interferometer-based matching network is given in Figure III-6.

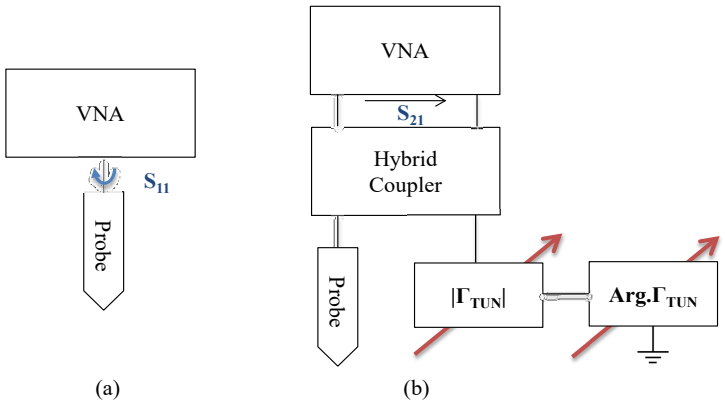

Figure III-6: Schematic of NFMM, (a): without interferometer, (b): with interferometer.

We present thereafter the influence of the relative distance between the probe and the solution on the reflection coefficient S_{11} for four glucose concentrations (DI water, 1mg/ml, 5mg/ml and 10 mg/ml) in case of the system without interferometer. The simulation results are illustrated in Figure III-7.

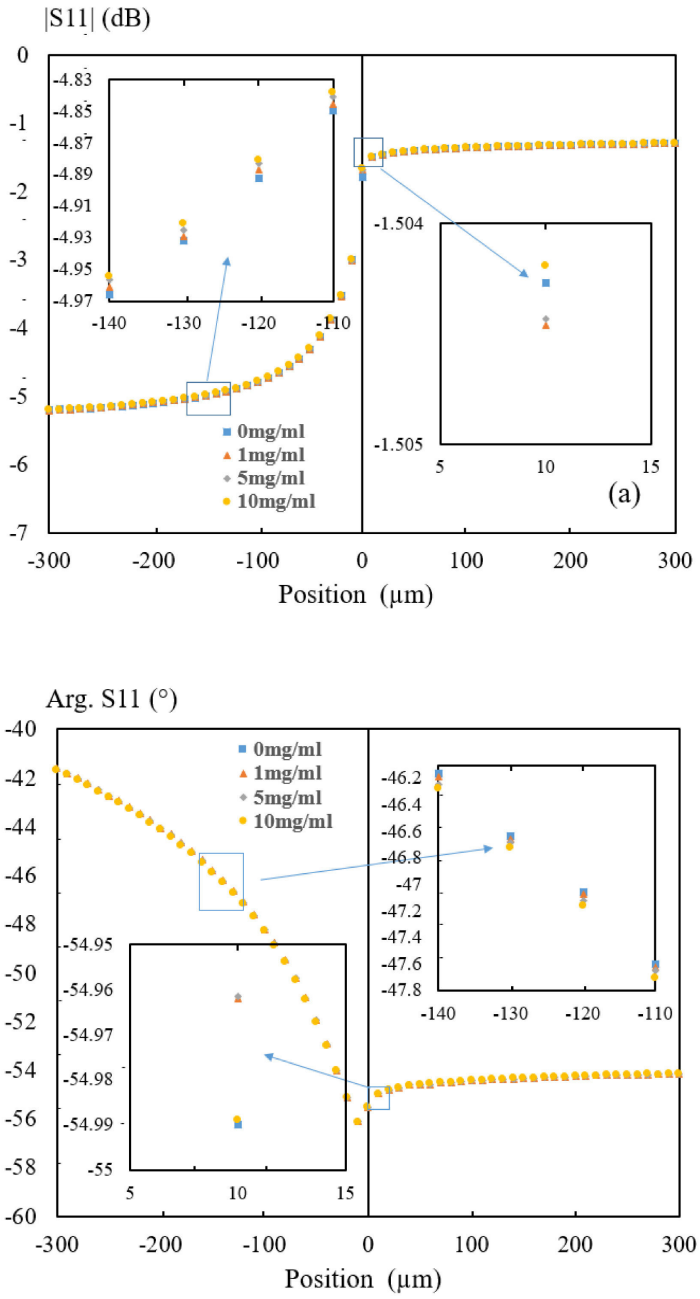

Figure III-7: HFSS™ Simulation results of the reflection coefficient versus the EMP position to the solution without the presence of interferometer-based matching network (frequency fixed at 2 GHz, concentration from 0 to 10 mg/ml): (a) Reflection coefficient magnitude (b) Reflection coefficient phase shift.

Note that the relative distance is referenced to a zero point, which is defined as the position when the EMP comes in contact with the solution. Positions larger than 0 indicate the EMP is pulled out of the solution which is related to the non-contact mode while the

negative values denote situations when the probe is in the glucose aqueous solution which is referenced to the immersion mode.

For the immersion mode characterization, the figure exhibits that for a decrease of the depth from 0 to -300 µm, the simulated reflection coefficient varies from around -3 dB to almost -5 dB. Closed up figures are provided to appreciate the gap in the reflection coefficient as a function of the solution concentration. As a conclusion of these tests, one can find that the variations in the solution are practically indistinguishable (e.g. 0.01 dB in magnitude / 0.08 degree in phase at an immersion depth of 130 µm in the concentration range going from 0 (DI water) to 10 mg/ml).

For the non-contact mode characterization, the Figure III-7 demonstrates that the simulated reflection coefficient varies from around -1.7 dB to almost -1.2 dB when the probe leaves the solution to reach a distance of 300 µm. In fact, one can note that the variation of the reflection coefficient is more pronounced between 0 to 10 µm, after that, a saturation is observed. This phenomena corresponds to the fact that the electric field is mostly confined around the probe tip [GU 16_a]. A larger electric field intensity can be detected at solution-air interface when the EMP is positioned closer to the solution. Based on the close-up figures, when the probe is at a distance of 10 µm or more, the variations of the reflection coefficient are totally indistinguishable. In addition, a frank break in the evolution of the reflection coefficient is noticed when the probe goes through the solution-air interface (1 dB difference) during the pulling of the EMP out of the liquid.

As demonstrated in this part, a characterization by means of a system that does not include an interferometer-based matching network (IBMN) is not sensitive enough to well distinguish the solution under test. In the following section, the improvement brought by the IBMN is illustrated (Figure III-6.b). To this end, we give an example of the sensitivity improvement when using the IBMN in immersion mode. The evaluation of the transmission coefficients when the probe is immersed in DI water and in a glucose-water mixture with a concentration of 10 mg/ml are given in Figure III-8 for a depth ranging from -300 to 150 µm.

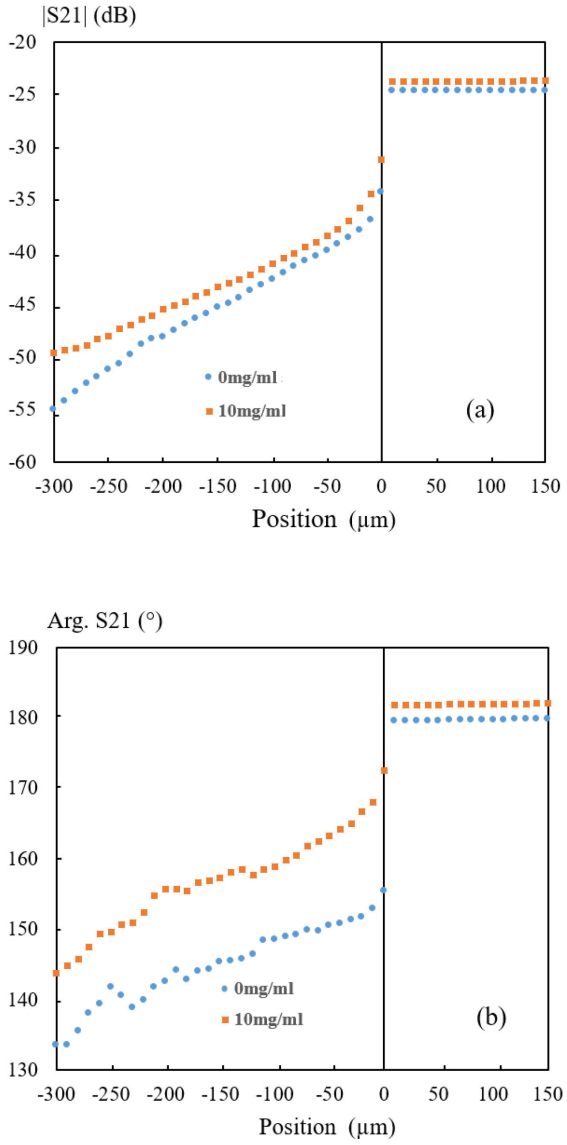

Figure III-8: Measured transmission coefficients for different immersion depths of the EMP (frequency fixed at 2 GHz, concentration (0, 10 mg/ml)): (a) Magnitude of transmission coefficient (b) Phase shift of transmission coefficient.

It has to be mentioned that the measured reflection coefficient is changed to the transmission coefficient by IBMN to avoid the directivity errors caused by the VNA when the small signals are under investigation.

In Figure III-8, as it has been already observed in the simulation study, an abrupt change in both magnitude and phase shift of the transmission coefficient, is recorded at the solution-air interface (zero point). One can figure out directly the improvement of

sensitivity from the difference of transmission coefficient thanks to the IBMN. Compared to the Figure III-7, for example at the depth of 300 µm, one can note that the transmission coefficient magnitude variation between water and glucose aqueous solution (10 mg/ml) is increased from 0.007 dB to 5.9 dB while the phase difference is enhanced from 0.35° to 10.2°. Finally, as evidenced by the measurement results, the transmission coefficient as well as the sensitivity are strongly dependent on the immersion depth, which reveals that a fine control of the position in the liquid should be assured in particular when investigating low concentration solutions.

III.4 Measurement repeatability

In the second chapter of the manuscript, the impact of the setting parameters on the measurement repeatability is provided (deviation of the repeated measurements from the mean value). Based on that study, the measurement repeatability of glucose concentration differentiation is discussed in this section.

For the immersion mode characterization, the setting parameters are an IFBW of 100 Hz, a power of 0 dBm, a number of frequency points of 201 and a zero level of -55 dB at 300 µm depth in the solution. For the non-contact mode, the power and number of frequency points remain the same, nevertheless, the IFBW is increased to 500 Hz and the zero level is set to -55 dB at a height of around 5 µm above the solution. The reasons for choosing these setting parameters are given in the following paragraphs. We list in table III-1 these setting parameters.

Modes	Power (dBm)	IFBW (Hz)	Number of frequency points	Zero level
Immersion	0	100	201	-55 dB at 300 µm depth
Non-contact	0	500	201	-55 dB at about 5 µm height

Table III-1: Setting parameters for two measurement modes in terms of Power, IFBW, number of frequency points and zero level.

In this table, the power is the one emitted by the VNA. The IFBW is the intermediate frequency bandwidth. For a conventional VNA, the receiver mix the detected microwave signal to a lower intermediate frequency (IF) by means of a local oscillator (LO). The obtained IF signal is bandpass filtered that narrows the receiver bandwidth and greatly improves the sensitivity, dynamic range and precision. The number of frequency points represents the frequency points to form the measured transmission coefficient in a frequency band. When this number increases, the curve becomes more accurate. The zero level indicates a very low level of the transmission coefficient S_{21} in order to match the high EMP impedance to the VNA impedance.

First of all, the different positions to set the zero level are achieved according to the different modes. As discussed in the chapter II, the zero level is related to the matching between the EMP and VNA. A level of -55 dB indicates a very good matching. Thus, a small variation of the transmission coefficient can be easily detected. The lower is this level, higher is the sensitivity. However, the signal will turn to be unstable during the measurement. According to the table II-4, a compromise between the sensitivity and the standard deviation of the transmission coefficient S_{21} as a function of the zero level has to be chosen. In these two measurement modes, we set the zero level to -55 dB for a high sensitivity and a relatively low deviation.

Secondly, the reason for choosing two different values of IFBW is based on considerations including standard deviation (drift errors) and evaporation effect.

For the standard deviation, it evolves with the acquisition time. As concluded in table II-1, for a fixed number of frequency points and acquisition time, a higher IFBW leads to higher drift errors. The standard deviation for an IFBW of 100 Hz and 500 Hz is about 0.8% and 0.9 %, respectively. This value increases to 1.5% for an IFBW of 1000 Hz, which is multiplied by a factor of almost 2. Taking into account the drift errors, the IFBW should be chosen no more than 500 Hz.

The second consideration to take for the IFBW selection is related to the evaporation effect of the liquid sample. For the immersion mode, the probe is plunged into the solution

at a depth of 300 μm to ensure a maximal interaction between the probe and the solution under test. This depth is selected to limit the evaporation effect during the measurement. However, this effect is very important for the non-contact mode. The measured evaporation rate is about 0.5 μm/s in Z direction. Strictly speaking, this value is mainly dependent on the temperature, atmospheric pressure, humidity and the liquid density. Because the measurement environment is fixed and the liquid density remains nearly constant for small concentrations of glucose aqueous solution, the evaporation rate is considered as stable. For the non-contact mode measurement, the probe remains fixed while the solution container is pulled up by the XYZ table in Z direction. The relative distance between the EMP and the solution container is affected by the evaporation effect and the pushing rate, it can be estimated by the following equation:

$$\text{relative distance} = (\text{pushing rate} - \text{evaporation rate}) * \text{time}$$

The pushing rate depends on the step size, number of frequency points and the acquisition time. A smaller step size, a larger number of frequency points and a longer acquisition time will lead to a decreased pushing rate. Nevertheless, to ensure the measurement precision, the step size is chosen as small as possible (1 μm) and the number of frequency points to represent the transmission coefficient is selected as 201. Thus, to increase the pushing rate, one should only adjust the acquisition time. Since this latter depends on the IFBW value, a higher IFBW leads to a faster sampling speed and a larger number of frequency points. If we fix the number of frequency points, a shorter acquisition time can be attained with a higher IFBW.

Based on the relative distance equation provided above, to ensure a positive value (the EMP moves closer towards the solution), the pushing rate should be larger than the evaporation rate (0.5 μm/s). Therefore, for a step size of 1μm, the acquisition time for each step should not exceed 2000 ms. For the non-contact mode, each measured transmission coefficient is repeated four times and the average data is achieved to reduce the measurement uncertainty. Thus, the acquisition time for each step cannot lager than 500

ms. Here we give the number of frequency points as a function of IFBW for an acquisition time of 60 seconds and 0.5 second.

IFBW (Hz)	Number of step (60s)	Number of step (0.5s)
1	60	Less than 1
10	600	5
50	3000	25
100	6000	50
500	30000	250

Table III-2: Number of frequency points as a function of IFBW; zero level = -55 dB, f = 2 GHz, acquisition time is respectively 60 second and 0.5 second.

Since the acquisition time is limited to 500 ms, the number of frequency points corresponding to different IFBWs should divide a factor of 120 which is calculated by 60s/500ms.

From the table III-1, if the number of frequency points is set to be 201, the IFBW should be chosen to 500 Hz. The standard deviation related to an IFBW of 500 Hz for a 60 seconds acquisition time is about 0.78%, which can be found in table II-2.

The measurement uncertainty can be caused not only by the setting parameters but is also due to the XYZ table mechanical errors. In our test, the XYZ table only moves in the Z direction. Based on the scanning repeatability study provided in chapter II, a standard deviation in the order of 6% for the z direction is found after 2 hours moving [GU 16_d]. As our measurement takes much less time than 2 hours (about 1 min), if this derivation is regarded as linear to time, the error rate during out measurement is about 0.05%, which can be ignored.

III.5 Complex permittivity analysis model

After evaluating the errors which occur during the measurement to assess the repeatability of the experimentation, we estimate the complex permittivity of solutions of different glucose concentrations. Complex permittivity models of the glucose-water

mixtures have been studied and discussed in different studies found in literature [TUR 15], [HOF 13] and [FUC 02]. The components of the complex permittivity, namely the dielectric constant and the dielectric losses, are dependent on the angular frequency ω and the glucose concentration C in mg/ml:

$$\varepsilon(\omega, \mathrm{C}) = \mathrm{Re}[\varepsilon(\omega, \mathrm{C})] - \mathrm{iIm}[\varepsilon(\omega, \mathrm{C})] \qquad (III-1)$$

According to the first order Debye model, the dielectric spectrum of glucose aqueous solutions can be represented by the following equation [DEB 29]:

$$\Delta\varepsilon(\omega, \mathrm{C}) = \varepsilon_{\omega\infty}(\mathrm{C}) + \frac{\varepsilon_{\omega 0}(\mathrm{C}) - \varepsilon_{\omega\infty}(\mathrm{C})}{1 + i\omega\tau_{\omega}(C)} \qquad (III-2)$$

Where $\varepsilon_{\omega 0}(\mathrm{C})$ denotes the static relative permittivity, $\varepsilon_{\omega\infty}(\mathrm{C})$ is the infinite frequency relative permittivity and $\tau_{\omega}(\mathrm{C})$ indicates the relaxation time. Several investigations, mainly conducted by using a commercial open-ended coaxial dielectric probe [ZHA 12], [RAI 98], have revealed the impact of the glucose concentration on the Debye-type parameters. Thus, relationships between the glucose concentration and the Debye-type parameters have been demonstrated by fitting the measurement data into the Debye equation [TUR 15]:

$$\varepsilon_{\omega 0}(\mathrm{C}) \approx 80.769 - 0.439.10^{-5}.\mathrm{C}$$

$$\varepsilon_{\omega\infty}(\mathrm{C}) \approx 4.076 + 5.048.10^{-7}.\mathrm{C} \qquad (III-3)$$

$$\tau_{\omega}(\mathrm{C}) \approx 8.008 + 0.275.10^{-5}.\mathrm{C} \qquad [\mathrm{ps}]$$

Based on these equations, it is observed that the static relative permittivity $\varepsilon_{\omega 0}(\mathrm{C})$ decreases with the increase of the glucose concentration while the relaxation time $\tau_{\omega}(\mathrm{C})$ shows a contrary behavior. The infinite permittivity $\varepsilon_{\omega\infty}(\mathrm{C})$ keeps the same tendency with the relaxation time $\tau_{\omega}(\mathrm{C})$. These variations are due to the fact that the structure and dynamic of water surrounding the glucose molecules are changed with the glucose concentration increase. Because the polar hydroxyl groups in glucose are supposed to replace the surrounded local tetrahedral coordination of the hydrogen bond network of water [SHI 15].

This formation of hydration shell influences the static relative permittivity and makes the water molecule difficult to rotate, which leads to an increase of relaxation time and a decrease of static relative permittivity [NAN 97].

It is worth underlining that the model is completed at a room temperature of 25 degrees, which is also the case for our measurements. Thanks to these equations, the complex permittivity of glucose aqueous solutions, considered in the physiological range (0 to 10 mg/ml), is extracted for eleven concentrations (step of 1 mg/ml). The results are presented in Figure III-9.

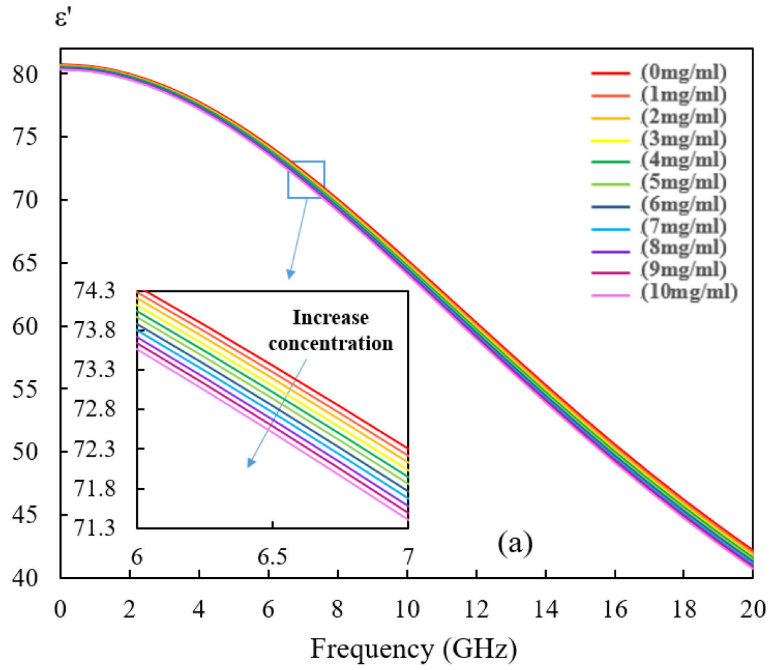

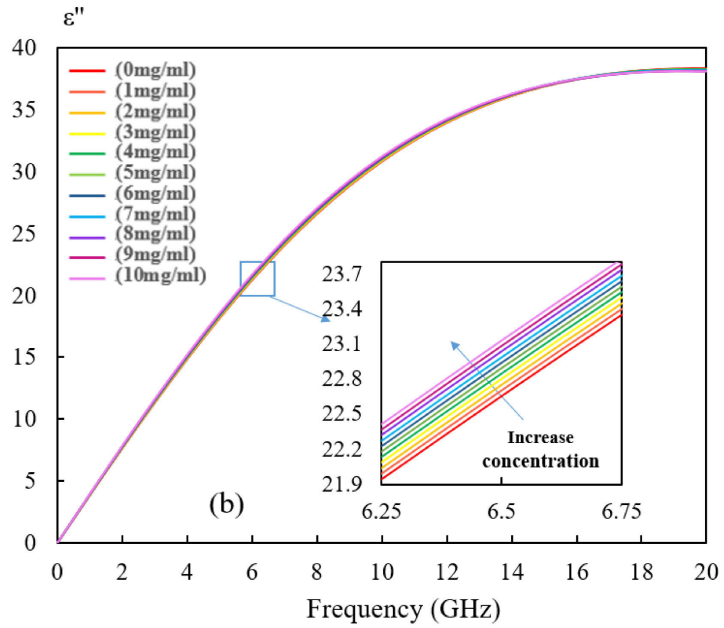

Figure III-9: The extracted complex permittivity of the glucose aqueous solution in physiological range varying from 0 to 10 mg/ml versus frequency. (a): The real part of the complex permittivity and its close up figure at 6.5 GHz. (b): The imaginary part of the complex permittivity and its close up figure at 6.5 GHz.

One can observe that, in the frequency range from 2 to 20 GHz, the real part of the complex permittivity falls with the frequency enhancement. Concerning the dielectric loss, it firstly increases and then turns to stabilize at high frequency. This stabilization at high frequency is due to the polarization of dipoles in the glucose molecules which cannot keep up pace with the increasing changing rate of applied electric field. This failure in accelerating oscillation leads to energy absorption [AHM 12]. This phenomenon is verified by the existing literatures [FUC 02], [MAS 92]. Thanks to these equations, the complex permittivity of glucose aqueous solution for a given concentration can be evaluated at any frequency in the range of interest.

III.6 Glucose concentration characterization in immersion mode

III.6.1 Introduction

In this section, the immersion mode characterization is under investigation. As can be seen from the word ‘immersion’, the EMP is plunged into the solutions to measure the

glucose concentration varying from 0 to 10 mg/ml (physiological range) with a step of 1 mg/ml. To prove the measurement feasibility, an electromagnetic simulation without the presence of IBMN is firstly carried out between the EMP and the glucose-water mixture at different frequencies from 2 to 18 GHz. Then, the experimental procedure is described in details. After that, the measurement results at several frequencies are illustrated and the measured transmission coefficients are finally translated into the complex permittivity.

III.6.2 Electromagnetic simulation of probe-solution interaction

After the determination of the parameters in the first order Debye model, the estimated complex permittivity is used to conduct electromagnetic simulations in HFSS™ environment for the analysis of the probe-solution interaction. In the simulation test presented, the tungsten EMP is fully immersed into a glucose-water mixture (10 mg/ml) at a depth of 300 µm to ensure a maximum electromagnetic interaction. The probe apex is a semi-sphere with a diameter of 260 µm.

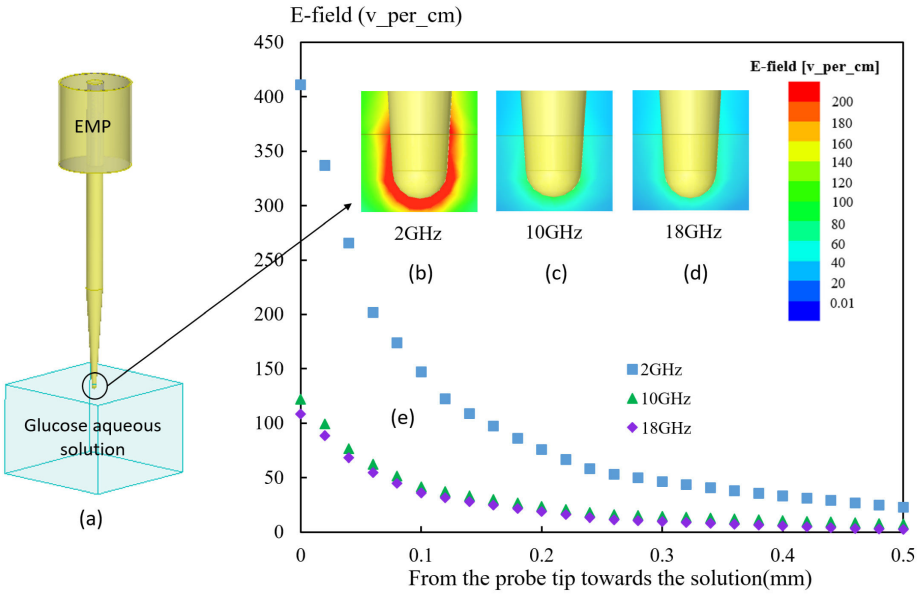

Figure III-10: Analysis of the probe-solution interaction at the cross section of the EMP (a) for a glucose concentration of 10 mg/ml at depth of 300 µm for different frequencies (2 GHz (b), 10 GHz (c) and 18 GHz (d)). E-field intensity along the extruded line at different distances from the tip (e).

As shown in Figure III-10.b, c, d, the E-field is mainly confined around the tip apex and the field intensity decays rapidly when the frequency increases. In order to analyse quantitatively this variation, a line is drawn from the tip towards the solution. The field intensity registered at different positions along this line is therefore given in Figure III-9.e. At the tip apex, a maximum field intensity around 400 V/cm is registered at 2 GHz, this value drops to 120 V/cm and 108 V/cm at 10 GHz and 18 GHz, respectively. One can note that the fall between 2 and 10 GHz is quite important (gap of 280 V/cm) whereas a slight decay between 10 GHz and 18 GHz is observed (difference of 12 V/cm). As for the stabilization of the dielectric losses at high frequency, the evolution toward a steady state is due to the rapid E-field polarization change which becomes too fast for the dipole to oscillate from a few GHz. Thus, even though the frequency continues to increase the molecules rotation speed is limited. If a fixed frequency is considered, we retrieve that the longer is the distance from the probe the smaller is the E-field intensity. For instance, at 2 GHz, the field diminishes fast from 410 V/cm to 23 V/cm if the distance between the tip apexes grows from 0 to 0.5 mm.

III.6.3 Experimental procedures and measurement results

III.6.3.1 Experimental procedures

During the measurement, the glucose aqueous solution is firstly poured into the plastic container and then placed beneath the EMP. The motor driven XYZ stage is finely controlled to adjust the position of the plastic container while the EMP remains fixed. On account of the liquid surface tension effect, the liquid-air interface performs a meniscus level which gives rise to different solution heights along the meniscus. To overcome this limitation and ensure this contact position can be repeated for each measurement, the EMP relative position as well as the volume of glucose-water mixture are fixed for each test.

For the immersion mode characterization, the EMP is slowly plunged into the solution with a step of 1 μm (by moving the container). Once the EMP reaches the solution, as predicted by the simulation, an abrupt break on the transmission coefficient appears and the ‘zero point’ (interface air-liquid) is therefore noted. Then the elevation of the plastic

container continues until the EMP arrives to a certain depth of several hundred microns (e.g. 300 µm) into the solution, so that the tip apex is fully immersed to guarantee a maximum electromagnetic interaction between the probe and the solution. At this depth, the zero level (cancelation level) is set to -55 dB to lower the measurement errors brought by the NFMM [GU 16_c]. After setting these parameters, the EMP is pulled out of the solution (by lowering the container) and immersed into it again to reach the same depth. The transmission coefficient is registered during this 'pull in' procedure [GU 16_c].

III.6.3.2 Measurement results at different frequencies

After demonstrating the sensitivity improvement at a fixed frequency (2 GHz) thanks to the presence of the interferometer-based matching network, we extend the study to the evaluation of the broadband performance of the glucose concentration differentiation by means of the proposed NFMM. Note that, except for the working frequency all other parameters of the NFMM remain unchanged during the manipulations and identical experimentation procedure are ensured.

Therefore, the EMP is immersed at 300 µm at the centre of the plastic container. For demonstration, the magnitude and phase shift of transmission coefficients obtained at 2 and 18 GHz, which are the extreme values of the working frequency band, are given in Figure III-11 for various concentrations.

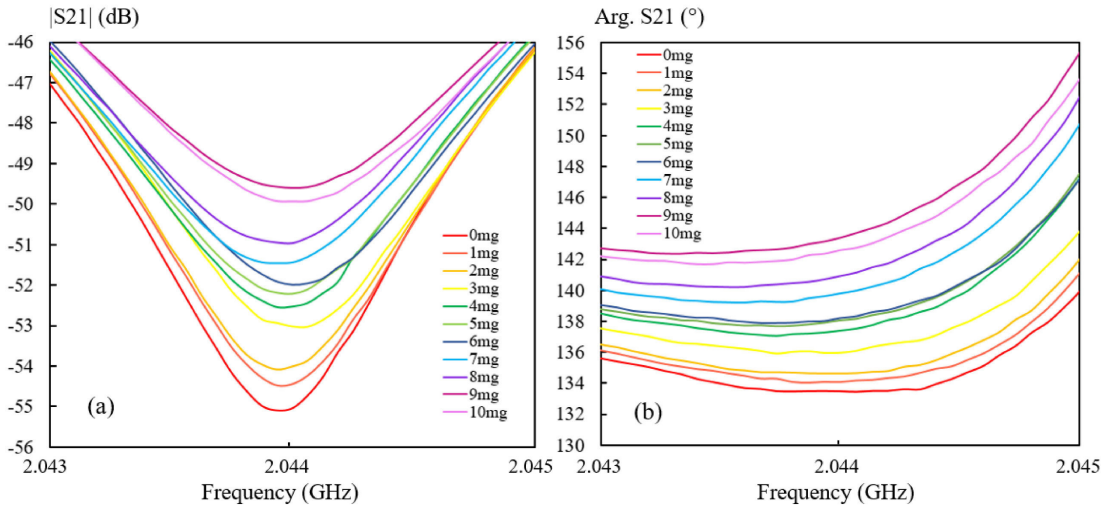

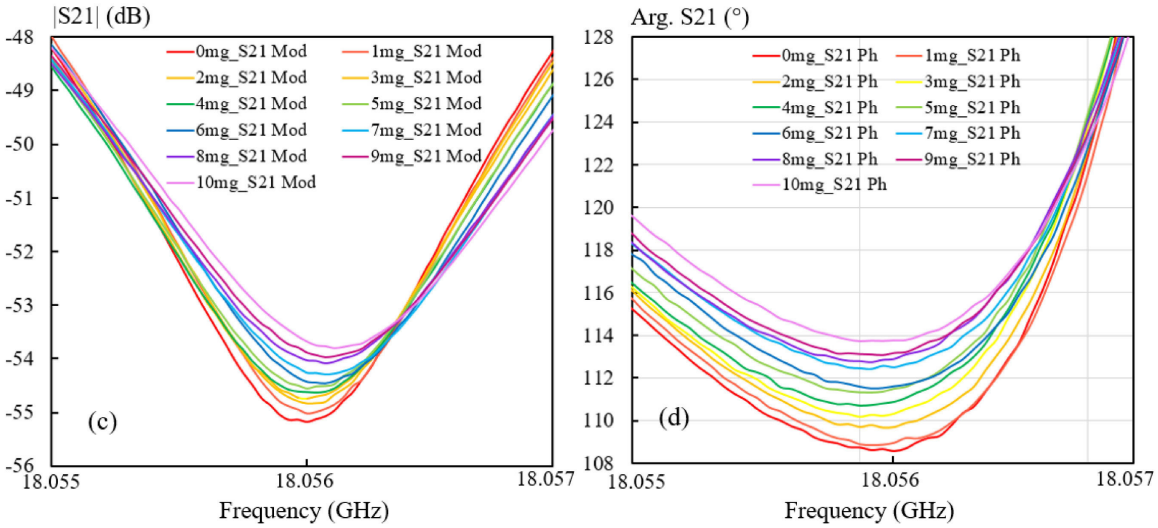

Figure III-11: Measured transmission coefficients (S_{21}) as a function of glucose concentration: (a) magnitude at 2.044 GHz (b) phase shift at 2.044 GHz (c) magnitude at 18.056 GHz (d) phase shift at 18.056 GHz.

It is clearly shown in Figure III-11 that the concentrations of glucose-water mixtures ranging from 0 to 10 mg/ml are well differentiated by means of S_{21} magnitude and phase shift at the two frequencies under evaluation. In Figure III-11.a, b, DI water gives a minimum transmission coefficient of -55.03 dB/133.46° at 2.044 GHz. With the growth of the glucose concentration, the transmission coefficient turns to be larger and the maximum value attains -49.60 dB/143.67° for the concentration of 10 mg/ml. The dynamic range of the transmission coefficient is therefore calculated as 5.43 dB and 10.22° for the magnitude and phase shift, respectively. From Figure III-11.c, d, similar tendency is observed at the higher frequency of 18.056 GHz. In that case, DI water shows a minimum transmission coefficient of -55.18 dB/108.60°. The maximum value is observed as - 53.67 dB/113.76° at a glucose concentration of 10 mg/ml. The concentrations distribution can be evidently distinguished but a lower dynamic range (1.51 dB and 5.16° respectively for the magnitude and phase shift) is observed compared to the case at 2 GHz. This observation is in accordance with the simulation results and the theoretical analysis mentioned in the previous part. To quantitatively evaluate the linearity of this distribution, the transmission coefficient corresponding to different glucose concentrations are given for these two fixed frequencies in Figure III-12.

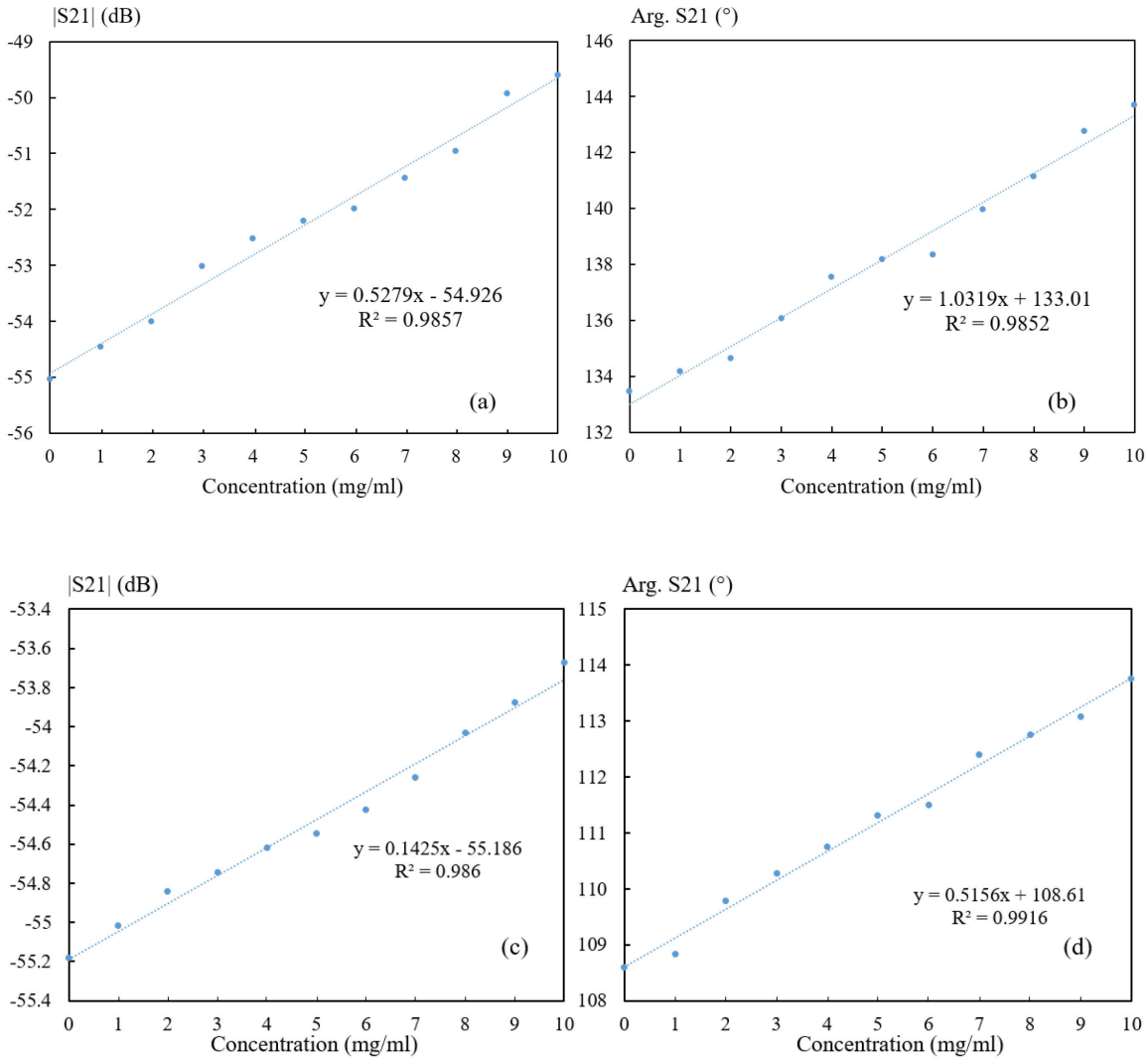

Figure III-12: Measured transmission coefficients (S_{21}) as a function of glucose concentration: (a) magnitude at 2.044 GHz (b) phase shift at 2.044 GHz (c) magnitude at 18.056 GHz (d) phase shift at 18.056 GHz. Dashed line: fitted polynomial line at first order.

According to the fitted polynomial lines at first order, the acquired values show a good linearity since the coefficient of determination R^2 is greater than 0.98 in all cases, which indicate that the distribution of the transmission coefficient is strongly correlated to glucose concentrations. Concerning the measurement dynamic range, one can observe that the variation of the transmission coefficient magnitude between water and the glucose aqueous solution of 10 mg/ml is around 5.4 dB at 2 GHz and reduces to 1.5 dB at 18 GHz. The phase shift shows the same tendency with a variation that goes from 10.2° to 5.2° for the same frequencies.

III.6.3.3 Extraction of complex permittivity

The linear correlation demonstrated in the previous section is achieved by taking care in applying the same measurement conditions including NFMM setting parameters, room temperature, immersion depth, liquid volume and probe-solution contact position. The knowledge of the transmission coefficient allows the determination of the corresponding complex permittivity by using an inverse procedure based on the one port calibration method [TUC 16]:

$$S_{21} = e_{00} + \frac{e_{10}e_{01}\Gamma_{EMP}}{1 - e_{11}\Gamma_{EMP}} \qquad (III - 4)$$

Where $\mathbf{e_{00}}$ is the directivity error, $\mathbf{e_{11}}$ denotes the port matching error and the term $\mathbf{e_{10}e_{01}}$ represents the tracking error. $\Gamma_{\mathbf{EMP}}$ is the probe reflection coefficient which can be theoretically expressed by:

$$\Gamma_{EMP} = \frac{Z_s - Z_0}{Z_s + Z_0} \qquad (III - 5)$$

Where Z_0 is the VNA characteristic impedance (50 Ω) and Z_s is the probe impedance. Since the sample is in the near field range of the probe and the apex size of the probe (D) is much smaller than the wavelength, the electromagnetic wave between the tip and sample is considered quasi-static and the probe impedance Z_s is therefore given according to the lumped element model [ANL 07]:

$$Z_s = \frac{1}{i2\pi F\varepsilon^*\varepsilon_0 D} \qquad (III - 6)$$

From the equation given above, for a given frequency F and a probe apex size D, the probe impedance as well as the probe reflection coefficient are mainly governed by the sample permittivity. The calculation of the three complex error terms (e_{00}, e_{01}, $e_{10}e_{01}$) is realized by choosing three solutions with known glucose concentrations. The probe impedances are therefore represented by Z_{s1}, Z_{s2} and Z_{s3} and result in three corresponding probe reflection coefficients Γ_{EMP1}, Γ_{EMP2} and Γ_{EMP3}. Once the errors terms

are determined, the translation from measured parameters to complex permittivity is established. However, this inverse procedure is a difficult task for broadband applications since the calibration procedure has to be repeated each time the frequency changes. In our study, the frequency range is from 2 to 18 GHz. So to keep a reasonable number of calibration procedures we consider a frequency step of 2 GHz.

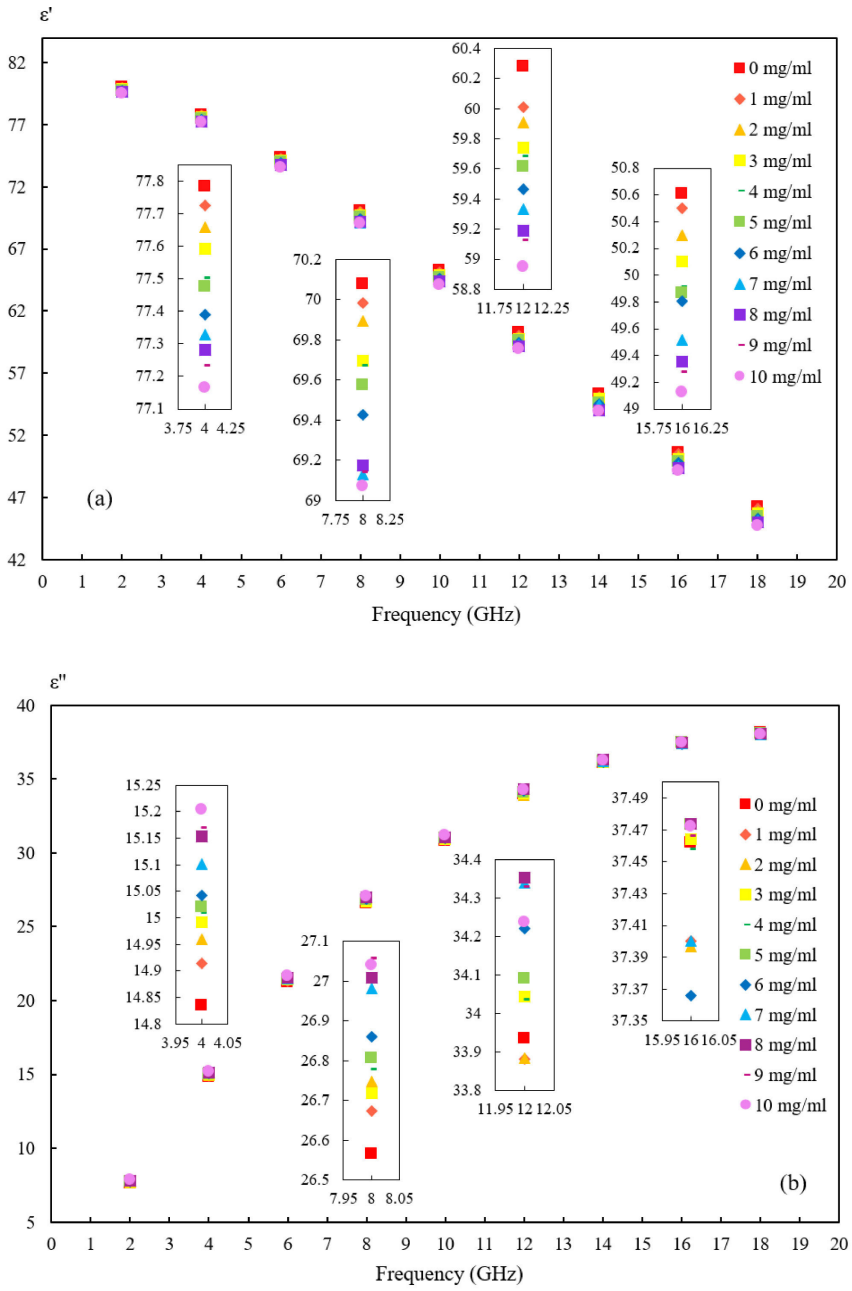

Figure III-13: The complex permittivity of glucose-water mixture versus frequency as a function of concentration and its close up figures at 4, 8, 12 and 16 GHz: (a) Real part of the complex permittivity (b) Imaginary part of the complex permittivity.

After the application of this inverse procedure, the translated complex permittivity of glucose aqueous solutions with a concentration from 0 to 10 mg/ml is plotted in the frequency range from 2 to 18 GHz in Figure III-13.

As shown in Figure III-13.a, the real part of the complex permittivity for each glucose concentration in the entire frequency band is given. According to the theoretical Debye-model provided in Figure III-9, the variation caused by a glucose concentration change (1 mg/ml) on complex permittivity is quite small. In the same figure, to better appreciate the differentiation of glucose concentrations, we give a zoom up for four discrete frequencies (4, 8, 12 and 16 GHz). For DI water, it always gives the highest dielectric constant compared to glucose-water mixtures and this value decreases when the frequency increases. For a particular frequency, it is noticed that the dielectric constant decays with the enhancement of the solution concentration level. These tendencies are consistent with the theoretical values.

In the frequency range from 2 to 10 GHz, the imaginary part of complex permittivity shows the same tendency compared to the Debye-model. DI water demonstrates minimum dielectric loss that increases in a quasi-linear manner with the concentration level elevation. Nevertheless, after 10 GHz, the differentiation of dielectric loss for each concentration is not evident as it evolves towards a saturation point. Finally, the complex permittivity measured on a large frequency band for a low concentration range of glucose aqueous solutions demonstrates a consistent behaviour when compared to the one described by the Debye-model.

III.6.4 Conclusion

In the immersion mode measurement, the complex permittivity of glucose aqueous solutions whose concentrations vary from 0 to 10 mg/ml (physiological range) is experimentally demonstrated in a frequency band spanning from 2 to 18 GHz. The interaction between the evanescent microwave probe and glucose-water mixtures is first studied by means of a finite element method solver, HFSS™ without the presence of IBMN. The results point out that the electric field is mainly confined around the probe tip and

evolves with the glucose concentration and the applied frequency. Then, the simulated reflection coefficient has been shown to be strongly influenced by both the glucose concentration and the immersion depth while a frank break is observed at the air-solution interface. The simulated results also demonstrate a very low sensitivity to glucose solutions in the concentration range of interest. To overcome such a limitation, an interferometric matching system is integrated into the NFMM for the measurement procedure. In this configuration, the reflection coefficient acquired from the EMP is mixed with a reference signal and the result of this operation is collected by a VNA in a transmission mode. An enhanced sensitivity of 0.54 dB/ 1 (mg/ml) for magnitude and 1°/ (mg/ml) for phase is obtained at 2 GHz. At 18 GHz, the minimum distinguishable variation is measured as 0.15 dB. With this same sensitivity, it is implied that our approach can arrive to a detectable resolution up to 0.3 mg/ml (1 mg/ml/ (0.54 dB/0.15 dB)) at 2 GHz. Based on the one port calibration method, the measured transmission coefficients are translated into complex permittivity. Compared to the conventional resonator method, the proposed technique enables a broadband characterization of high loss materials with a quite high sensitivity. In the next section, the glucose concentration characterization in non-contact mode is demonstrated to compare with the immersion mode.

III.7 Glucose concentration characterization in non-contact mode

III.7.1 Introduction

After the characterization of glucose solution in immersion mode, we move now to the configuration where the probe is not in contact with the solution under test. This non-contact mode is considered to be more challenging because the EMP has no direct interaction with the glucose aqueous solution. Indeed, the air in between them will leads to much attenuation. However, this configuration is regarded as non-destructive and much easier to be applied in the daily monitoring for the patients with diabetes mellitus.

For the non-contact mode characterization, the measurement goal is to differential the glucose aqueous solution from DI water to 3 mg/ml with a step as small as possible. This

step (sensitivity) has to meet the distinction requirement of the diabetes mellitus. Thus, according to the glucose characterization results in immersion mode, the frequency is set to be 2 GHz based on the sensitivity consideration. With respect to the simulation results provided in Figure III-10, it can be found that the E-field intensity decreases with the increase of the distance between the probe tip and the solution. First of all, a simulation has to be done to evaluate the E-field intensity at the air-solution interface.

III.7.2 Electromagnetic simulation of probe-solution interaction

In this section, for the non-contact mode, the electromagnetic simulation of the interaction between the probe and glucose aqueous solution without the presence of interferometer-based matching network is established. The simulation results are illustrated in Figure III-14.a, where the E-field intensity collected at the air-solution interface is strongly influenced by the distance between the EMP tip and solution. One can find that for a 'stand-off' distance spanning from 1 to 10 µm, the E-field intensity decreases from 65000 to 10000 v/cm. During this decrease, the downtrend becomes smaller for higher distances. This phenomena is with respect to the fact that the E-field is mainly confined around the probe tip and decreases rapidly away from the tip.

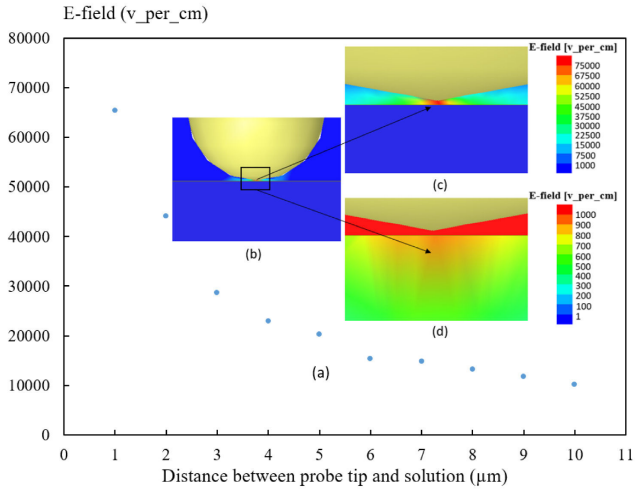

Figure III-14: Analysis of the probe-solution interaction at the cross section of the EMP tip for non-contact mode in terms of E-field intensity and distribution (a) The stand-off distances influence on the E-field intensity for a glucose concentration of 1.2 mg/ml at 2 GHz (b) E-field distribution at a standoff distance of 1 µm between the probe and solution (c) The zoom up figure of E-field distribution in air (d) The zoom up figure of E-field distribution in solution.

To better demonstrate the E-field distribution from the EMP tip to a certain depth in glucose aqueous solution which is shown in Figure III-14.b, we separate the E-field distribution into two parts, one is between the tip and air-solution interface, the other one is inside the solution, which are respectively given in Figure III-14.c and Figure III-14.d. The E-field intensity between the probe and solution is around 60000 V/cm while the one inside the solution is only about several hundred v/cm. This indicates the majority of the signal is reflected at the air-solution interface. Thus, compared to the immersion mode characterization, the non-contact mode brings more challenge in terms of sensitivity. This measurement difficulty is also proved in the Figure III-15.

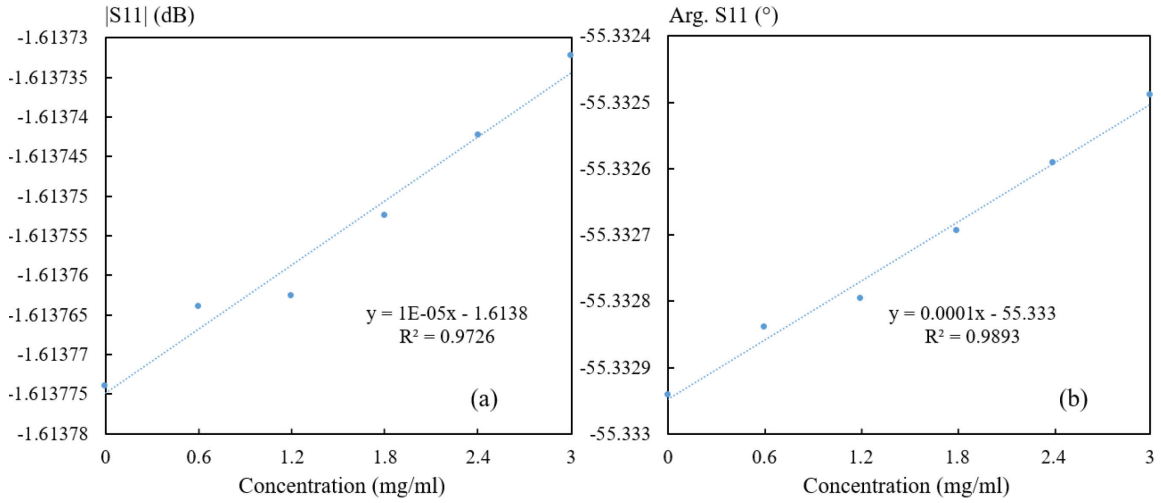

Figure III-15: The simulated reflection coefficient of glucose-water mixture for the concentration varying from 0 to 3 mg/ml at 2 GHz without the interferometer-based matching network: (a) The magnitude of the reflection coefficient (b) The phase shift of the reflection coefficient. Dashed line: fitted polynomial line at first order.

As illustrated in Figure III-15, from the simulation results, one can hardly distinguish the different glucose concentrations in terms of magnitude and phase shift of the reflection coefficient. Indeed, the obtained sensitivity is extremely small both in magnitude and in phase shite. As expected, this sensitivity is much smaller than the one find in immersion mode characterization, which indicates the higher difficulty of a characterization in non-contact mode. Nevertheless, based on the first order polynomial fitting, the acquired values show a good linearity since the coefficient of determination R^2 is greater than 0.97 in all cases.

III.7.3 Experimental procedures and measurements results

As illustrated in the previous part, the simulation results show a very low sensitivity in case of the system without the presence of interferometer-based matching network. However, a good linearity is observed which allows an assumption that a system with interferometer-based matching network can improve the sensitivity enough to distinguish small glucose concentrations. The measurement procedure is described in this section.

III.7.3.1 Experimental procedures

The experimental procedures for the non-contact mode characterization is similar to the immersion mode except that the zero level is adjusted when the EMP is above the solution. At the start of the measurement, the EMP moves slowly towards the solution with a step of 1 µm (by elevating the solution container) until a position of EMP equals to about 5 µm above the solution. This stand-off distance cannot be exactly ensured because of the existence of evaporation effect previously described. At this position, we set the zero level (cancelation level) to -55 dB and the other parameters given in Table III-1. After that, the measured transmission coefficients start to be recorded during the elevation of the plastic container until the EMP is in touch with the solution.

The measured transmission coefficient at a distance of 1 µm between the probe and solution is selected as the results. To avoid the random noise, for each sample with a fixed glucose concentration, the measurement is repeated 5 times and the average transmission coefficient is calculated.

III.7.3.2 Measurement results at 2 GHz

The measurement results are shown in Figure III-16. The evaluated transmission coefficients in terms of magnitude and phase shift correspond to the concentrations spanning from 0 to 3 mg/ml are given. It is noticed that the different glucose concentrations with a step of 0.6 mg/ml are clearly distinguished at 2.029 GHz.

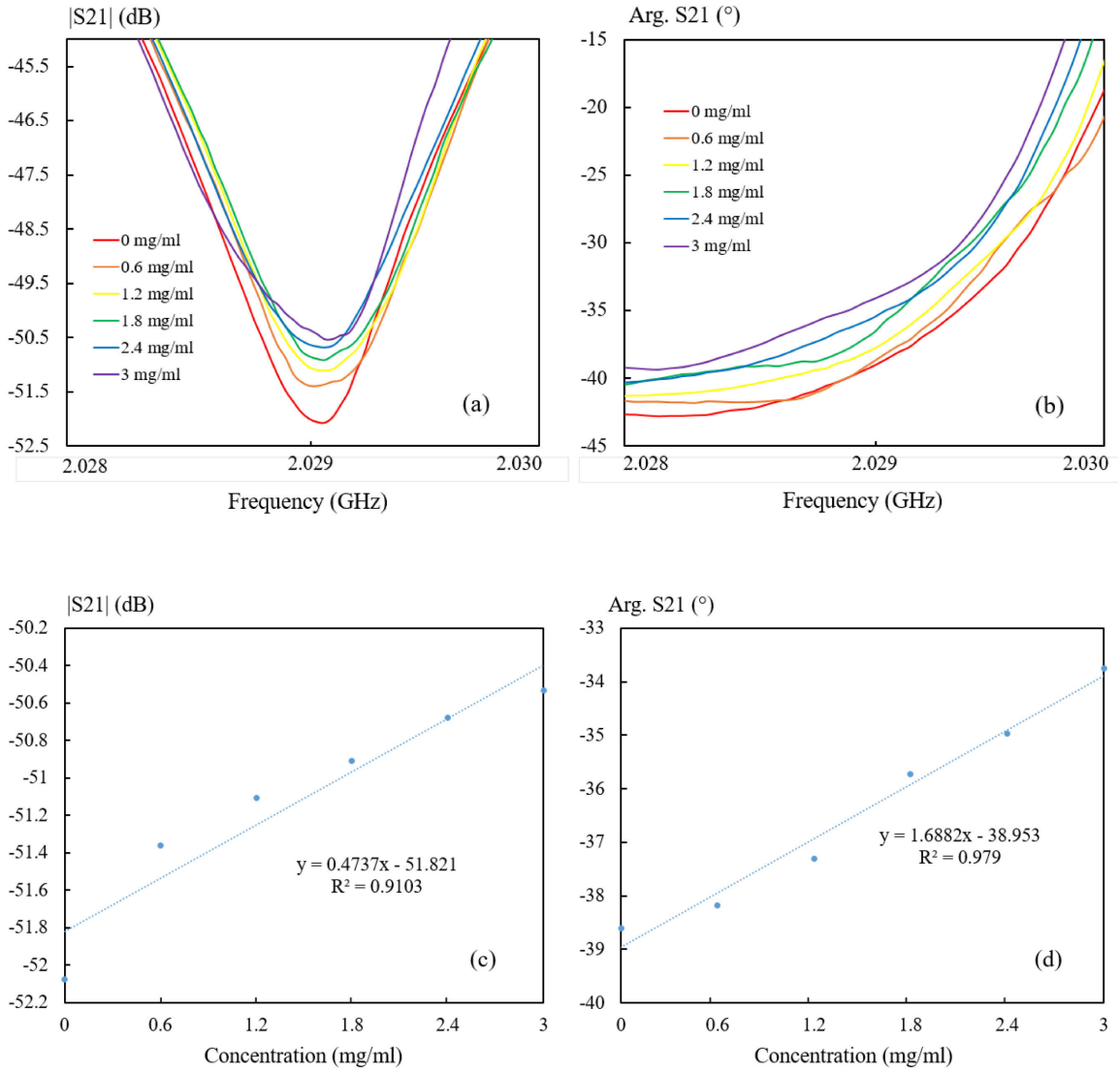

Figure III-16: Measured transmission coefficients (S_{21}) as a function of glucose concentration varying from 0 to 3 mg/ml with a step of 0.6 mg/ml at 2.029 GHz: (a) The magnitude of the transmission coefficient. (b) The phase shift of the transmission coefficient. (c) Magnitude at 2.029 GHz as a function of the glucose concentration (d) Phase shift at 2.029 GHz as a function of the glucose concentration. Dashed line: fitted polynomial line at first order.

As can be found in Figure III-16.a, b, the measured transmission coefficients in terms of magnitude and phase shift are well distinguished for all the solutions considered (from DI water to a glucose solution of 3 mg/ml with a step of 0.6 mg/ml). In Figure III-16.c, DI water gives a minimum transmission coefficient of -52.0 dB/-38.6° at 2.029 GHz while the solution with a glucose concentration of 3 mg/ml gives a maximum value of -50.5 dB/-33.8°. The dynamic range of the transmission coefficient over the 3 mg/ml concentration

range is calculated as 1.5 dB and 4.8° for the magnitude and phase shift, respectively. If we compare this dynamic range of the measured transmission coefficient to the one obtained in the immersion mode, we can report the results given in table III-3.

Mode	Dynamic range from 0 to 3 mg/ml in magnitude and phase shift	
Immersion	2.1 dB	2.5°
Non-contact	1.5 dB	4.8°

Table III-3: Dynamic range of the measured transmission coefficients from the DI water to 3 mg/ml both in magnitude and phase shift.

For the two modes characterization, the measured dynamic range for a concentration ranging from 0 to 3 mg/ml are in the same order. Even though the non-contact mode brings more challenge in terms of sensitivity, the higher IFBW gives compensation in this part and finally brings the same order of the dynamic range.

Same as the immersion mode, a dashed line is drawn by a fitted polynomial line at first order to evaluate the results' linearity. The coefficient of determination R^2 is always greater than 0.97 if one initial point is ignored, which indicate that the distribution of the transmission coefficient is correlated to glucose concentrations.

III.7.3.3 Extraction of complex permittivity for non-contact mode

Thanks to the inverse procedure given in the section III.6.2.3, the measured transmission coefficients in terms of magnitude and phase shift are translated into complex permittivity (Figure II-17). As shown in this figure, the variation of the real and imaginary part of complex permittivity determined at 2 GHz shows a linear behaviour with the variation of glucose concentration. It also demonstrates a consistent values when compared to the one described by the Debye-model.

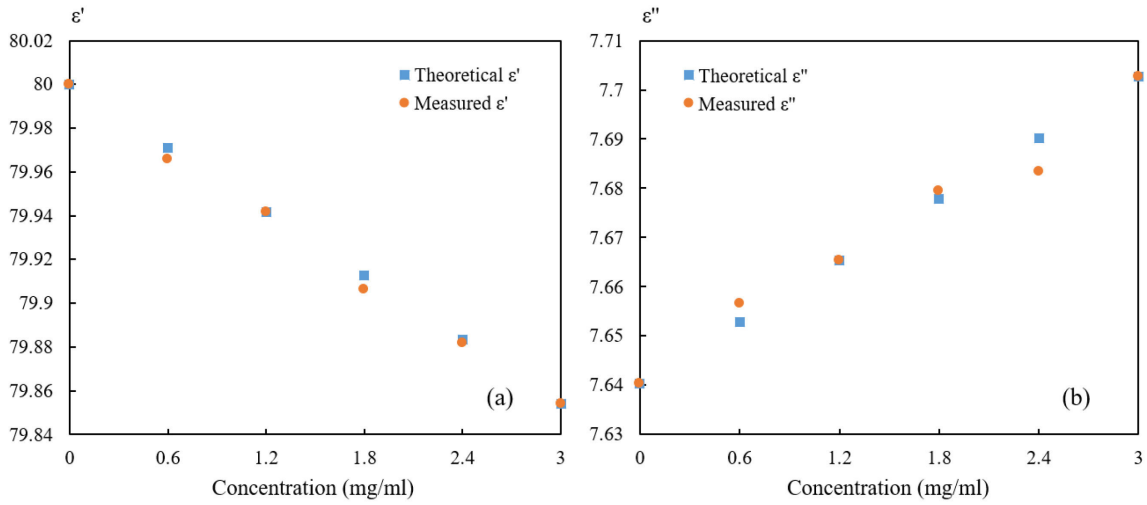

Figure III-17: The complex permittivity of glucose-water mixture for each concentration at 2 GHz: (a) Real part of the complex permittivity (b) Imaginary part of the complex permittivity.

III.7.4 Conclusion

First of all, thanks to HFSS™, the electromagnetic interaction between the EMP and the glucose solution is evaluated with different stand-off distances varying from 1 to 10 µm. As predicted theoretically, it is verified that closer the probe is to the solution, larger is the larger E-field intensity at the solution-air interface.

Thanks to the interferometer-based matching network, the sensitivity is improved which is equal to 0.32 dB/ (mg/ml) for magnitude and 0.96°/(mg/ml) for phase at 2 GHz. The glucose concentrations spanning from 0 to 3 mg/ml with a step of 0.6 mg/ml are well distinguished. After the application of the inverse procedure proposed in section III.6.3.3, the translated complex permittivity of glucose aqueous solutions for a concentration from 0 to 3 mg/ml is successfully extracted.

III.8 Conclusion

In this chapter, a brief introduction to need of the glucose aqueous solution characterization is firstly given. Different applications in varies fields have been listed. Among those evaluation methods, the interferometer-based near field microwave microscope is selected since it owns advantages such as broad operating frequency band,

high sensitivity, measurement simplicity and small volume of sample needed. After demonstrating the sensitivity improvement brought by the IBMN, the measurement repeatability is evaluated. With a well-established complex permittivity model, the glucose concentration characterization is carried out in two modes: immersion mode and non-contact mode. Based on the data collected, electromagnetic simulations are realized by HFSS™ with different configurations for the two modes. After the simulation, related experimental procedures are carried out.

In the immersion mode measurement, the transmission coefficient of glucose aqueous solutions whose concentrations vary from 0 to 10 mg/ml (physiological range) with a step of 1 mg/ml is experimentally demonstrated in a frequency band spanning from 2 to 18 GHz. An enhanced sensitivity of 0.54 dB/ (mg/ml) for magnitude and 1°/(mg/ml) for phase is obtained at 2 GHz for the immersion mode. For the non-contact mode, the glucose concentrations spanning from 0 to 3 mg/ml with a step of 0.6 mg/ml are investigated at 2 GHz. The measured sensitivity turns to be 0.53 dB/ (mg/ml) for magnitude and 1.6°/(mg/ml) for phase.

Finally, after the application of a one-port calibration, the transmission coefficients are translated into complex permittivity for each mode.

III.9 References

(44 references, Classified in alphabetical order)

[AHM 12] Ahmad, Zulkifli. "Polymeric dielectric materials." *Dielectric Material* (2012): 3-26.

[ANL 07] Anlage, Steven M., Vladimir V. Talanov, and Andrew R. Schwartz. "Principles of near-field microwave microscopy." *Scanning probe microscopy*. Springer New York, 2007. 215-253.

[BAB 06] Babajanyan, Arsen, et al. "Sodium chloride sensing by using a near-field microwave microprobe." *Applied physics letters* 89.18 (2006): 183504.

[BAG 15] Baghbani, Rasool, Masoomeh Ashoori Rad, and Ali Pourziad. "Microwave sensor for non-invasive glucose measurements design and implementation of a novel linear." *IET Wireless Sensor Systems* 5.2 (2015): 51-57.

[CHI 16] Chien, Jun-Chau, et al. "A microwave reconfigurable dielectric-based glucose sensor with 20 mg/dL sensitivity at sub-nL sensing volume in CMOS." *Microwave Symposium (IMS), 2015 IEEE MTT-S International*. IEEE.

[DEB 29] Debye, Peter Josef William. *Polar molecules*. Chemical Catalog Company, Incorporated, 1929.

[DHA 15] Dhakal, Rajendra, et al. "Complex permittivity characterization of serum with an air-bridge enhanced capacitor for quantifiable detection of glucose." *Applied Physics Letters* 106.7 (2015).

[DHK 15] Dhakal, Rajendra, et al. "Complex permittivity characterization of serum with an air-bridge enhanced capacitor for quantifiable detection of glucose." *Applied Physics Letters* 106.7 (2015): 073702.

[DOB 12] Dobson, R, Ruiheng Wu, and P. Callaghan. "Blood glucose monitoring using microwave cavity perturbation." *Electronics letters* 48.15 (2012): 905-906.

[FUC 02] Fuchs, K, and U. Kaatze. "Dielectric spectra of mono-and disaccharide aqueous solutions." *The Journal of chemical physics* 116.16 (2002): 7137-7144.

[GU 14] Gu, Sijia, Kamel Haddadi, and Tuami Lasri. "Near-field microwave microscopy for liquid characterization." *Microwave Conference (EuMC), 2014 44th European*. IEEE, 2014.

[GU 16_a] Gu, Sijia, Tianjun Lin, and Tuami Lasri. "Broadband dielectric characterization of aqueous saline solutions by an interferometer-based microwave microscope." *Applied Physics Letters* 108.24 (2016): 242903

[GU 16_b] Gu, Sijia, Tianjun Lin, and Tuami Lasri. "Dielectric properties characterization of saline solutions by near-field microwave microscopy." *Measurement Science and Technology* 28.1 (2016): 014014.

[GU 16_c] Gu, Sijia, Tianjun Lin, and Tuami Lasri. "Materials characterization by near-field scanning microwave microscopy." *Progress in Electromagnetic Research Symposium (PIERS)*. IEEE, 2016.

[GU 16_d] Gu, S., Haddadi, K., El Fellahi, A., & Lasri, T. (2016). Setting parameters influence on accuracy and stability of near-field scanning microwave microscopy platform. *IEEE Transactions on Instrumentation and Measurement*, *65*(4), 890-897.

[GUB 15] Gubin, Alexey I, et al. "Whispering-gallery-mode resonator technique with microfluidic channel for permittivity measurement of liquids." *IEEE transactions on microwave theory and techniques* 63.6 (2015).

[GYO 98] Gyorgydeak, Zoltan, and Istvan Pelyvas. Monosaccharide Sugars: Chemical synthesis by chain elongation, degradation, and epimerization. *Academic Press*, 1998.

[HAY 03] Hayashi, Yoshihito, et al. "Dielectric spectroscopy study of specific glucose influence on human erythrocyte membranes." *Journal of Physics D: Applied Physics* 36.4 (2003).

[HE 01] He, J., Watkins, S, & Kelley, D. E. (2001). Skeletal muscle lipid content and oxidative enzyme activity in relation to muscle fiber type in type 2 diabetes and obesity. *Diabetes*, *50*(4), 817-823.

[HOF 13] Hofmann, Maximilian, et al. "Microwave-based noninvasive concentration measurements for biomedical applications." *IEEE Transactions on Microwave Theory and Techniques* 61.5 (2013): 2195-2204.

[INT 15] International Diabetes Federation, IDF diabetes atlas, 7th edition (2015).

[KAR 13] Karacolak, Tutku, Elaine C. Moreland, and Erdem Topsakal. "Cole–cole model for glucose-dependent dielectric properties of blood plasma for continuous glucose monitoring." *Microwave and Optical Technology Letters* 55.5 (2013): 1160-1164.

[LAM 06] Lampreia, Isabel MS, et al. "Solubility of proline–leucine dipeptide in water and in aqueous sodium chloride solutions from T= (288.15 to 313.15) K." *The Journal of Chemical Thermodynamics* 38.3 (2006): 240-244.

[LEE 08] Lee, Kiejin, et al. "Glucose aqueous solution sensing by a near-field microwave microprobe." *Sensors and Actuators A: Physical* 148.1 (2008): 28-32.

[LEE 12] Lee, Hee-Jo, et al. "A planar split-ring resonator-based microwave biosensor for label-free detection of biomolecules." *Sensors and Actuators B: Chemical* 169 (2012): 26-31.

[MAS 92] Mashimo, Satoru, Nobuhiro Miura, and Toshihiro Umehara. "The structure of water determined by microwave dielectric study on water mixtures with glucose, polysaccharides, and L-ascorbic acid." *The Journal of chemical physics* 97.9 (1992): 6759-6765.

[NAK 16] Nakamura, Masahito, et al. "Selectivity-enhanced glucose measurement in multi-component aqueous solution by broadband dielectric spectroscopy." *Microwave Symposium (IMS), 2016 IEEE MTT-S International*. IEEE, 2016.

[NAN 97] Nandi, Nilashis, and Biman Bagchi. "Dielectric relaxation of biological water." *The Journal of Physical Chemistry B* 101.50 (1997): 10954-10961.

[NOT 06] Note, A. A. (2006). Agilent Basics of Measuring the Dielectric Properties of Materials. *Agilent Literature Number*.

[RAI 98] Raicu, V, T. Saibara, and A. Irimajiri. "Dielectric properties of rat liver in vivo: a noninvasive approach using an open-ended coaxial probe at audio/radio frequencies." *Bioelectrochemistry and Bioenergetics* 47.2 (1998): 325-332.

[SCH 13] Schwerthoeffer, U, R. Weigel, and D. Kissinger. "A highly sensitive glucose biosensor based on a microstrip ring resonator." *Microwave Workshop Series on RF and Wireless Technologies for Biomedical and Healthcare Applications (IMWS-BIO), 2013 IEEE MTT-S International*. IEEE, 2013.

[SCH 14] Schwerthoeffer, U., Weigel, R., & Kissinger, D. (2014, May). Highly sensitive microwave resonant near-field sensor for precise aqueous glucose detection in microfluidic medical applications. In *Instrumentation and Measurement Technology Conference (I2MTC) Proceedings, 2014 IEEE International* (pp. 919-922). IEEE.

[SEN 16] Sen, K., & Anand, S. (2016). Determination of Glucose-Dependent Dielectric Properties of Ringer Lactate Using Open-Ended Coaxial Probe Method. *MAPAN*, *31*(3), 225-230.

[SHI 15] Shiraga, Keiichiro, et al. "Broadband dielectric spectroscopy of glucose aqueous solution: Analysis of the hydration state and the hydrogen bond network." *The Journal of chemical physics* 142.23 (2015): 234504.

[TAL 07] Talary, Mark S, et al. "In vivo life sign application of dielectric spectroscopy and non-invasive glucose monitoring." *Journal of Non-Crystalline Solids* 353.47 (2007): 4515-4517.

[TUC 16] Tuca, Silviu-Sorin, et al. "Calibrated complex impedance of CHO cells and E. coli bacteria at GHz frequencies using scanning microwave microscopy." *Nanotechnology* 27.13 (2016): 135702.

[TUR 07] Tura, Andrea, et al. "Dielectric properties of water and blood samples with glucose at different concentrations." *11th Mediterranean Conference on Medical and Biomedical Engineering and Computing 2007*. Springer Berlin Heidelberg, 2007.

[TUR 15] Turgul, Volkan, and Izzet Kale. "On the accuracy of complex permittivity model of glucose/water solutions for non-invasive microwave blood glucose sensing." *E-Health and Bioengineering Conference (EHB), 2015*. IEEE.

[TUR 16] Turgul, Volkan, and Izzet Kale. "A novel pressure sensing circuit for non-invasive RF/microwave blood glucose sensors." *Microwave Symposium (MMS), 2016 16th Mediterranean*. IEEE, 2016.

[TUR 17] Turgul, V, and I. Kale. "Influence of fingerprints and finger positioning on accuracy of RF blood glucose measurement from fingertips." *Electronics Letters* 53.4 (2017): 218-220.

[VAS 12] Vashist, Sandeep Kumar. "Non-invasive glucose monitoring technology in diabetes management: A review." *Analytica chimica acta* 750 (2012): 16-27.

[YAN 11] Yan, Qinyi, et al. "Measurement of tear glucose levels with anemometric glucose biosensor/capillary tube configuration." *Analytical chemistry* 83.21 (2011): 8341-8346.

[ZHA 12] Zhadobov, Maxim, et al. "Complex permittivity of representative biological solutions in the 2–67 GHz range." *Bioelectromagnetics* 33.4 (2012): 346-355.

[ZHA 14] Zhang, Ling Yan, et al. "Discrimination of colorectal cancer cell lines using micro-wave biosensors." *Sensors and Actuators A: Physical* 216 (2014): 405-416.4

Chapter IV

The improvement of iNFMM: multi-port reflectometer based on broadband multi-layer coupler

Chapter IV : The improvement of iNFMM: multi-port reflectometer based on broadband multi-layer coupler

IV.1 Introduction to multi-port reflectometers

The fundamental works on multi-port technique are firstly proposed in the 1970s by Engen [ENG 77_a], [ENG 77_b] and Hoer [HOER 77]. In these references, the term 'six-port' is mentioned for the first time. Since then, both in theoretical and experimental fields, many excellent works have contributed to the development of this technique [ENG 79], [MOL 06] [HAD 13] [TAT 13] [HAN 15] [WIL 17]. A six-port acts as a network analyzer and is able to measure the complex impedance of a device under test. The complex impedance is characterized in terms of reflection coefficient, which explains in part the name given to this system.

The six-port reflectometer is basically a circuit made of passive components including couplers and power dividers. In particular, these components are chosen as a function of the propagation structure and the operating frequency. Generally, the six-port reflectometer has two input ports and four output ports. The generated output signals are the combination of these two input signals with a different phase shift [GHA 09].

Compared to the conventional network analyzer, the six-port technique owns a major advantage, which is related to the only utilization of scalar measurements such as power or voltage. As well known, the conventional network analyzer is based on a receiver architecture that mixes the received microwave signal to a lower intermediate frequency (IF) by means of a local oscillator. The magnitude and phase information extracted from the IF signal are obtained thanks to an analog-to-digital converter (ADC) and a digital-signal processor (DSP) [AGI 13]. Nevertheless, these required hardware are expensive and take up space in the system. Compared to the conventional network analyzer, the structure of a six-port reflectometer is simple and cost effective. Furthermore, the simplified structure makes it easier for its use in portable applications. When talking about the

measurement precision, with the help of calibration techniques, the calibrated six-port reflectometer can achieve a relatively high precision compared to the conventional network analyzer [HAD 08]. Hence, the six-port technique is considered as a good alternative solution for the reflection coefficient measurement.

To date, many applications are based on the six-port technique such as the six-port-based near field microwave microscopy [HAD 13], precise alignment measurements [KOE 16], radar application [ZHA 08], [VIN 16], telecommunication [HAD 10] and heart rate detection [WIL 15]. Depending on the application, different six-port reflectometers can be found in different structures, but the overall trend is related to the compactness and broadband features in the microwave/millimeter wave frequency band [BAU 15].

Thanks to the excellent work of the researchers involved in this task, the six-port technology and related applications have been substantially developed. In the next section, some typical six-port junctions are presented with their main components. Based on our design target, the proposed six-port reflectometer is described in section IV.3, where the design procedure, fabrication methods and measurement results are also demonstrated. After that, the six-port reflectometer is given with a broadband characterization and finally comes with the conclusion.

IV.2 Typical six-port reflectometer junctions

IV.2.1 Introduction

As already said, the components inside the six-port junctions are mainly chosen according to the working frequency which corresponds to targeted applications. In this section, the two most popular junctions and the components associated are discussed in details. Then, we present our strategy for the selection of our design.

IV.2.2 Six-port junction with hybrid couplers and a power divider

IV.2.2.1 Theoretical basis

The most common six-port junction is composed of a Wilkinson power divider and three hybrid couplers as shown in Fig I-1[WIL 15]:

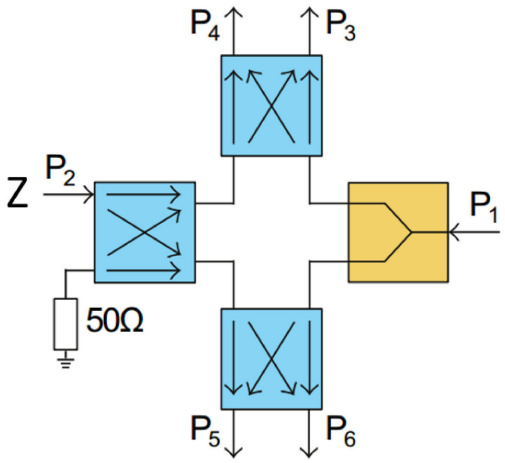

Figure IV-1: Schematic of a six-port junction [WIL 15].

The main idea of this structure is to superimpose the two input signals P_1 and P_2 by means of the Wilkinson power divider and the hybrid couplers. The input signals are delivered to four output signals (P_3 to P_6) with a static phase shift of $\pi/2$ amongst each other. Based on the theoretical derivation provided in [WIL 15], the two input signals P_1 and P_2 are defined in complex forms by the following expressions:

$$\begin{aligned} P_1 &= A_1\,[\cos(\omega t + \Phi_1) + j\sin(\omega t + \Phi_1)] \\ P_2 &= A_2\,[\cos(\omega t + \Phi_2) + j\sin(\omega t + \Phi_2)] \end{aligned} \qquad (IV-1)$$

Where A_1 and A_2 denote the amplitudes, ω represent the angular frequency and the Φ is the phase value of each signal. As demonstrated in Figure IV-1, the power divider splits the input signal P_1 equally into two parts while the coupler separates the input signal P_2 into two signals with the same magnitude but a phase difference of 90°. Therefore, the

output signal P_3 can be calculated by the addition of a half of P_1 and a half of P_2 with a 90° phase shift. The other output signals can be written in the same way as given in the following equation:

$$\begin{aligned} P_3 &= 0.5 * (P_1 + jP_2) \\ P_4 &= 0.5 * (jP_1 + P_2) \\ P_5 &= 0.5 * (jP_1 + jP_2) \\ P_6 &= 0.5 * (P_1 - P_2) \end{aligned} \qquad (IV-2)$$

One can note that the relative phase shift between the four output signals are 90°. Thus, a complex representation of Z can be obtained with the in-phase and quadrature components. This obtained impedance Z is derived as follows:

$$Z = I + jQ = (P_5 - P_6) + j(P_3 - P_4) \qquad (IV-3)$$

Once Z is given, the reflection coefficient Γ can be calculated by the well-known equation:

$$\Gamma = \frac{Z - Z_s}{Z + Z_s} \qquad (IV-4)$$

Where Z_s is the source impedance of 50 Ω. After this very brief recall of the theoretical principle of the six-port junction with hybrid couplers and power divider. This structure can be applied as a six-port network in various applications.

IV.2.2.2 Components selection strategy

As illustrated in Figure IV-1, the main components of the described junction are the hybrid coupler and the power divider. Since the six-port junction is a passive structure, its working frequency depends on the operating bandwidth of the components considered for

its realization. Thus, the components selection strategy is related to the working frequency and consequently to the targeted applications.

For the power divider, the Wilkinson type is the most popular one as it owns a great advantage with respect to the design facility and the frequency band achievable. Indeed, the multi-section Wilkinson power divider can achieve an operating frequency over several octaves in the microwave range [WEI 15], [HON 17]. The one realized with SIW technology also provides a good performance in the millimeter range [MAN 15].

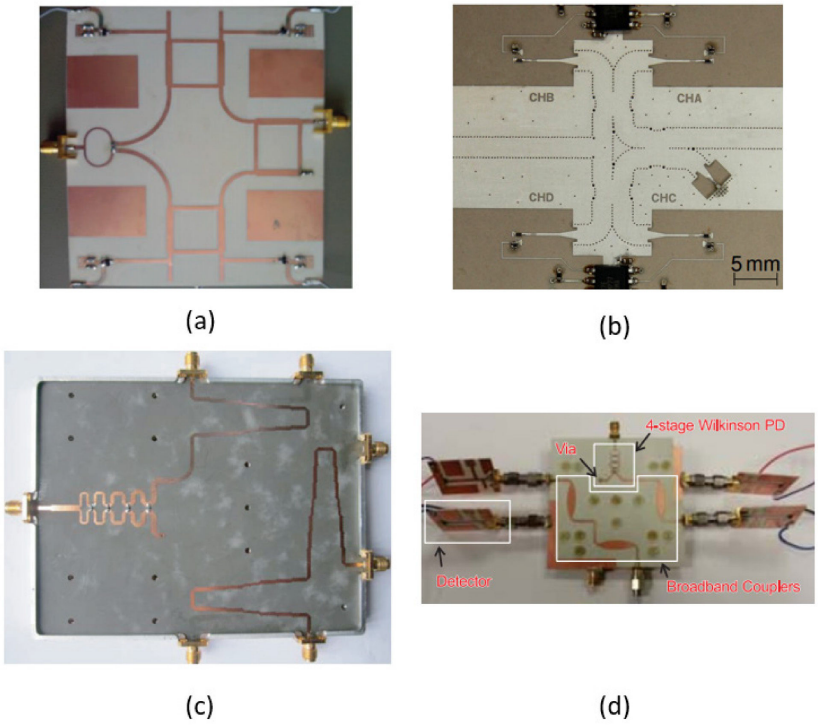

Figure IV-2: Different types of hybrid couplers integrated in a six-port junction. (a) Branch line coupler [QAY 14] (b) Short-slot coupler in SIW [MAN 15] (c) Multi-section coupler in tandem structure [HON 17] (d) Elliptical microstrip-slot coupler [WEI 15].

Compared to the power divider, a large choice of hybrid couplers is available. Indeed, many types of coupler can be chosen according to their technology and operating frequency band. For instance, in Figure IV-2, different types of hybrid couplers are included within a six-port junction.

As demonstrated in Figure IV-2, the four examples of six-port junctions make use of a Wilkinson power divider but different kinds of hybrid couplers. One can find in the Table.IV-1, the operation bandwidth corresponding to the different types of couplers considered in these examples.

Coupler types	Working bandwidth (GHz)
Branch line	1-3.3
Short-slot	60-62
Multi-section	2-8
Elliptical microstrip-slot	0.5-5

Table IV-1： The working frequency range for the four types of coupler illustrated in Figure IV-2.

Indeed, the six-port junction with three hybrid couplers and a power divider is considered as the most popular structure. Nevertheless, other junctions can also provide a comparable performance in terms of design facility and frequency band. In the next section, a junction with only hybrid couplers is described.

IV.2.3 Six-port junction with only hybrid couplers

IV.2.3.1 Theoretical basis

According to the configuration illustrated in Figure IV-3, the six-port junction is based on five couplers. Without the existence of the Wilkinson power divider, the design complexity is even more decreased. As shown in the figure, this configuration, includes four power detectors, five 3 dB/90° broadband couplers and the transitions between them. As a result, the performance of the six-port reflectometer is mainly dependent on the couplers properties.

The reflection coefficient (Γ) can be therefore calculated from the power measured by the four detectors (P_3 to P_6) when connecting a DUT at port 2. Assuming that the five couplers ensure ideal -3 dB coupling and the system is lossless, the reflection coefficient Γ is given by [SEM 06]:

$$\Gamma = \frac{P_5 + P_6 - P_3 - P_4}{4P_4} + j\frac{P_6 - P_5}{2P_4} \qquad (IV-5)$$

It has been demonstrated that this reflection coefficient can also be expressed as a function of the reflectometer S-parameters by the following equation:

$$\Gamma = \frac{|S_{51}|^2 + |S_{61}|^2 - |S_{31}|^2 - |S_{41}|^2}{4|S_{41}|^2} + j\frac{|S_{61}|^2 - |S_{51}|^2}{2|S_{41}|^2} \qquad (IV-6)$$

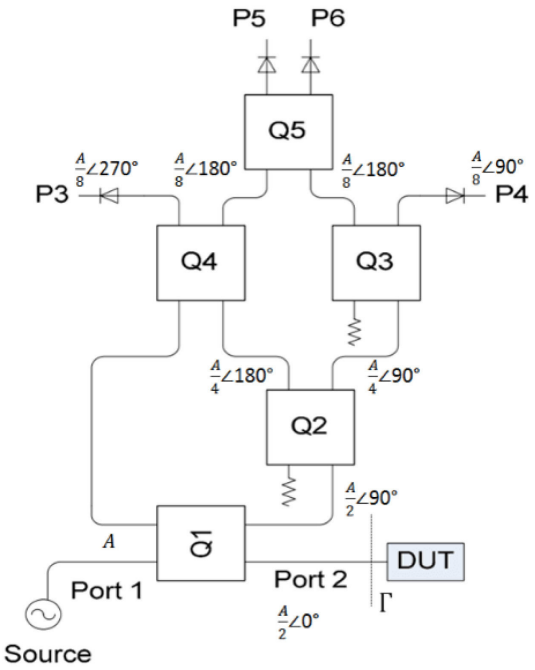

Figure IV-3: Six-port reflectometer conceptual diagram where Qi (i= 1 to 5) is a 3 dB/90° coupler

Thus, when applying this junction, much attention has to be given to the design of the coupler.

IV.2.3.2 Six-port reflectometer with only couplers

Based on the conceptual diagram given above in Figure IV-3, a six-port reflectometer has been designed as illustrated in Figure IV-4:

As can be seen from the figure, five branch line couplers are implemented in the proposed six-port junction with a fine designed interconnection. To get through the frequency band limitation of a branch line coupler, the authors apply the defect ground structure (DGS) technique on the bottom side of the coupler, where a ring headed dumbbell is etched in order to not only improve the bandwidth but also better control the characteristic impedance [SHU 14].

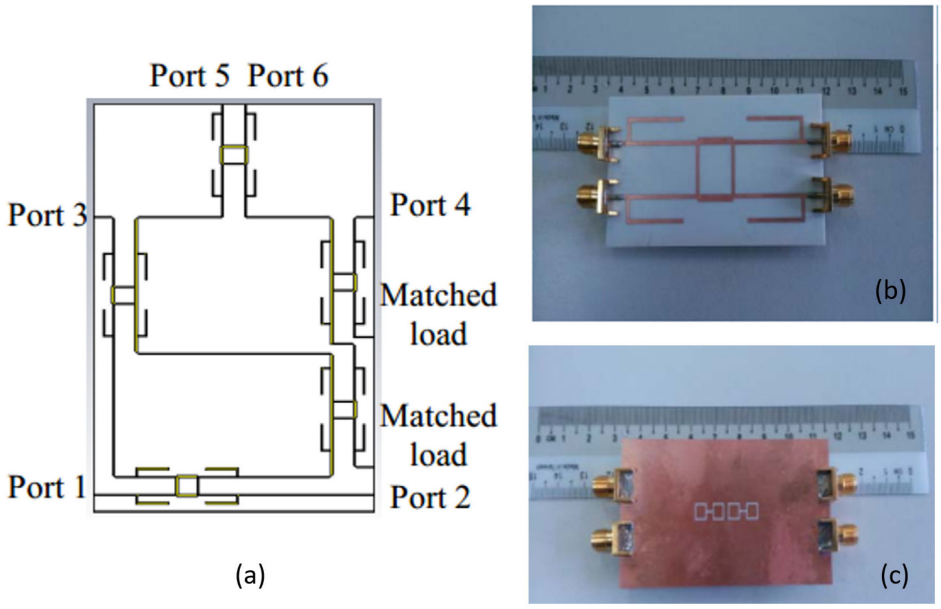

Figure IV-4: The six-port reflectometer with five branch line couplers (a) The layout of branch line coupler (b) Top view of branch line coupler (c) Bottom view of branch line coupler using defect ground structure technique (DGS) [SHU 14].

This six-port reflectometer can achieve an operating frequency band ranging from 2.5 to 4 GHz [SHU 14].

IV.2.4 Conclusion

In this section, a brief presentation of the six-port reflectometer is given firstly. After that, two six-port junctions are discussed theoretically in terms of reflection coefficient measurement. Different examples using the given junctions are also demonstrated. Mainly based on consideration such as simplicity on the design, the junction with only couplers is chosen as our design basis. In the next part, the coupler to be included in the six-port reflectometer is under investigation.

IV.3 Broadband multi-layer coupler design

IV.3.1 Introduction

As described in section II, two kinds of six-port junctions as well as the associated components are briefly presented. One can note that the broadband coupler plays an important role in the discussed junctions. Thus, in this section, we propose a broadband multi-layer coupler which is able to meet the requirements of a six-port reflectometer.

IV.3.2 The broadband coupler selection

The broadband coupler candidate for an integration in the six-port reflectometer is described in this section. In our design goal, the reflectometer should be able to operate from 2 to 20 GHz in order to cover the bandwidth that corresponds to the near field microwave microscopy platform.

As discussed in the section IV.2.3.2, a method to increase the bandwidth of a branch line coupler named as Defect Ground Structure (DGS) can be used [SHU14]. The DGS presents a rectangular ring headed dumbbell shape which can enhance the bandwidth of 11% compared to the conventional branch line coupler. However, this limited bandwidth is not large enough for an ultra-large band application from 2 to 20 GHz.

For a conventional rat-race coupler, the bandwidth is about 20% but can be increased by using a multi-section impedance transformer [GRU 12] to attain a bandwidth of about an octave. But this bandwidth remains too small when considering our objective. In addition, because of the physical discontinuities at the junctions of the rat-race, the insertion loss are important at high frequency, which is not suitable for our reflectometer.

The multi-section directional coupler is one of the candidates for the six-port reflectometer topology [KIM 04]. Actually, its bandwidth can potentially attain several octaves. Nevertheless, the major disadvantage of the multi-section structure is the abrupt change between each section along the transmission line. This discontinuity leads to a poor

matching which is even more pronounced at high frequency. To avoid these frank physical discontinuities, a continuous variation along the coupling path of the coupler could be implemented. Therefore, the non-uniform coupler appears as a possible solution for the reflectometer bandwidth enlargement.

In the next section, we discuss the theory and the design procedure of the proposed ultra large band coupler. In addition to the bandwidth performance, several methods have been applied in order to increase the matching and isolation capabilities. The improvements brought by the solution investigated are evaluated by using the finite element environment based platform, HFSS™. The fabrication method is also proposed and finally the measurement results are presented.

IV.3.3 Multi-layer coupler design

IV.3.3.1 Tandem configuration

When designing an ultra large band coupler, the difficulty is to achieve a desired coupling factor in the entire frequency band. In the reference [SHE 66_a], the authors present a possible solution to figure out this problem. The idea consists in discretizing the coupling path into small elements. These elements are well positioned in order to perform different coupling factors, which have to be carefully calculated. After reconnecting them as a successive coupling path, it can achieve a flat coupling factor in the entire frequency band. With respect to this idea, in our design, a 3 dB coupler with tandem configuration can be realized by cascading two couplers together [ANS 14], [MON 07].

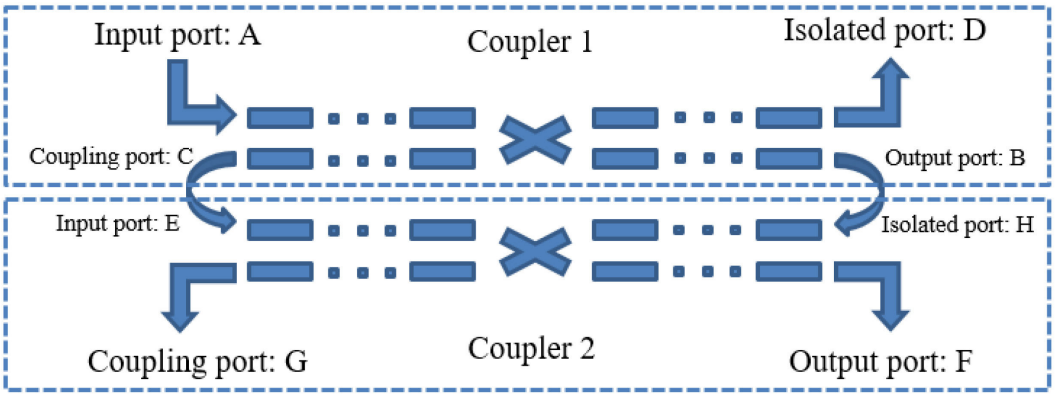

Figure IV-5: Tandem structure to realize a 3 dB coupler by cascading two couplers.

As shown in Figure IV-5, for the first coupler, an incident signal feeds the input port A and is divided in two parts that travel toward the output port B and the coupling port C. In ideal case, there is no signal at the isolated port D. With such a tandem arrangement, the output port B and coupling port C of the first coupler are respectively connected to the input port E and isolated port H of the second coupler. In the following part, the theoretical derivation that determines which coupling factor should be chosen for the two identical couplers to produce a 3 dB coupling is given in details.

As a four port component (Figure IV-6), the coupler operation can be completely described by a 4*4 scattering matrix. The numbering chosen for the coupler ports is the following: 1 is related the input port A in the Figure IV-5, 2 refers to the output port B, 3 corresponds to coupling port C while the 4 is the isolated port D.

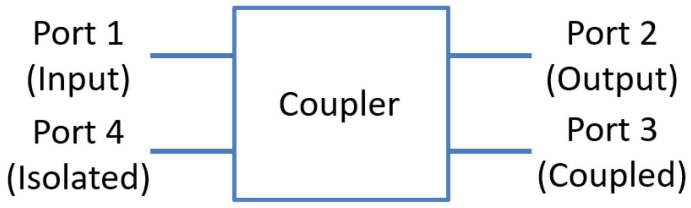

Figure IV-6: The coupler: a four port network.

$$\text{Scattering matrix of a coupler} = [S] = \begin{bmatrix} S11 & S12 & S13 & S14 \\ S21 & S22 & S23 & S24 \\ S31 & S32 & S33 & S34 \\ S41 & S42 & S43 & S44 \end{bmatrix}$$

For an ideal TEM mode coupler, all the ports are matched ($S_{11} = S_{22} = S_{33} = S_{44} = 0$). Because of the symmetric character of the coupler, the input port and the isolated port (Figure III-6) are regarded as identical. The same stands for the coupling port and the output port. Additionally, the isolated port is always independent from the input port and the network is reciprocal, Thus, $S_{14} = S_{41} = S_{23} = S_{32} = 0$ and $S_{12} = S_{21} = S_{34} = S_{43}$. Since an ideal TEM mode coupler is lossless, the signal at the input port is fully transmitted to the output port and the coupling port while occurs a 90° phase shift between the output ports and the coupling ports. Therefore, ${S_{12}}^2 + {S_{13}}^2 = 1$. Based on the analysis given above and to meet these conditions, we give a possible value respectively for S_{12} and S_{13} where the $S_{12} = -i\cos(\alpha)$ and $S_{13} = sin(\alpha)$, the scattering parameters of the TEM mode coupler are therefore given by the following matrix [MON 07]:

$$[S] = \begin{bmatrix} 0 & -i\cos(\alpha) & \sin(\alpha) & 0 \\ -i\cos(\alpha) & 0 & 0 & \sin(\alpha) \\ \sin(\alpha) & 0 & 0 & -i\cos(\alpha) \\ 0 & \sin(\alpha) & -i\cos(\alpha) & 0 \end{bmatrix}$$

Where sin(α) is the coupling coefficient of the coupler. With respect to the topology given in Figure IV-5, if a signal is injected at the input port A, the signal at the output port B and coupling port C of the first coupler can be predicted by using the scattering parameters.

$$\begin{bmatrix} A \\ B \\ C \\ D \end{bmatrix} = \begin{bmatrix} 0 & -i\cos(\alpha) & \sin(\alpha) & 0 \\ -i\cos(\alpha) & 0 & 0 & \sin(\alpha) \\ \sin(\alpha) & 0 & 0 & -i\cos(\alpha) \\ 0 & \sin(\alpha) & -i\cos(\alpha) & 0 \end{bmatrix} * \begin{bmatrix} 1 \\ 0 \\ 0 \\ 0 \end{bmatrix}$$

This gives:

$$\begin{aligned} B &= -i\cos(\alpha); \\ C &= \sin(\alpha) \\ D &= 0; \end{aligned} \qquad (IV-7)$$

As the output port B and the coupling port C are connected to the isolated port H and the input port E of the second coupler, respectively, the signals at the ports B and H should be identic and the signals at the port C and E should also be the same.

$$\begin{aligned} H = B &= -i\cos(\alpha); \\ E = C &= \sin(\alpha) \end{aligned} \qquad (IV-8)$$

To calculate the signals at the output port F and at the coupling port G, one can use the results found for E and H:

$$\begin{bmatrix} E \\ F \\ G \\ H \end{bmatrix} = \begin{bmatrix} 0 & -i\cos(\alpha) & \sin(\alpha) & 0 \\ -i\cos(\alpha) & 0 & 0 & \sin(\alpha) \\ \sin(\alpha) & 0 & 0 & -i\cos(\alpha) \\ 0 & \sin(\alpha) & -i\cos(\alpha) & 0 \end{bmatrix} * \begin{bmatrix} \sin(\alpha) \\ 0 \\ 0 \\ -i\cos(\alpha) \end{bmatrix}$$

After the matrix calculation, the signals from port E and H are transmitted to port F and G, this leads to:

$$\begin{aligned} F &= -i\cos(\alpha) * \sin(\alpha) + \sin(\alpha) * -i\cos(\alpha) = -i\sin(2\alpha) \\ G &= \sin(\alpha) * \sin(\alpha) + -i\cos(\alpha) * -i\cos(\alpha) = -\cos(2\alpha); \end{aligned} \qquad (IV-9)$$

With the tandem configuration, a 3 dB coupling is expected. To ensure that the magnitude of the signal at the output port F is equal to the one at the coupling port G, one should verify the following expression:

$$|F| = |G| = |-\cos(2\alpha)| = |-i\sin(2\alpha)| \qquad (IV-10)$$

To that end, 2α should be equal to $\frac{\pi}{4}$, which means that α is equivalent to $\frac{\pi}{8}$. Thus, the coupling (c = sin (α)) in decibels is given as:

$$\text{Coupling factor R} = -20\log\left(\sin\left(\frac{\pi}{8}\right)\right) = 8.34\ \text{dB} \qquad (\text{IV}-11)$$

Thanks to the theoretical derivation, a 3 dB coupler that can be realized by placing two 8.34 dB couplers in tandem structure is demonstrated. Once the cascade structure of two 8.34 dB couplers is chosen, the design of a non-uniform broadband TEM directional coupler is started. In the next section, we introduce the design procedure of the proposed coupler in details. The first step is to derive the even/odd mode impedance of each small element which consist of the coupling path.

IV.3.3.2 Theoretical derivation for even mode impedance

Generally, a typical coupler performs a coupling factor between two coupled paths. To evaluate such coupling factor, one should make use of the even/odd mode analysis method provided in the references [MON 07] [YIG 12]. As presented in Figure IV-7, the planes (OO') and (PP') in between the two symmetric coupled lines act like an electric or magnetic wall.

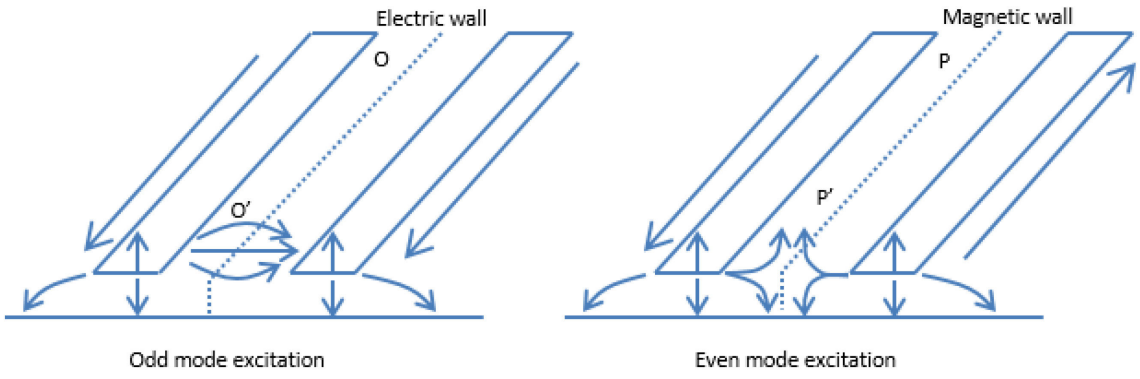

Figure IV-7: Even/odd mode excitation of the two coupled lines.

The scattering parameters of a symmetric four ports network two-coupled lines are given by the following matrix [MON 07]:

$$\begin{bmatrix} \frac{S11e + S11o}{2} & \frac{S21e + S21o}{2} & \frac{S11e - S11o}{2} & \frac{S21e - S21o}{2} \\ \frac{S21e + S21o}{2} & \frac{S22e + S22o}{2} & \frac{S21e - S21o}{2} & \frac{S22e - S22o}{2} \\ \frac{S11e - S11o}{2} & \frac{S21e - S21o}{2} & \frac{S11e + S11o}{2} & \frac{S21e + S21o}{2} \\ \frac{S21e - S21o}{2} & \frac{S22e - S22o}{2} & \frac{S21e + S21o}{2} & \frac{S22e + S22o}{2} \end{bmatrix}$$

Where $S_{11e/o}$ and $S_{21e/o}$ are respectively the reflection coefficients and the transmission coefficients of the even/odd mode signals. As recalled in the previous part, for a TEM type coupler, the following conditions are respected:

$$\begin{aligned} &S_{11} = S_{22} = S_{33} = S_{44} = 0 \\ &S_{14} = S_{41} = S_{23} = S_{32} = 0 \\ &S_{12} = S_{21} = S_{34} = S_{43} \neq 0 \\ &S_{24} = S_{42} \neq 0, S_{13} = S_{31} \neq 0 \end{aligned} \qquad (IV-12)$$

Therefore, if we apply these conditions to the matrix given above, the relation between the even and odd mode signals at each port can be found:

$$S_{11e} = -S_{11o},\ S_{22e} = -S_{22o} \text{ and } S_{21e} = S_{21o} \qquad (IV-13)$$

With respect to these relations, the matrix representing the four port network can be reduced to:

$$\begin{bmatrix} 0 & S21e & S11e & 0 \\ S21e & 0 & 0 & S22e \\ S11e & 0 & 0 & S21e \\ 0 & S22e & S21e & 0 \end{bmatrix}$$

The paper [CRI 66] demonstrates that the coupling factor of a TEM-mode multi-section coupler can be analyzed from the even/odd mode impedance of each section. As well known, this latter is strongly linked to the physical dimensions of each section. Thus, with a design goal of an equal-ripple and maximally-flat coupling in the entire frequency band, it is suggested to vary the physical dimensions of each section along the length of the coupling path. From the Cristal and Young's table [CRI 66], if the dimension of each coupled line is well chosen, the impedance of the even and odd mode respectively $Z_{oe}$and Z_{oo} should satisfy the following condition:

$$\sqrt{Z_{oe} * Z_{oo}} = Z_o = 50\Omega \qquad (\text{IV} - 14)$$

Thanks to the transmission line theory and small signal analysis, the coupling between the input port and the coupling port can be finally determined by the equation given in the reference [TRE 66]:

$$S_{31} = -je^{-j\beta d} \int_{-d/2}^{d/2} \sin(2\beta u) p(u) du$$

where, $$p(u) = \frac{1}{2}\frac{d}{du}\ln(Z_{oe}) \qquad (\text{IV} - 15)$$

and $$d = \frac{n}{\beta_c}\pi$$

As mentioned above, the coupling factor depends on the even/odd mode impedance of each section, which is described by $\mathrm{p}(u)$. The parameter d is the overall length of the coupling path (Figure IV-9), β is the wave propagation constant in air and β_c is the phase constant of the coupler for the center frequency f_o (11 GHz) in our case. Since this design is based on a nine section coupler illustrated in Figure IV-8, the sections at two sides are symmetric to the middle section, thus, we consider here the n equals to 5 when looking to one side of the coupler as indicated by the flash.

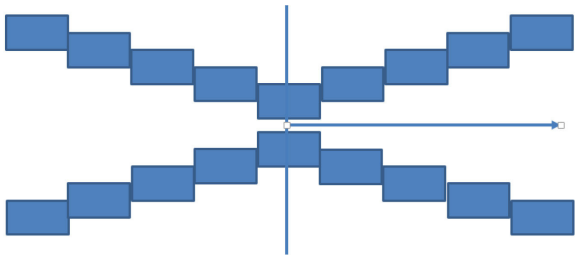

Figure IV-8: Schematic of a nine-section coupler.

To achieve a maximum coupling and bandwidth, $p(u)$ can be derived as [TRE 66]:

$$p(u) = -\frac{R}{\pi}\frac{\sin^2\left(\frac{u}{2}\right)}{\frac{u}{2}} \qquad (\text{IV}-16)$$

Where R is the coupling factor in decibels (8.34 dB in this case) and u is a variable representing the distance of each element from the mid one. Since the equation (IV-16) is infinite and to avoid the Gibb's phenomenon (ringing problem) [CRI 66], the ripple level may be equalized by using the weighting technique and a weighting function $w(u)$ is inserted into $p(u)$.

$$p_w(u) = p(u) * w(u) \qquad (\text{IV}-17)$$

The weighting function can be calculated using the method given in [TRE 66]:

$$W_1 = ln\left(\frac{Z_{oe5}}{Z_{oe4}}\right) * \pi * \frac{1}{R*4}$$

$$W_2 = ln\left(\frac{Z_{oe4}}{Z_{oe3}}\right) * \pi * \frac{3}{R*4}$$

$$W_3 = ln\left(\frac{Z_{oe3}}{Z_{oe2}}\right) * \pi * \frac{5}{R*4} \qquad (\text{IV}-18)$$

$$W_4 = ln\left(\frac{Z_{oe2}}{Z_{oe1}}\right) * \pi * \frac{7}{R*4}$$

$$W_5 = ln\left(\frac{Z_{oe1}}{Z_o}\right) * \pi * \frac{9}{R * 4}$$

Once the weighting function is calculated, the final even mode impedance can be derived as the integral of the even mode impedance of each element along the coupling path by using the equations from IV-14 to IV-18:

$$\frac{1}{2} ln \frac{Z_{oe}(u)}{Z_o} = \int_{-d/2}^{u} p_w(u)du = \int_{-d/2}^{u} w(u)p(u)du = -\frac{R}{\pi}\int_{-d/2}^{u} w(u)\frac{\sin^2(u/2)}{u/2}du \quad (\text{IV} - 19)$$

IV.3.3.3 Coupling factor determination

After the derivations of even mode impedance's equations, we can start the calculation by firstly choosing the design parameters given in Cristal and Young's table [CRI 66]. The selection criteria of these values are based on the bandwidth and ripple level desired. In our design, the bandwidth is from 2 to 20 GHz, which means the bandwidth ratio should be greater than Fmax /Fmin=10. To get a maximally-flat frequency response, the ripple level is needed to be as small as possible. We consider a ripple level of a fraction of dB.

Ripple level (dB)	Z_1	Z_2	Z_3	Z_4	Z_5	Bandwidth Ratio
0.20	1.02379	1.06452	1.14687	1.33341	2.21025	9.498
0.25	1.02764	1.07099	1.15622	1.34622	2.23285	10.256
0.30	1.03134	1.09697	1.16469	1.35771	2.25315	10.960

Table IV-2: The even mode impedance of the 9 sections tandem structure with the ripple level and the bandwidth ratio in Cristal and Young's table.

As given in the Table IV-2, the Z_n (n=1 to 5) is the ratio of the even mode characteristic impedance to the normalized impedance of 50 Ω for the five sections considered. Since the coupler is symmetric, the nine sections along the coupling path can be reduced to the five sections at only one side as described in Figure IV-8. According to the Table IV-2, for a bandwidth ratio of 10.256, the ripple level is 0.25 dB, which indicates an acceptable fluctuation on the coupling factor in the entire frequency band.

From the obtained impedance Z_n (n=1 to 5), one can derive the coupling function k(u) which returns the coupling coefficient of each coupling element along the length of the coupler. This coefficient, given by equation IV-20 [CRI 66], is illustrated in Figure IV-9.

$$k(u) = \frac{(Z_{oe}(u)/Z_o)^2 - 1}{(Z_{oe}(u)/Z_o)^2 + 1} \qquad (\text{IV} - 20)$$

It can be noted from the figure that the coupling is more pronounced at the cross section of the two coupled path, this one is identified as tight coupling. The coupling factor R decreases with the increased distance from the mid-section, this value tends to zero at the end of the length. This one is denoted as loose coupling. The coupling factor R in decibels is related to the corresponding section along the length of the coupler.

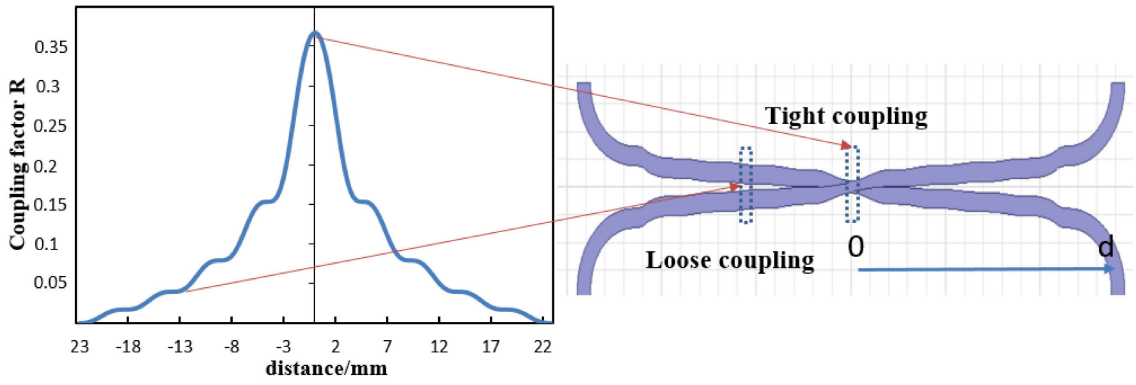

Figure IV-9: Coupling factor R along the length of the coupler.

With respect to the formulas given in previous equations (IV 14 - 20), a numerical algorithm developed in MATLAB™ environment is written to determine the coupling factor R along the length of the coupler. The following step is to figure out the physical dimensions of each coupling element on the basis of the coupling factor R. According to Figure IV-9, the coupling element are broadside coupled along the length of the coupler and form a cross section at the mid part. To realize this structure, one should apply the broadside-coupled offset stripline configuration. In the next section, the calculation of the design parameters of a broadside-coupled offset stripline are given.

IV.3.3.4 Broadside-coupled offset stripling configuration

In the broadside-coupled offset stripline configuration, the design parameters are the strip width W, the strip offset length W_o, the strip spacing S and the ground spacing distance L. The electrical parameters are the dielectric constant of the substrate (ε_r) and the even/odd mode impedances of each stripline element. The general offset stripline configuration is presented in Figure I-V10:

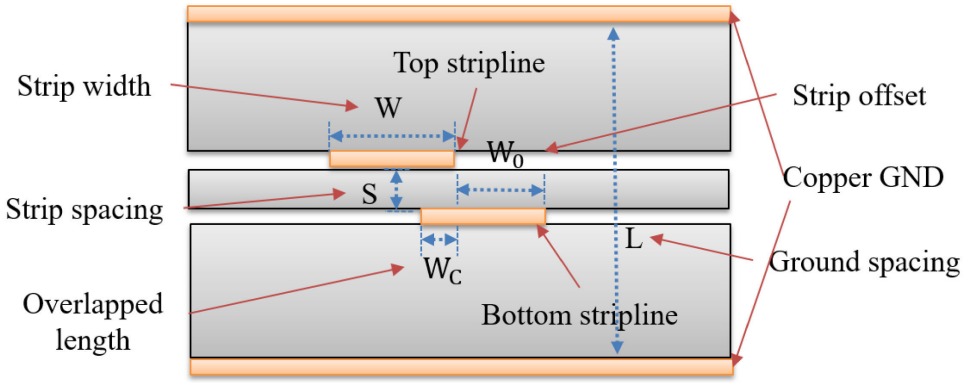

Figure IV-10: The offset stripline configuration.

Since the coupling factor versus distance function is already figured out by means of equations IV-20, the offset stripline dimensions (W, S, L and W_o) can be determined from the design equations proposed by J. Paul Shelton [SHE 66_b]. In this reference, the author demonstrates two types of coupling: a loose coupling at the two sides and a tight coupling at the mid part (cross section) as indicated in Figure IV-9. Indeed, these two types of coupling are mainly dependent on the relative position of the two broadside-coupled elements. To identify in which condition a tight/loose coupling should be applied, the capacitance between the two coupled elements should be analyzed. By means of the fringing capacitance derivation and the Schwartz-Christoffel transformation [SHE 66_b], these conditions are given thereafter:

Tight coupling conditions:

$$\frac{W'}{1-S'} \geq 0.35 \qquad (\text{IV}-21)$$

$$\frac{Wc'}{S'} \geq 0.7$$

Loose coupling conditions:

$$\frac{W'}{1-S'} \geq 0.35$$
$$\frac{2 * W_o{}'}{1+S'} \geq 0.85 \qquad (\text{IV}-22)$$

Where W'=W/L, S'=S/L, W_c'=W_c/L and W_o'=W_o/L. These symbols denote the normalized values. Once the coupling condition is identified, according to the equations provided in [SHE 66_b], the design parameters of the stripline including the space width W, stripline offset distance W_o, strip spacing S and the overlapped length W_c can be calculated using the MATLAB™.

IV.3.4 Structure improvement in terms of insertion loss and isolation

A multi-section topology based coupler can operate in a broad frequency band. For example, a frequency band spanning from 0.5 to 18 GHz has been demonstrated in the reference [ANS 14]. With such a large frequency band, poor matching properties and reduced directivity due to the abrupt change between each section along the transmission line represent a major issue. To avoid these drawbacks, a modified structure is described in this section.

IV.3.4.1 Reduction of the insertion loss

The main limitation of the tandem structure is related to the transition aspect between each successive section along the coupled path which impacts the matching properties. In order to improve the matching property, the horizontal distance between each two adjacent coupled elements should be reduced as much as possible. Thus, the number of discrete points should be theoretically infinite. However, based on the concern of the design complexity, this number is chosen to be 400 as a compromise. Thus, based on equations

given in the previous section, a numerical program is written in MATLAB™ to represent the nearly continuous coupled line from 400 discrete segments.

As demonstrated in the Figure IV-11, a tandem structure with a large number of sections allows the reduction of the discontinuity. In the example given, a 5 sections tandem structure is compared to a 400 sections one. It is obviously found that the discontinuity between each coupled element is further reduced by increasing the discretization number of elements along the coupled path.

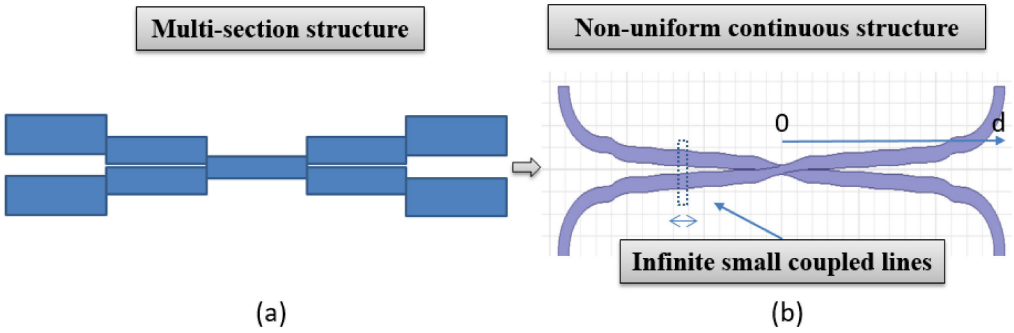

Figure IV-11: Transition aspect between each two successive sections of a tandem structure of (a) 5 sections (b) 400 sections.

Although this discretization method can be easily applied to the two sides of the coupled lines, it is more difficult in case of the middle part (cross section of the two coupled lines) since the discontinuity at this location is more important as demonstrated in Figure IV-12.a. To smooth such discontinuity, different types of compensation methods are shown in Figure IV-12 and simulated in HFSS™ environment. The simulation results for these different kinds of compensation methods are compared thereafter.

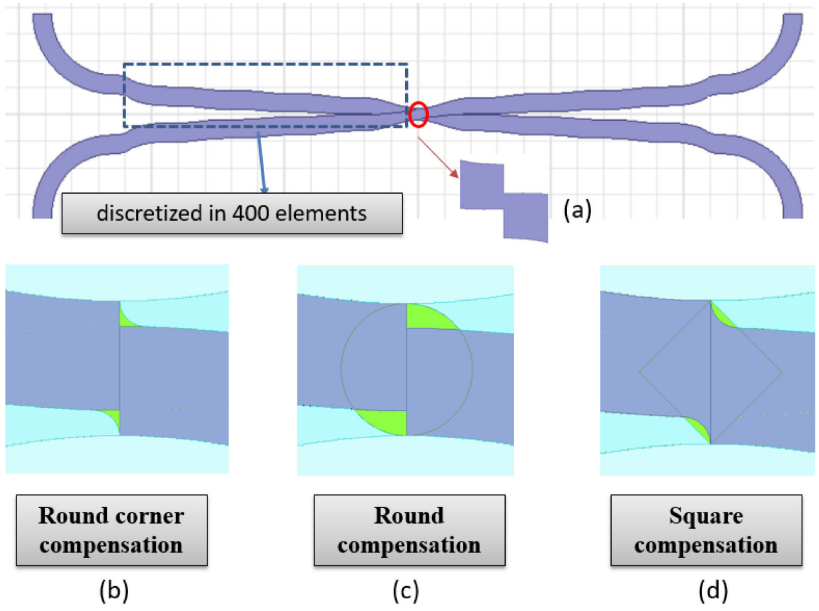

Figure IV-12: The insertion loss compensation method in the mid cross section. (a) Original section (b) Round corner compensation (c) Round compensation (d) Square compensation.

IV.3.4.1.1 Round corner compensation

As demonstrated in the previous section, the proposed 3 dB coupler is composed of two 8.34 dB couplers whose properties determine directly the performance of our design. Based on the simulation complexity consideration, the simulation of a 8.34 dB multi-section coupler with tandem structure is first achieved by considering a round corner compensation method. Figure IV-13 shows the simulation results in such case.

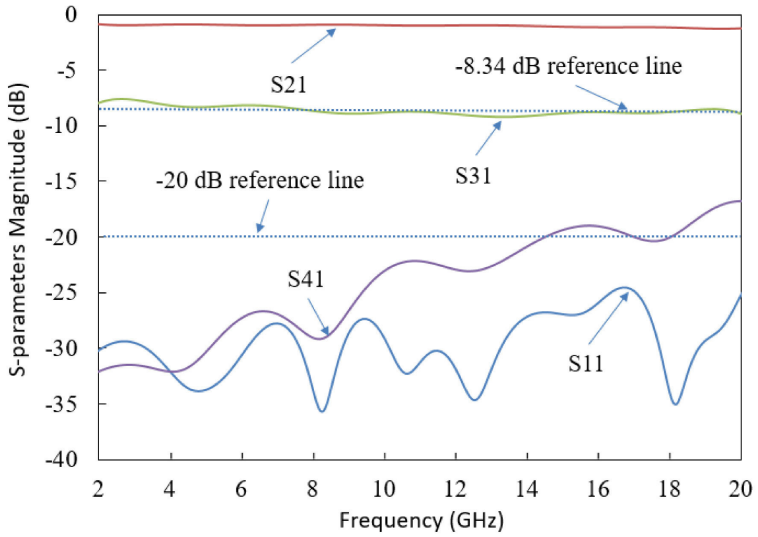

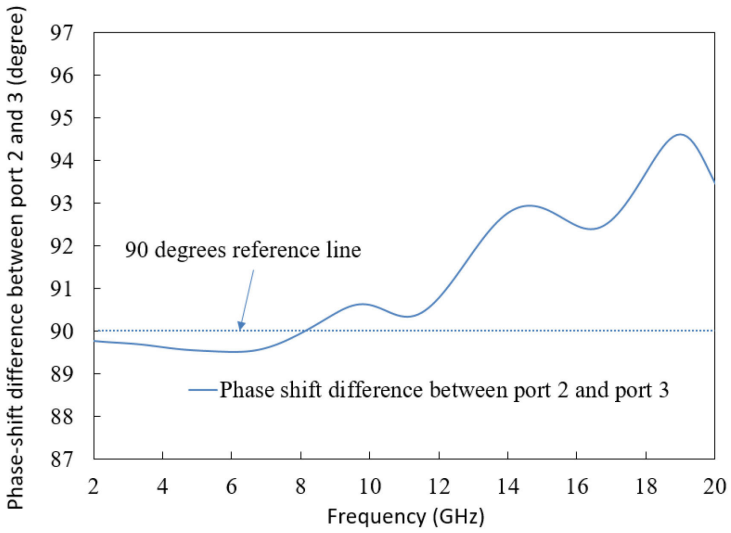

Figure IV-13: S-parameters simulation results when the round corner compensation method is applied in the middle cross section for a 8.34 dB multi-section coupler (a) S-parameters magnitude (b) Phase shift difference between the output port 2 and coupling port 3.

In the entire bandwidth ranging from 2 to 20 GHz, the S-parameters simulation results show a good coupling around -8.3 dB, a reflection coefficient below -25 dB, an isolation performance better than 17 dB and a phase shift of 90 ± 5° between the output port 2 and the coupling port 3.

IV.3.4.1.2 Round compensation

In this part, the round compensation method is tested. The simulation results are given in the Figure IV-14.

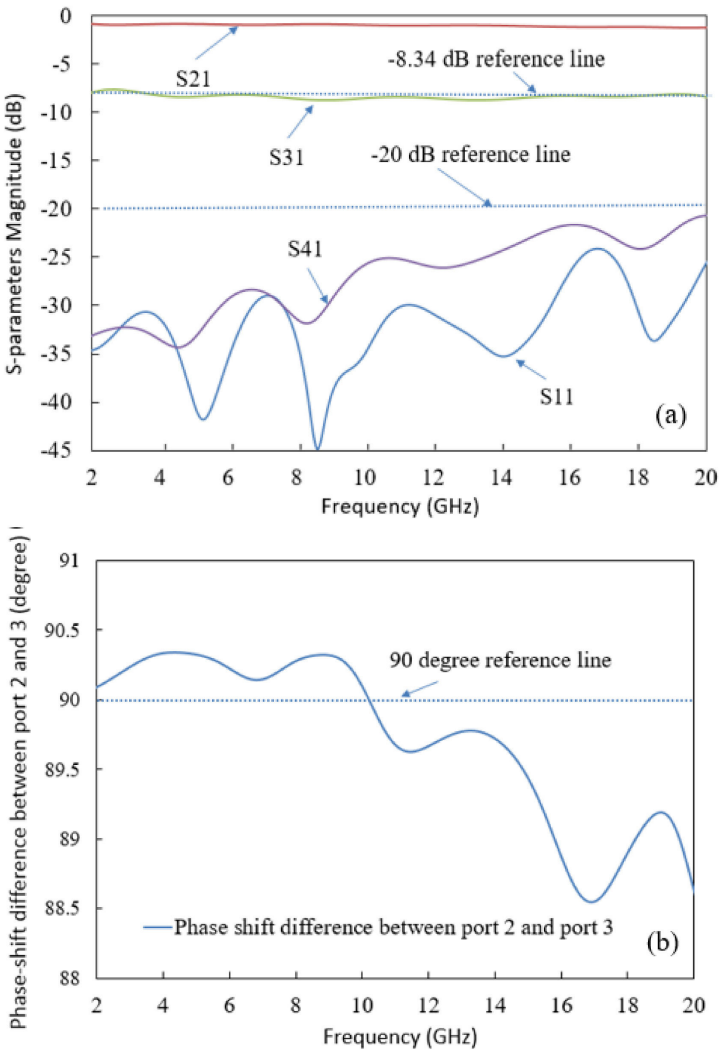

Figure IV-14: S-parameters simulation results when the round compensation method is applied in the middle cross section for a 8.34 dB multi-section coupler (a) S-parameters magnitude (b) Phase shift difference between the output port 2 and coupling port 3.

Over the entire frequency band, the S-parameters simulation results show a good coupling around -8.3 dB. The reflection coefficient is always below to -24 dB, an isolation performance better than 21 dB and a phase shift of 90 ± 1° between the output port 2 and the coupling port 3.Compared to the round corner method, the round one gives a better performance.

IV.3.4.1.3 Square compensation

In this section, the third compensation method: square compensation is simulated and the results are presented in Figure IV-15:

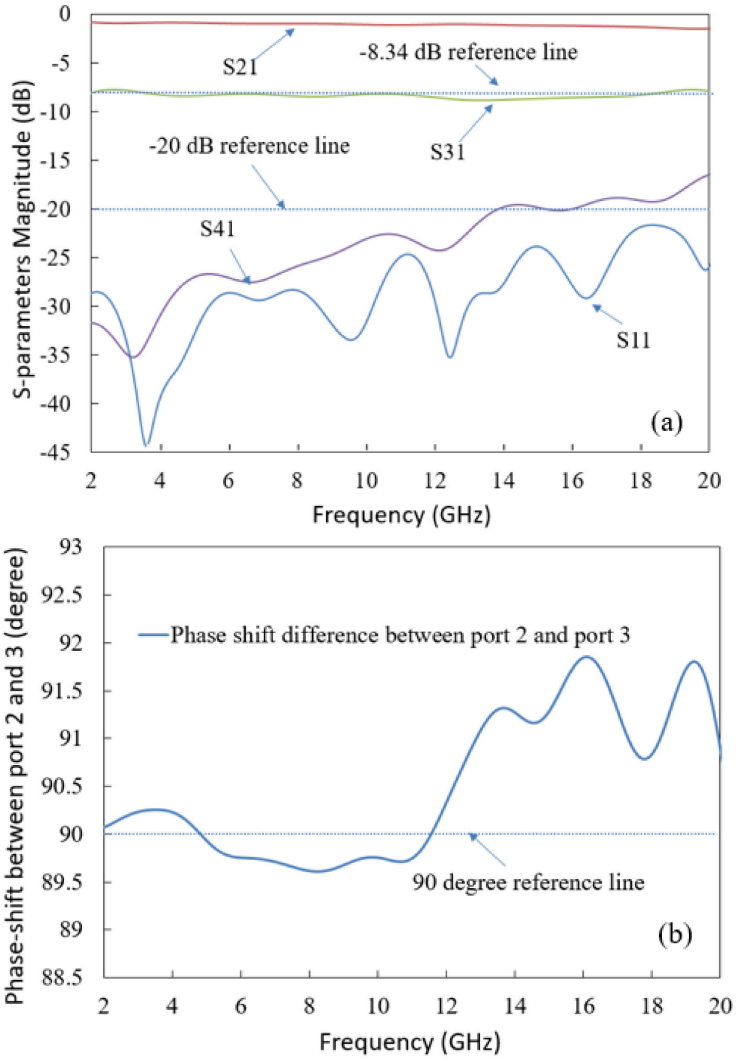

Figure IV-15: S-parameters simulation results when the square compensation method is applied in the middle cross section for a 8.34 dB multi-section coupler (a) S-parameters magnitude (b) Phase shift.

According to the Figure IV-15, the S-parameters simulation results show a good coupling around -8.3 dB in the desired frequency band. The reflection coefficient is always below -22 dB and an isolation performance better than 17 dB. The phase shift between the output port 2 and the coupling port 3 is around 90 ± 2°.

To sum up the compensation methods proposed above, their simulation results are gathered in the Table.IV-3:

Compensation method	Matching property	Coupling	Isolation	Phase shift
Round corner	-22 dB	-8.3 dB	-17 dB	90 ± 5°
Round	-24 dB	-8.3 dB	-21 dB	90 ± 1°
Square	-22 dB	-8.3 dB	-17 dB	90 ± 2°

Table IV-3: The comparison of simulation results for different compensation methods.

According to these results, the round compensation method is selected to ensure a good matching better than -24 dB at each port, a good isolation better than 21 dB and an almost constant phase shift of 90° between port 2 and port 3.

IV.3.4.2 Isolation improvement

In the previous part, it has been shown that the round compensation method to enhance the matching property leaves an isolation performance around -20 dB. As indicated in the reference [OBO 14], the isolation performance mainly depends on the velocity difference between the even and odd modes propagation. Thus, for a better isolation performance, an air gap is positioned between each crossover of the parallel-coupled lines to equilibrate the even/odd modes propagation velocity. As illustrated in Figure IV-16, at the cross section part, the odd mode is located between the two stripline (127 µm) and the even mode one (508 µm) is between the top/bottom stripline and the copper GND. Because the dielectric constant of air ($\varepsilon_r = 1$) is less than the one of the substrate ($\varepsilon_r = 2.2$), the air hole can efficiently accelerate the odd mode propagation velocity to enhance the isolation performance at high frequency.

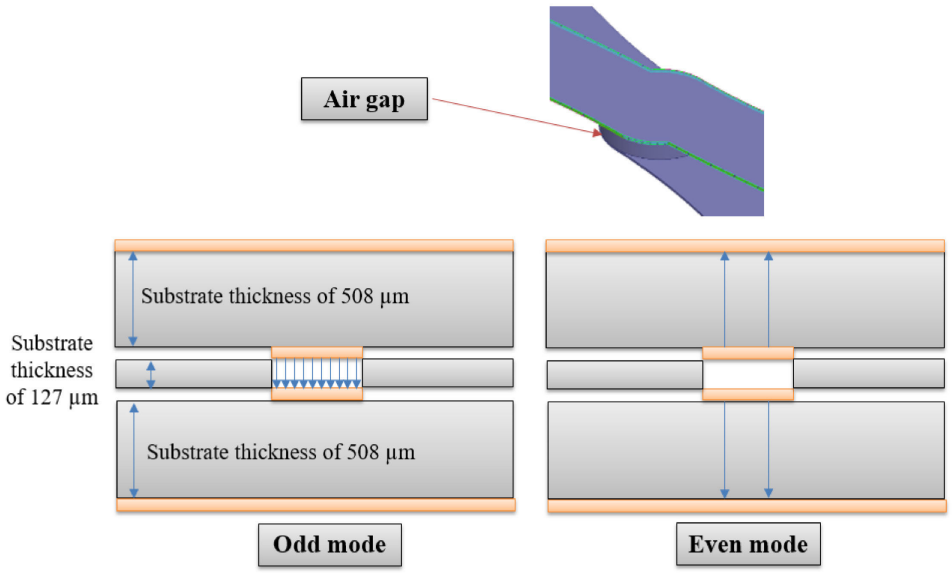

Figure IV-16: The air gap placed between each crossover of the parallel-coupled lines and the even/odd mode propagation path.

The isolation improvement is tested in the HFSS™ environment and the simulation results are given in Figure IV-17:

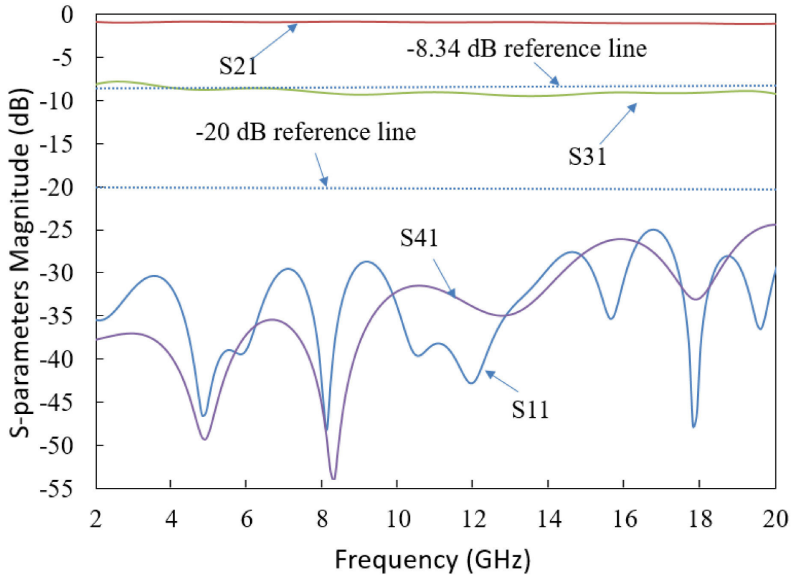

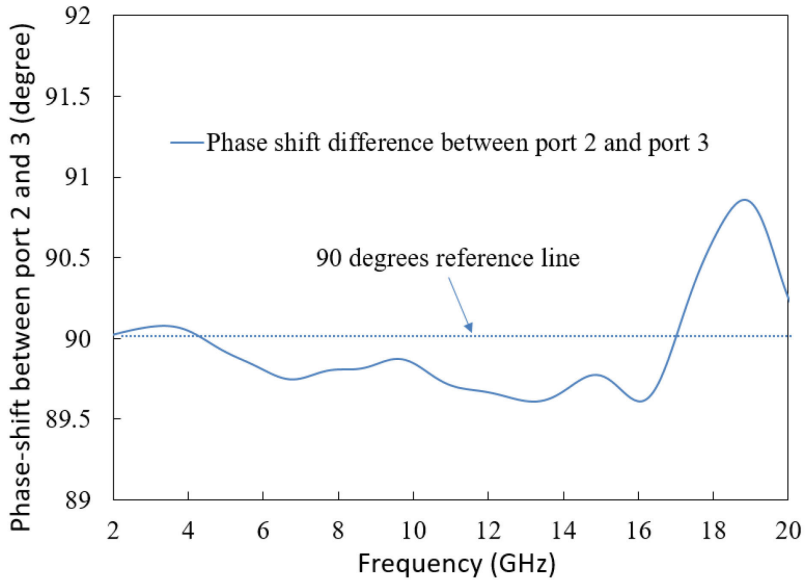

Figure IV-17: S-parameters simulation results when the isolation improvement method is applied in the middle cross section for a 8.34 dB multi-section coupler (a) S-parameters magnitude (b) Phase shift between the output port 2 and coupling port 3.

With the simulation results given above, it is observed that this air gap inserted in between the cross section of two coupled lines can effectively improve the isolation performance from 20 dB to 25 dB, especially at the high frequencies. The phase shift between the output port 2 and the coupling port 3 is around 90 ± 1°.

This method evaluated in this section gives an isolation improvement of around 7 dB at 20 GHz. In the following part, the design of the proposed coupler is given in details.

IV.3.5 Design of the proposed coupler

In the previous section, the isolation improvement method as well as the insertion loss reduction technique are evaluated in order to improve the performance of the proposed coupler. As explained in IV.3.2.1, a 3 dB coupler can be realized by cascading two 8.34 dB coupler. Therefore, to evaluate the performance of a 3 dB coupler, the designed structure is simulated and presented in Figure IV-18. In this structure, two 8.34 dB couplers C_1 and C_2 are cascaded to realize the 3 dB coupling. Two layers of copper at the top and bottom are considered as ground plane. This configuration is also illustrated in Figure IV-10, where the multi-layer (three layers) structure is given. As previously discussed, an air

hole is inserted into the cross section to enhance the isolation performance. In addition, several holes are drilled to help to align the different layers which are fixed with screws.

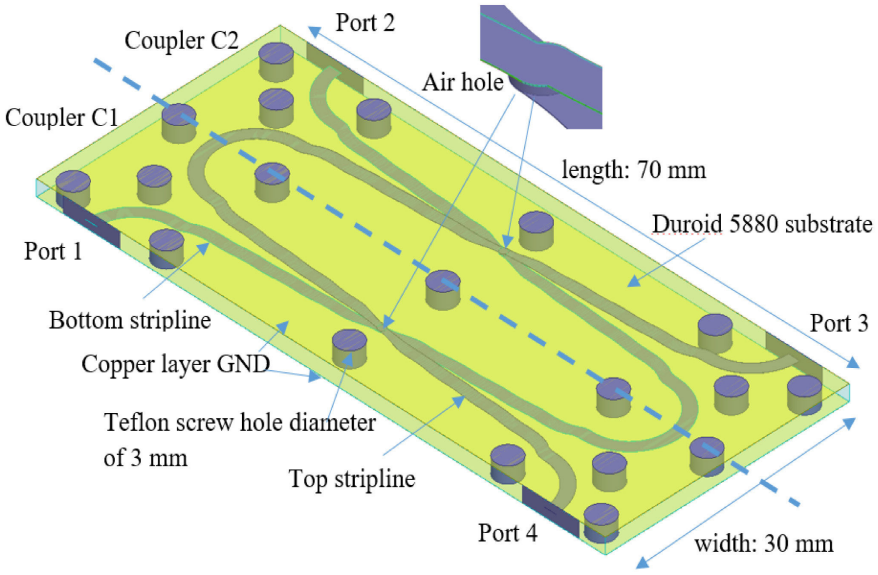

Figure IV-18: Structure of the 3 dB coupler based on the cascade of two 8.34 dB couplers.

To protect the circuit and ensure the connection reliability, a metal package is also fabricated (Figure IV-19). The screw holes and the connectors space are carefully designed to fix the coupler into the package and ensure the alignment of the three layers.

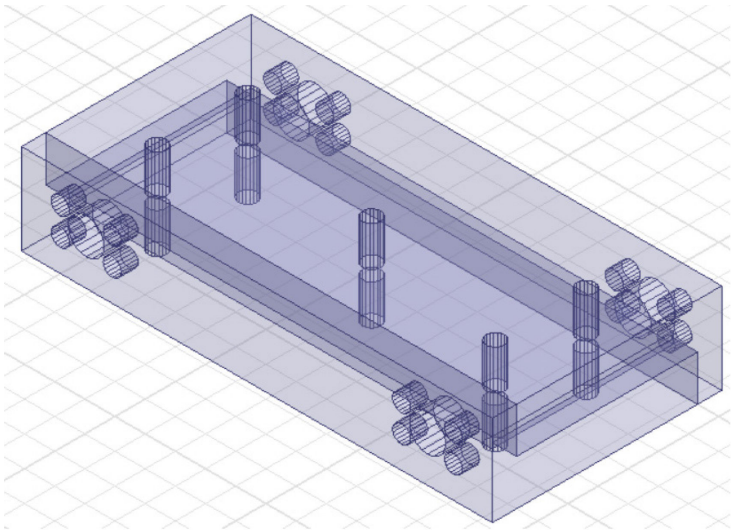

Figure IV-19: The 3D design of the packaging to fix the coupler circuit.

The fabrication of the coupler and the results obtained for both simulation and measurement are presented in the following part.

IV.3.6 Fabrication of a 3 dB multi-layer coupler

A photograph of the fabricated multi-layer coupler is given in Figure IV-20. The substrate used for the realization is the Rogers RT/Duroid 5880 ($\varepsilon_r = 2.2$, tan δ = 0.0009). For the multi-layer structure, the spacing S (Figure IV-10) is extremely important since it mainly determines the coupling factor. To avoid increasing this spacing, a special connector named SMA-KFD469 is used. Thanks to its tapered tip, the connection in between the layers can be realized.

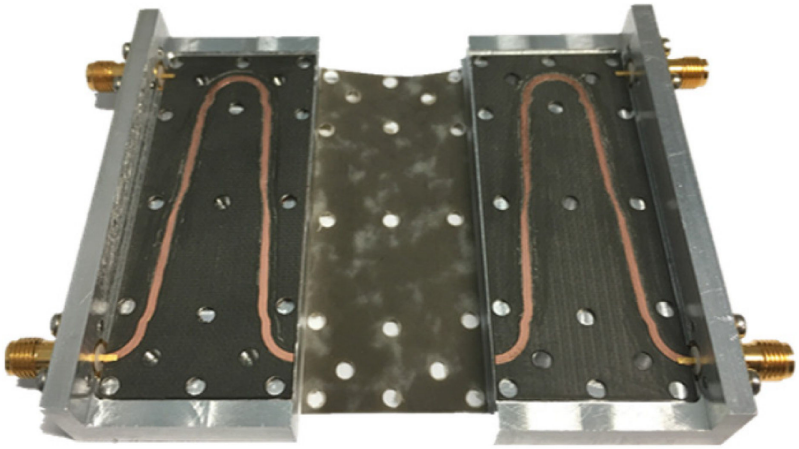

(a) (b) (c)

Figure IV-20: Photograph of the fabricated multi-layer coupler (a) Bottom stripline (b) Duroid 5880 mid layer (c) Top stripline.

The three parts of the coupler shown on the exploded view in Figure IV-20 are stacked using screws. In particular, attention should be paid to the alignment of the striplines on the top and bottom layers. This is achieved by ensuring the same position of the screws holes drilled on each substrate. The thickness of top and bottom substrates (Figure IV-20.a and Figure IV-20.c) is equal to 508 µm while the mid substrate thickness (Figure IV-20.b) is 127 µm. The etching is realized by using a PCB milling system with a good precision (± 10 µm) to enhance the coupler's performance over the entire frequency band from 2 to 20 GHz.

IV.3.7 Characterization of the 3 dB multi-layer coupler

To appreciate the performance of the proposed coupler the simulation and measurement results are compared in Figure IV-21.

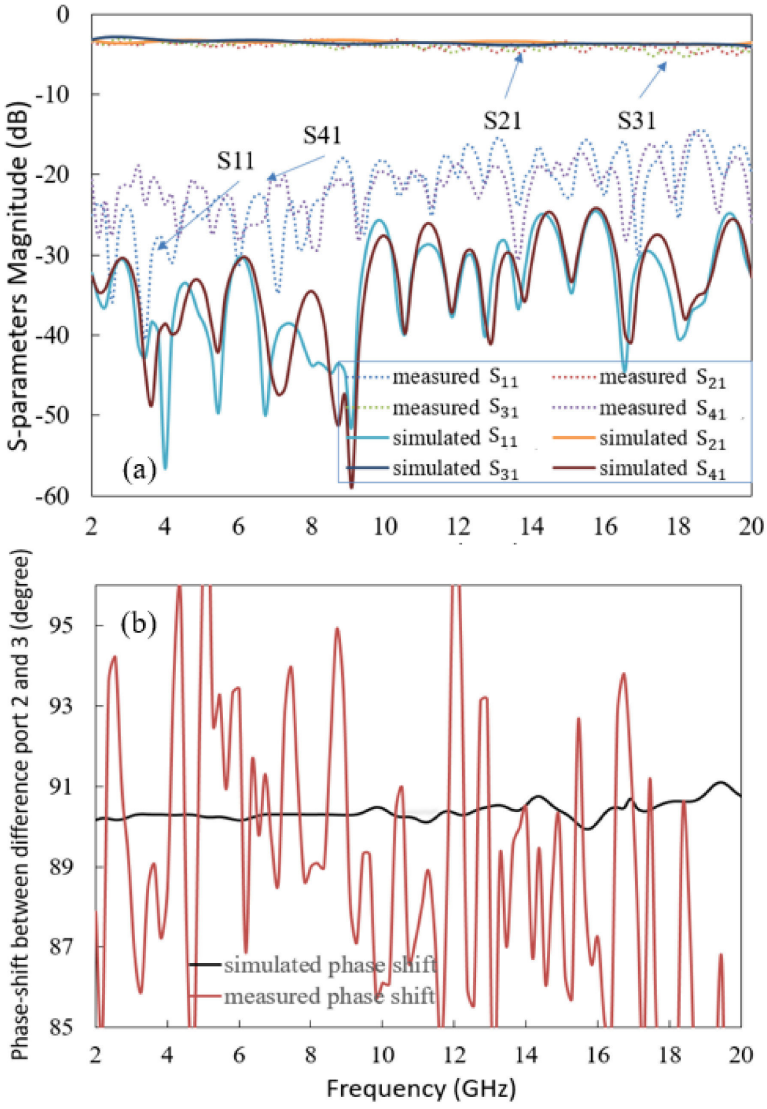

Figure IV-21: Simulated and measured S-parameters as a function of frequency (a) Magnitude (b) Phase-shift between port 2 and port 3.

The realized coupler demonstrates a good agreement between measurement and simulation data for both the coupling (S_{31}) and transmission (S_{21}) coefficients. Actually, values around 3.5 ± 0.5 dB between 2 GHz and 15 GHz and around 4.3 ± 0.5 dB from 15

GHz to 20 GHz are measured, which is very good for such a large frequency band. The isolation (S_{41}) as well as the matching properties (S_{11}) are always better than 17 dB. The phase shift between port 2 and port 3 is mainly in the range of 90 ± 5° (Figure IV-21.b).

According to these results, the coupler is proved to be an excellent candidate for the construction of the six-port reflectometer. Nevertheless, to link the five multi-layer couplers together, a via-hole is necessary as the striplines on different layers should be connected to each other at the electrical path between the couplers Q_4 and Q_5 (Figure IV-3). In particular, this electrical path should be the same to the one between the couplers Q_3 and Q_5 to avoid the phase imbalance at the output ports. Hence, a controlled impedance has to be carefully designed with minimum insertion loss and phase shift.

IV.3.8 Conclusion

In this section, the coupler selection strategy is firstly given. After that, the multi-section coupler as well as the applied tandem configuration is theoretically discussed in order to cover a large working frequency (2 - 20 GHz). With a carefully derivation of the even mode impedance, a multi-section coupler can be therefore obtained by using the broadside-coupled offset stripling configuration. Facing to a high insertion loss and poor isolation features, the structure improvement techniques are carried out and evaluated by the HFSS™ simulation. Thanks to this design tool, the design of the 3 dB multi-layer coupler is finished. After the fabrication, it is characterized and the obtained measurement results show that the proposed coupler is a good candidate for the design of a broadband six-port reflectometer.

IV.4 Controlled impedance via design

In this section, the design of a controlled impedance via is discussed. In fact, the insertion loss as well as the phase shift increases with the thickness of the via. Thus, the feasibility of the structure in terms of transmission coefficient and phase shift compared to

a standard stripline is under investigation. Based on the description in [WEI 15], the simulation design and fabricated structure are given in the Figure IV-22.

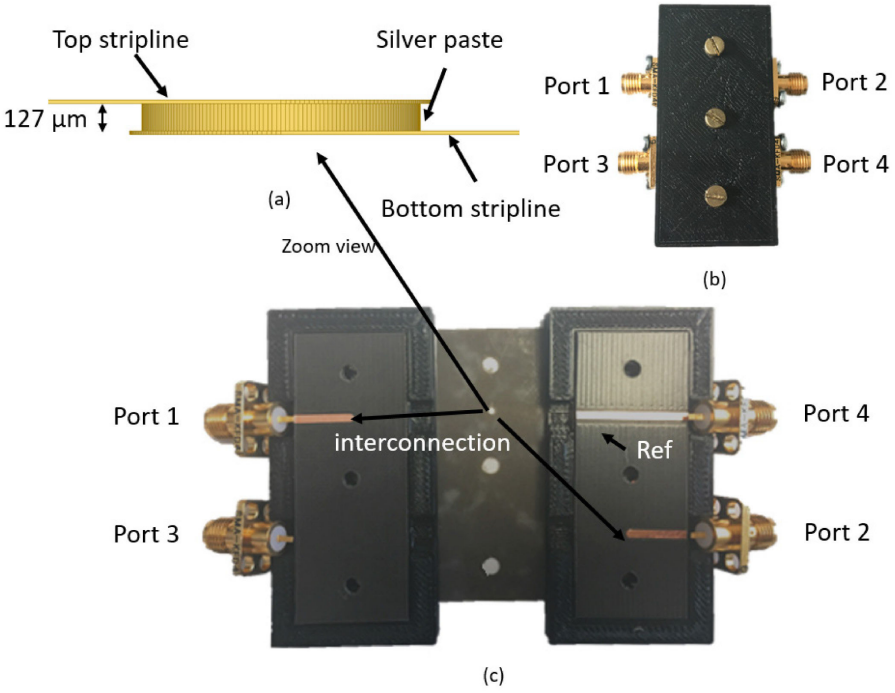

Figure IV-22: (a) Controlled impedance via design (b) Closed package of the interconnection structure and its corresponding reference line (c) Exploded view of the test.

To connect the two striplines on top and bottom layers, a cylinder, with a diameter of 1.3 mm and a height of 127 µm (mid layer thickness), is used as the controlled impedance via as indicated in the Figure IV-22.a. The whole structure is simulated using HFSS™ to evaluate its performance in terms of transmission coefficient and phase shift in the frequency band of interest.

This interconnection is realized by adding some conductive silver paste through the drilled hole at the mid layer. The diameter of the drilled hole (1.3 mm) is slightly smaller than the stripline width (1.41 mm), which helps to be entirely covered by the two striplines without any leakage. After a heating of 20 min, the interconnection becomes solid and is characterized through S-parameters measurement.

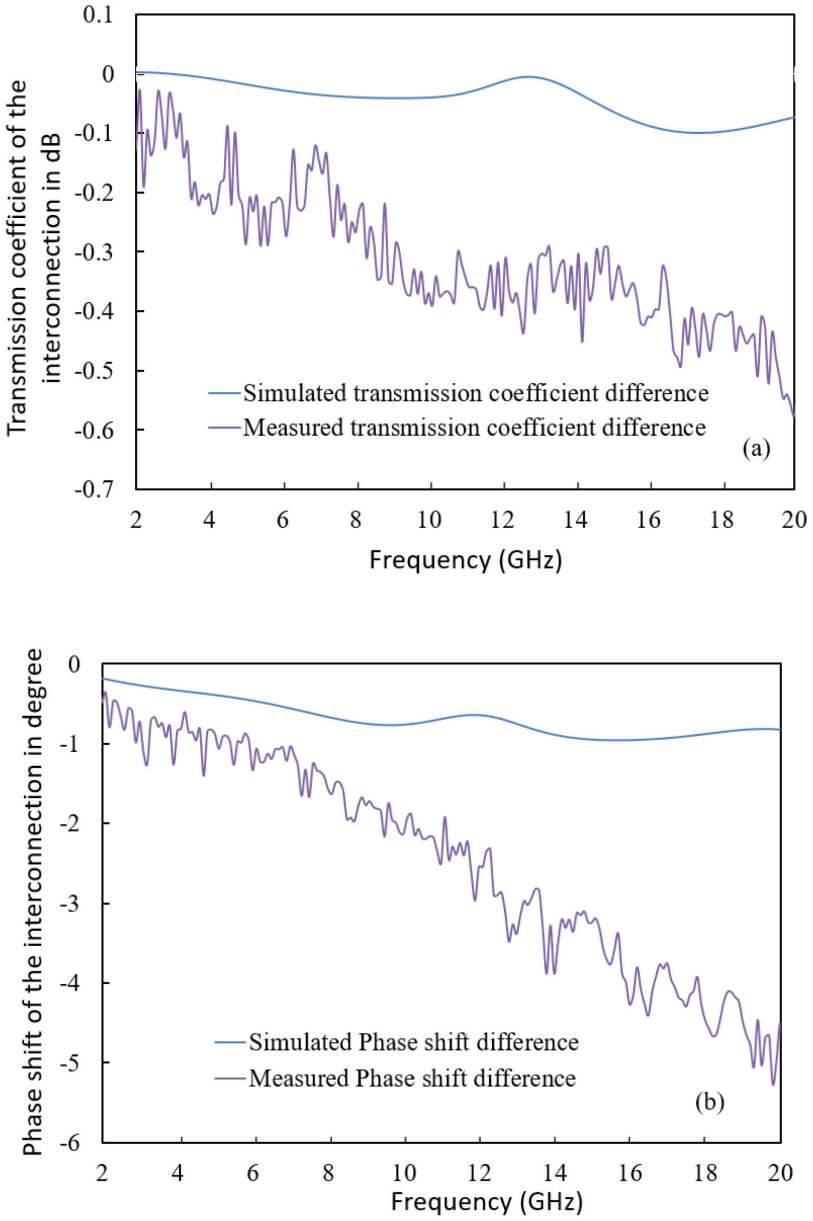

Figure IV-23: Simulated and measured transmission coefficient of the interconnection as a function of frequency compared to the reference line transmission coefficient. (a) Transmission coefficient difference (b) Phase-shift difference.

In Figure IV-23, are given the transmission coefficients of the simulated and measured data for the controlled impedance via compared to a reference line. The simulated results show a difference between the via and the reference line around 0.1 dB for the magnitude on the frequency band of interest. On the measured data side, a maximum difference between the via and the reference line of about 0.5 dB is retrieved (Figure IV-23.a). In the Figure IV-23.b, it is observed that, the phase shift difference between the two lines

(controlled impedance via and reference line) is more pronounced as a function of the frequency. One can notice that the simulated phase shift difference is lower than 1 degree while the measured one remains below 5 degrees over the entire working frequency band.

After this first step which consisted to study individually the coupler and the controlled impedance via, the six-port reflectometer can be simulated to better predict its performance.

IV.5 Design of a six-port reflectometer based on five 3 dB couplers

IV.5.1 Introduction

In the previous two sections, the proposed broadband 3 dB coupler as well as the controlled impedance tuner prove that they are good candidates for their implementation in the six-port reflectometer. Thus, in this section, the design of the six-port reflectometer is presented and evaluated by the simulation approach.

IV.5.2 Simulation of the six-port reflectometer

The previous simulation and measurement results prove that the coupler and the controlled impedance via structure investigated are good candidates for their implementation in the six-port reflectometer. Hence, according to the topology given in Figure IV-3, five 3 dB multi-layer couplers and a controlled impedance via are associated to realize the six-port reflectometer presented in the Figure IV-24.

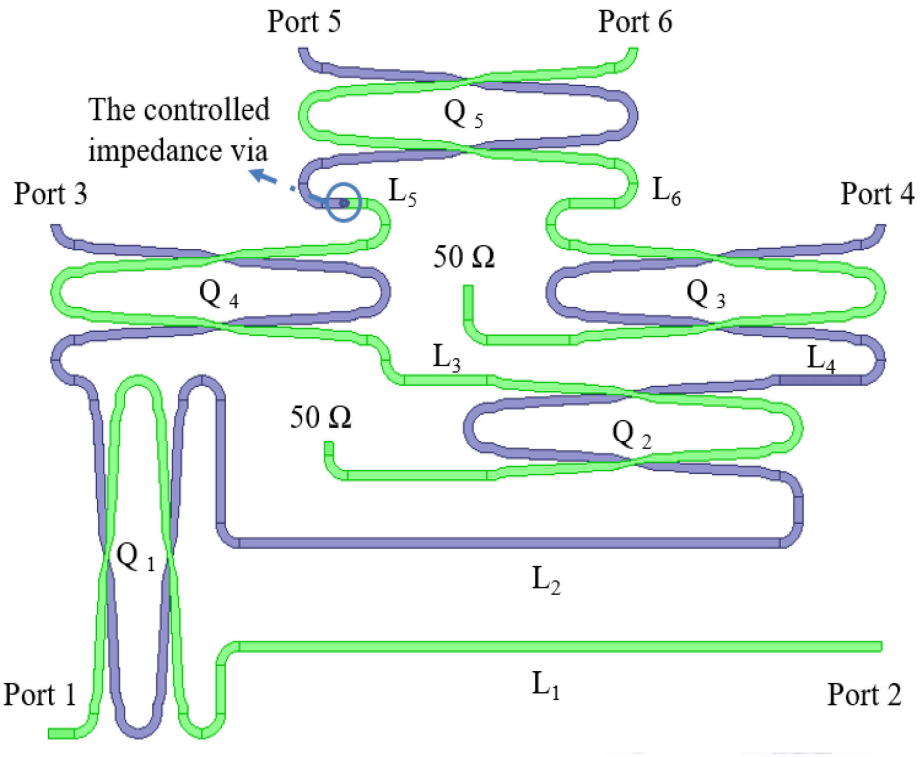

Figure IV-24: Six-port reflectometer layout based on five couplers and a controlled impedance via (The layout size is 13 cm*10 cm).

In this layout, for better illustration, the striplines on the top layer are in green while the ones on the bottom layer are in purple. The signal feeding the port 1 is splited by the coupler Q_1 and a part goes to the device under test connected to the port 2 and the other part goes towards the couplers Q_2 to Q_5. To make sure the phase difference between port 3 and port 4 is 180° (Figure I-3) and remains the same at the entrances of the coupler Q_5, the electrical paths connecting the five couplers must satisfy the following equations:

$$L_1 = L_2\ ;\ L_3 = L_4\ ;\ L_5 = L_6 \qquad (IV-23)$$

To better predict the performance of the six-port reflectometer, we consider for the simulation by means of the KEYSIGHT/ADS™ the data measured for the coupler and the interconnection instead of ideal values. Thanks to the reflection coefficient Γ derived from the equation IV-6, the performance of the six-port reflectometer is estimated on the basis of the simulation results.

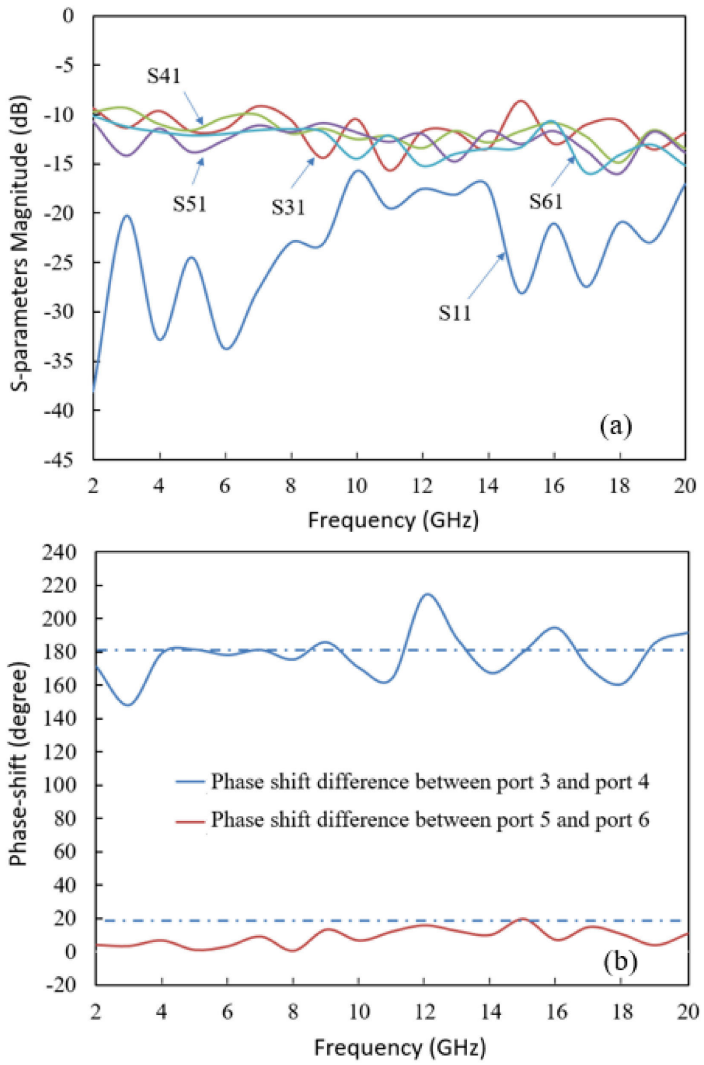

Figure IV-25: Six-port reflectometer simulation results as a function of frequency (a) Magnitude of S-parameters at each port (b) Phase-shift difference between port 5 ,port 6 and port 3, port 4.

In Figure IV-25 are given the simulation results of the six-port reflectometer as a function of the frequency. From the conceptual diagram given in Figure IV-3, when the source is connected at port 1 and the device under test at port 2 is a perfect 50 Ohm load, the signal level detected at the other ports should be equal to -9 dB. The simulation results demonstrate rather -13 dB on almost the entire frequency band. Compared to the ideal -9 dB performance, the magnitude difference is mainly caused by the imperfection of the coupler in terms of transmission coefficient and coupling factor (3.5 ± 0.5 dB). Indeed, the signal feeding the input port goes through 3 couplers to reach the output port. As predicted

by the theory, the phase shift between port 3 and port 4 should exhibit a difference around 180° compared to the one observed between port 5 and port 6. One can note from the Figure IV-25.b, at several frequency points, this phase shift is not constant and varies between a maximal value of 220° and a minimal value of 150°.

The simulated results show good performance of the six-port reflectometer at most frequency points in the entire frequency band. However, imperfections of the system still occur at several frequencies. In order to reduce the influence of these effects and improve the measurement accuracy, a calibration method is introduced in the next section.

IV.5.3 Calibration method

For a six-port reflectometer, only one-port devices are measured. A basic scheme of this operation is given in Figure IV-26 [RYT 01].

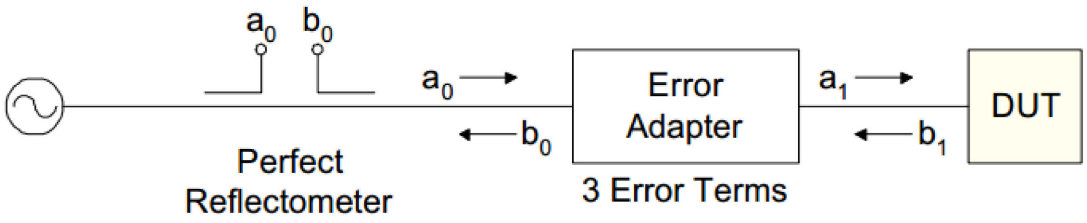

Figure IV-26: One port 3-terms error model [RYT 01].

In the Figure IV-26, first of all, the six-port reflectometer is considered as a perfect system. The imperfections of the system including the directivity, port match and tracking errors are represented by an error adapter which is inserted between the reflectometer considered as perfect and the DUT.

The error adapter is analyzed in details with the help of a flowgraph showing all the possible signal paths in Figure IV-27. The three terms of errors are identified as e_{00} (directivity error), e_{11} (port match error) and $e_{10}e_{01}$ (tracking error).

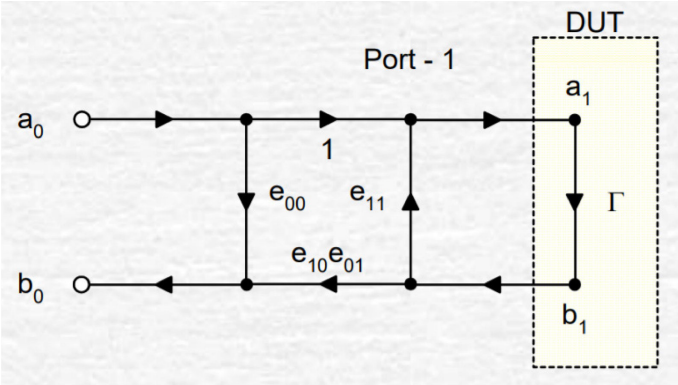

Figure IV-27: The flowgraph shows all the possible signal paths.

The measured reflection coefficient Γ_m as a function of the actual reflection coefficient Γ obtained from the flowgraph is:

$$\Gamma_m = \frac{b_0}{a_0} = \frac{e_{00} - \Delta_e \Gamma}{1 - e_{11}\Gamma} \qquad (IV - 24)$$

If we invert the formula to obtain the actual reflection coefficient, we have:

$$\Gamma = \frac{e_{00} - \Gamma_m}{\Delta_e - e_{11}\Gamma_m}$$

$$\text{where} \qquad \Delta_e = e_{00}e_{11} - e_{10}e_{01} \qquad (IV - 25)$$

The equation can be transformed into a linear form to simplify the calculation:

$$\Gamma_{mn} = e_{00} + \Gamma_n \Gamma_{mn} e_{11} - \Gamma_n \Delta_e \qquad (IV - 26)$$

Where n is the number of the known loads needed to solve the problem. Thus, the equations set to calculate the three terms of errors (e_{00}, e_{11} and $e_{10}e_{01}$) are given by:

$$\Gamma_{m1} = e_{00} + \Gamma_1 \Gamma_{m1} e_{11} - \Gamma_1 \Delta_e$$

$$\Gamma_{m2} = e_{00} + \Gamma_2 \Gamma_{m2} e_{11} - \Gamma_2 \Delta_e \qquad (IV - 27)$$

$$\Gamma_{m3} = e_{00} + \Gamma_3\Gamma_{m3}e_{11} - \Gamma_3\Delta_e$$

With the three different known reflection coefficients Γ_n and the measured reflection coefficientsΓ_{mn}, the linear equations above can be solved to determine e_{00}, e_{11} and $e_{10}e_{01}$.

$$e_{11} = \frac{\frac{(\Gamma_{m1} - \Gamma_{m3}) + (\Gamma_1 - \Gamma_3)}{T}(\Gamma_1 - \Gamma_2) + (\Gamma_{m1} - \Gamma_{m2})}{(\Gamma_1\Gamma_{m1} - \Gamma_2\Gamma_{m2})}$$

$$e_{00} = \Gamma_{m1} + \Gamma_1\Delta_e - \Gamma_1\Gamma_{m1}e_{11}$$

$$e_{10}e_{01} = (\Gamma_{m1} + \Gamma_1\Delta_e - \Gamma_1\Gamma_{m1}e_{11})\, e_{11} - \frac{(\Gamma_{m1} - \Gamma_{m3}) + (\Gamma_1 - \Gamma_3)}{T} \quad (IV-28)$$

$$\text{where} \quad \Delta_e = \frac{(\Gamma_{m1} - \Gamma_{m3}) + (\Gamma_1 - \Gamma_3)}{T}$$

$$\text{and} \quad T = \frac{[(\Gamma_1 - \Gamma_2) + (\Gamma_{m1} - \Gamma_{m2})](\Gamma_1\Gamma_{m1} - \Gamma_3\Gamma_{m3})}{(\Gamma_1\Gamma_{m1} - \Gamma_2\Gamma_{m2})}$$

Once the three terms of errors are determined, we can use them to calculate the calibrated reflection coefficient of an un-known load from the measured reflection coefficient:

$$\Gamma_{unknown} = \frac{e_{00} - \Gamma_m}{\Delta_e - \Gamma_m e_{11}} \quad (IV-29)$$

For demonstration, a study where the 2-20 GHz coupler based reflectometer benefits from a SOL (short, open and load) calibration is given. For the simulation, the port 2 of the six-port reflectometer is successively connected to a short, an open and a load to calculate their reflection coefficients. After recording these data for each frequency point from 2 to 20 GHz with an interval of 1 GHz, and knowing the actual values for the reflection

coefficient of these devices (respectively -1, 1 and 0), the three terms of error are easily calculated with the equations given above.

To directly observe the performance of the SOL one-port calibration, the smith chart is a good tool. Actually, the representation of the reflection coefficient before and after the correction allows an appreciation of the correction efficiency. Since our six-port reflectometer works in an ultra large frequency band [2- 20 GHz], we choose three frequency points 2 GHz, 11 GHz and 20 GHz respectively the start, center and stop of the frequency band of interest to represent its performance and the calibration accuracy. For demonstration, three loads, which represent different areas of the Smith Chart (around 50 Ohm, a short and a value in between) have been characterized by using the proposed reflectometer.

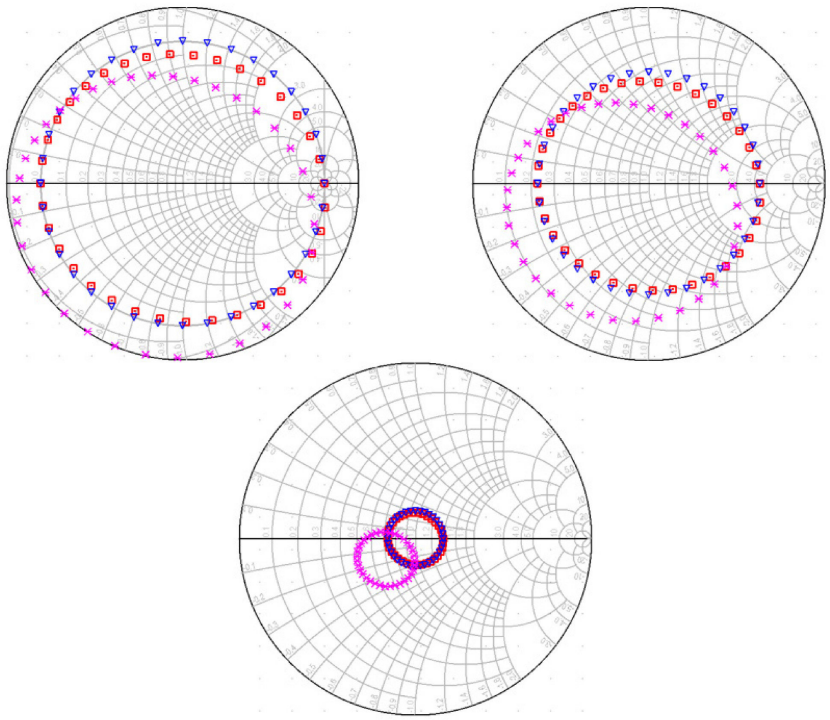

Figure IV-28: The Reflection coefficient distribution for three loads (a short, around 50 Ohm and a value in between) simulation pink star: measured data, red square: calibrated data and blue triangles: ideal data. F=2 GHz.

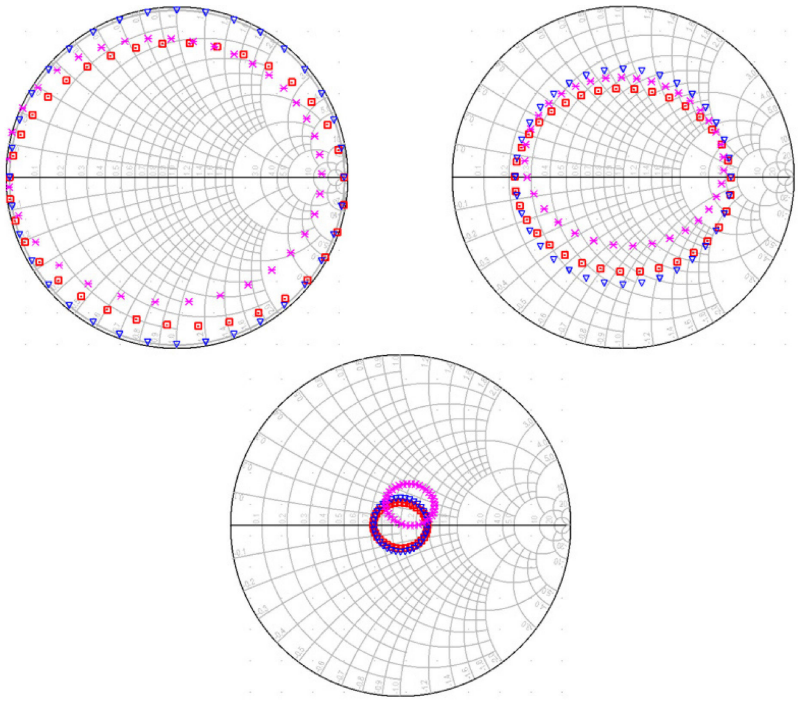

Figure IV-29: The Reflection coefficient distribution for three loads (a short, around 50 Ohm and a value in between) simulation pink star: measured data, red square: calibrated data and blue triangles: ideal data. F=11 GHz.

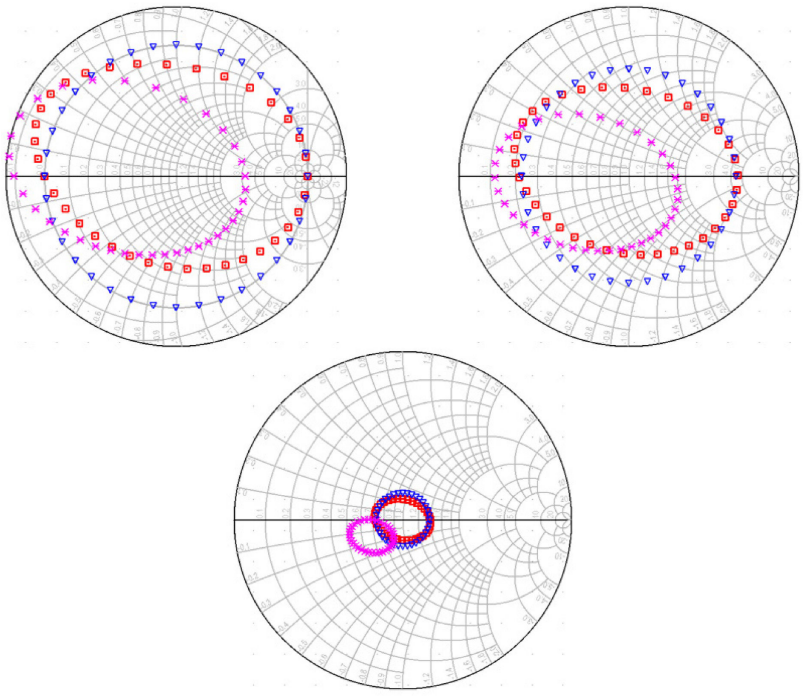

Figure IV-30: The Reflection coefficient distribution for three loads (a short, around 50 Ohm and a value in between) simulation pink star: measured data, red square: calibrated data and blue triangles: ideal data. F=20 GHz.

In these figures above (Figure IV-28, 29, 30), we give the distribution of the simulated reflection coefficients at three frequency points for ideal values (blue triangles), simulated values (pink star) and calibrated values (red square), respectively.

Generally speaking, a good agreement is observed between the ideal values and the simulated data retrieved after calibration.

IV.5.4 Conclusion

In this section a 2-20 GHz six-port reflectometer is presented. The key components of this system, a coupler based on a non-uniform structure and a controlled impedance via have been investigated in details, designed, simulated, fabricated and measured. The comparison between the simulation and measurement results shows a good agreement is obtained. Thanks to the very good performance obtained, these two components have been integrated in a six-port reflectometer. The characterization of a large range of loads over the entire frequency band shows a comparable matching with the ideal values. As an illustration, the results at 2, 11 and 20 GHz for three loads are presented. The results obtained after using a simple calibration technique (SOL) show a sensitive improvement of the reflection coefficient measurement.

IV.6 Conclusion

At the beginning of this chapter, a brief introduction to multi-port reflectometers is given. A multi-port reflectometer is basically built on six-port junctions, which are commonly represented in two forms: one consisting of hybrid couplers and a power divider, the other one only based on hybrid couplers. We present in the second section the conception and existing examples of these two junctions. Because our main application concerns the near field microwave microscopy (NFMM) field, the working frequency of the six-port reflectometer has to cover the frequency range from 2 to 20 GHz that correspond to the operating system. However, this frequency band is too large for a

Wilkinson power divider in terms of insertion loss and isolation. Based on these considerations, the junction composed of five couplers is selected as the design basis.

In the third section of this chapter, several couplers are under investigation in terms of the working frequency. To meet our design target, the multi-section coupler in tandem structure stands out from the competition relying on its multi-octaves performance. Firstly, a conventional multi-section coupler is given and the design procedure is demonstrated. To avoid the disadvantages such as high insertion loss and low isolation especially in higher frequency, some improvement techniques are applied. These proposed methods are evaluated by means of finite element simulation by using HFSS™. After validating the design, the coupler is fabricated and characterized. The measured results show a good performance over the entire working frequency band. Since the proposed coupler is based on a multi-layer structure, to realize a six-port junction, a controlled impedance via has to be used. Thus, this interconnection is also designed, simulated, fabricated and evaluated. Once these components are characterized, we start a simulation with ADS™ to predict the performance of the six-port reflectometer. A simple calibration method (SOL) is also involved in the simulation. The results obtained demonstrate a good performance over the entire frequency band.

IV.7 References

(36 references, Classified in alphabetical order)

[AGI 13] Agilent Technologies, Inc., “Scanning Microwave Microscopy (SMM) Mode”, Datasheet, 2013.

[ANS 14] Anselmi, M., Pingue, M., Manna, A., Flamini, R., & Cosmi, L. (2014, October). Design and Realization of 3 dB hybrid stripline coupler in 0.5–18.0 GHz. In *Microwave Conference (EuMC), 2014 44th European* (pp. 464-467).

[BAU 15] Bauch, A., Hofmann, M., Nehring, J., Weigel, R., & Kissinger, D. (2015, September). A 2–30 GHz multi-octave planar microwave six-port for reflectometry applications. In *Microwave Conference (EuMC), 2015 European* (pp. 52-55).

[CRI 66] Cristal, E. G., & Young, L. (1965). Theory and tables of optimum symmetrical TEM-mode coupled-transmission-line directional couplers. *IEEE transactions on Microwave Theory and Techniques*, *13*(5), 544-558.

[ENG 77_a] Engen, G. F. (1977). The six-port reflectometer: An alternative network analyzer. *IEEE Transactions on Microwave Theory and Techniques*, *25*(12), 1075-1080.

[ENG 77_b] Engen, G. F. (1977). An improved circuit for implementing the six-port technique of microwave measurements. *IEEE Transactions on microwave theory and techniques*, *25*(12), 1080-1083.

[ENG 79] Engen, G. F., & Hoer, C. A. (1979). Thru-reflect-line: An improved technique for calibrating the dual six-port automatic network analyzer. *IEEE transactions on microwave theory and techniques*, *27*(12), 987-993.

[GHA 09] Ghannouchi, F. M., & Mohammadi, A. (2009). *The six-port technique with microwave and wireless applications*. Artech House.

[GRU 12] Gruszczynski, S., & Wincza, K. (2012). Broadband rat-race couplers with coupled-line section and impedance transformers. *IEEE Microwave and Wireless Components Letters*, *22*(1), 22-24. 1070-1074.

[HAD 06] Haddadi, K., El Aabbaoui, H., Loyez, C., Glay, D., Rolland, N., & Lasri, T. (2006, December). Wide-band 0.9 GHz to 4 GHz four-port receiver. In *Electronics, Circuits and Systems, 2006. ICECS'06. 13th IEEE International Conference on*(pp. 1316-1319).

[HAD 08] Haddadi, K., Wang, M. M., Nouri, K., Glay, D., & Lasri, T. (2008). Calibration and performance of two new ultra-wideband four-port-based systems. *IEEE Transactions on Microwave Theory and Techniques*, *56*(12), 3137-3142.

[HAD 13] Haddadi, K., & Lasri, T. (2013). Six-port-based compact and low-cost near-field 35 GHz microscopy platform for non-destructive evaluation. *NDT & E International*, *55*, 102-108.

[HAD 10] Haddadi, K., Wang, M. M., Loyez, C., Glay, D., & Lasri, T. (2010). Four-port communication receiver with digital IQ-regeneration. *IEEE Microwave and Wireless Components Letters*, *20*(1), 58-60.

[HAN 15] Hannachi, C., & Tatu, S. O. (2015, January). A new compact V-band six-port receiver for high data-rate wireless applications. In *Wireless Sensors and Sensor Networks (WiSNet), 2015 IEEE Topical Conference on* (pp. 26-28). IEEE.

[HOE 77] Hoer, C. A. (1977). A network analyzer incorporating two six-port reflectometers. *IEEE Transactions on Microwave Theory and Techniques*, *25*(12).

[HON 17] Hong, L, Zhu, J., & Li, E. (2017). A Design of Compact Microwave Six-Port Device for Ultra-Wideband Applications. *Progress In Electromagnetics Research Letters*, *65*, 57-61.

[KOE 16] Koelpin, A., Lurz, F., Linz, S., Mann, S., Will, C., & Lindner, S. (2016). Six-port based interferometry for precise radar and sensing applications. *Sensors*, *16*(10), 1556.

[KIM 04] Kim, C. S., Lim, J. S., Kim, D. J., & Ahn, D. (2004, June). A design of single and multi-section microstrip directional coupler with the high directivity. In *Microwave Symposium Digest, 2004 IEEE MTT-S International* (Vol. 3, pp. 1895-1898).

[MAN 15] Mann, S., Erhardt, S., Lindner, S., Lurz, F., Linz, S., Barbon, F., ... & Koelpin, A. (2015, January). Diode detector design for 61 GHz substrate integrated waveguide

six-port radar systems. In *Wireless Sensors and Sensor Networks (WiSNet), 2015 IEEE Topical Conference on* (pp. 44-46).

[MOL 06] Moldovan, E., Bosisio, R. G., & Wu, K. (2006). W-band multiport substrate integrated waveguide circuits. *IEEE Transactions on Microwave Theory and Techniques*, *54*(2), 625-632.

[MON 07] Mongia, R. K., Hong, J., Bhartia, P., & Bahl, I. J. (2007). *RF and microwave coupled-line circuits*. Artech house.

[OBO 14] Oborovski, A., Hofmann, M., Weigel, R., & Kissinger, D. (2014, October). Multi-octave planar microwave slot-coupled directional coupler up to 28 GHz with novel phase velocity compensation. In *Microwave Conference (EuMC), 2014 44th European* (pp. 77-80).

[QAY 14] Qayyum, S., Wei, M. D., & Negra, R. (2014, January). High dynamic-range and sensitivity six-port receiver using reactive matching technique. In *Radio and Wireless Symposium (RWS), 2014 IEEE* (pp. 19-21).

[RYT 01] Rytting, D. K. (2001, November). Network analyzer accuracy overview. In *ARFTG Conference Digest-Fall, 58th* (Vol. 40, pp. 1-13).

[SEM 06] Seman, N., & Bialkowski, M. E. (2006, May). Design of a Wideband Reflectometer for a Microwave Imaging System. In *Microwaves, Radar & Wireless Communications, 2006. MIKON 2006. International Conference on*(pp. 25-28).

[SHE 66_a] Shelton, J. P., & Mosko, J. A. (1966). Synthesis and design of wide-band equal-ripple TEM directional couplers and fixed phase shifters. *IEEE Transactions on Microwave Theory and Techniques*, *14*(10), 462-473.

[SHE 66_b] Shelton, J. P. (1966). Impedances of offset parallel-coupled strip transmission lines. *IEEE Transactions on Microwave Theory and Techniques*, *14*(1), 7-15.

[SHU 14] Shukor, N. A. M., Seman, N., & Zaidel, D. N. A. (2014, December). Wideband six-port reflectometer design formed by enhanced branch-line couplers. In *Applied Electromagnetics (APACE), 2014 IEEE Asia-Pacific Conference on* (pp. 63-66).

[TAT 13] Tatu, S. O., & Wu, K. (2013, October). Six-port technology and applications. In *Telecommunication in Modern Satellite, Cable and Broadcasting Services (TELSIKS), 2013 11th International Conference on* (Vol. 1, pp. 239-248). IEEE.

[TRE 66] Tresselt, C. P. (1966). The design and construction of broadband, high-directivity, 90-degree couplers using nonuniform line techniques. *IEEE Transactions on Microwave Theory and Techniques*, *14*(12), 647-656.

[VIN 16] Vinci, G., & Koelpin, A. (2016, January). Progress of Six-Port technology for industrial radar applications. In *Wireless Sensors and Sensor Networks (WiSNet), 2016 IEEE Topical Conference on* (pp. 48-51).

[WEI 15] Wei, M. D., Chen, Y. T., Qayyum, S., Tseng, C. H., & Negra, R. (2015, January). Wideband six-port receiver using elliptical microstrip-slot directional couplers. In *Radio and Wireless Symposium (RWS), 2015 IEEE* (pp. 10-12).

[WIL 15] Will, C., Shi, K., Lurz, F., Weigel, R., & Koelpin, A. (2015, November). Intelligent signal processing routine for instantaneous heart rate detection using a Six-Port microwave interferometer. In *Intelligent Signal Processing and Communication Systems (ISPACS), 2015 International Symposium on* (pp. 483-487).

[WIL 17] Will, C., Linz, S., Mann, S., Lurz, F., Lindner, S., Weigel, R., & Koelpin, A. (2017, January). Segmental polynomial approximation based phase error correction for precise near field displacement measurements using Six-Port microwave interferometers. In *Wireless Sensors and Sensor Networks (WiSNet), 2017 IEEE Topical Conference on* (pp. 23-25).

[YIG 12] Ge, Y., & Guo, G. (2012, May). The design of broadband stripline directional coupler. In *Millimeter Waves (GSMM), 2012 5th Global Symposium on* (pp. 307-311).

[ZHA 08] Zhang, H., Li, L., & Wu, K. (2008). Software-defined six-port radar technique for precision range measurements. *IEEE Sensors Journal*, *8*(10), 1745-1751.

General conclusion

In this PhD manuscript a homemade interferometer-based near-field microwave microscope (iNFMM) is presented and evaluated in terms of lateral resolution, in-depth resolution and measurement precision. The iNFMM is also exploited for different kinds of applications in the field of microwave imaging and characterization.

The NFMM state of art is briefly described in the first chapter where the measurement principle, typical features and classical NFMM set-ups can be found. Concerning the measurement principle, it is based on the understanding of the electromagnetic interaction between the sample under test and the evanescent microwave probe (EMP). This interaction is evaluated though the variation of material properties such as for example impedance, dielectric constant, conductivity and dopant intensity from the calibrated values. Thus, different kinds of materials can be characterized. Moreover, thanks to the penetration ability of microwaves, the subsurface properties can also be extracted, which is considered as a major advantage of the NFMM compared to the other characterization means. After talking about the advantages of NFMM, some limitations in terms of the measurement noise and microwave source signal drift are discussed. The measurement noise is mainly related to the setting parameters of the system and the measurement environment. The microwave source signal drift is generally evaluated as a function of the measurement duration. To overcome these two limitations, a careful study on setting parameters is achieved. After that, a classical NFMM set-up is under investigation. All the components including the signal generation system, the scanner and the data acquisition part are illustrated. Then, to address the sensitivity limitation, two of the most popular matching networks are described in details. Finally, we show that according to various types of probes, different applications at selected operating frequencies can be achieved.

In the second chapter, a homemade interferometer-based NFMM is briefly presented. The reason to choose the IBMN is due to its ability to efficiently adjust the electromagnetic coupling between the probe and the sample under test to guarantee a high sensitivity in a broad frequency band and bypass the frequency limitation brought by the resonator based

matching networks. The evaluation of the interferometric technique is then carried out both in Keysight™/ADS™ environment and experimentally. In the selected frequency band [2-18 GHz], a Q factor around 10000 can be achieved, which can be seen as a perfect match between the EMP and the sample. In addition, a measurement repeatability study is performed to figure out the measurement noise and microwave source signal drift during the measurement. The surface evaluation of a sample is also presented in this chapter. The measurement precision is firstly estimated by characterizing the width of a gold line that is deposited on a high impedance silicon substrate. With a careful choice of the setting parameters including the tip-sample distance, working frequency, probe apex and IFBW, a 100 µm wide gold line is estimated to 113 µm with an EMP whose tip apex size is 30 µm. After the measurement precision study, the lateral resolution is then performed by scanning several gold lines with different spacing between them. Keeping the same setting parameters, the lateral resolution can be evaluated from both signal magnitude and phase shift. As expected the lateral resolution depends on the combination of probe apex, tip-sample distance and working frequency. Once the 1D imaging performance is evaluated, the 2D imaging is carried out with two examples. The first one is dedicated to the imaging of an euro cent coin whose diameter is 16.25 mm. With such a large scanning surface, the scanning duration has to take about 3 hours to guarantee the image quality. Indeed, the scanning duration can be reduced with a sacrifice of image quality. The second sample is an accelerometer deposited on a silicon wafer. Using the same method, this device is also imaged. However, in both cases the existing sample tilt and measurement noise blurry the obtained images and decrease the image quality. To correct this distortion, an algorithm based on an implementation of local regression and local likelihood models is applied on the images and finally improves their quality. As an outstanding merit, our iNFMM is also able to perform a subsurface evaluation. For this demonstration, we have deposited a photoresist layer with different thicknesses from 2 to 12 µm on the accelerometer to estimate our iNFMM subsurface imaging ability. When the setting parameters such as stand-off distance, working frequency, probe apex and IFBW are fixed, the 1D and 2D imaging results are carried out. It is clearly shown that the thickness of the cover impacts both the measurement sensitivity and the contour details. In fact, the in-depth resolution of our system depends on the setting parameters, the cover physical property and the tip apex

size. In our case, even with the 12 μm cover, our iNFMM is still able to image correctly the subsurface device by using a 30 μm EMP.

As previously mentioned, our iNFMM has an extremely high measurement sensitivity thanks to the adjustable Q factor provided by the interferometer-based matching network. This gives us a chance for its implementation in a large range of applications. For example in the biology field, our system is able to realize the identification of different components in the solution. For demonstration, the measurement of glucose concentration in blood is given. According to the fact that different glucose concentrations in blood lead to a small variation of the blood complex permittivity, the measurement can be realized by estimating small complex permittivity variation with our iNFMM. To prove the feasibility of this assumption, first of all, a well-established first order Debye model to determine the complex permittivity of different concentrations of glucose aqueous solutions is presented in chapter III. Afterwards, based on the data collected from the first order Debye model and our system, electromagnetic simulations are realized by HFSS™ with different configurations for two different modes: immersion mode and non-contact mode. The characterization of the glucose concentration in immersion mode is demonstrated from the measurement of glucose concentrations from 0 to 10 mg/ml, whereas the glucose concentration ranging from 0 to 3 mg/ml is studied for the non-contact mode. Finally a comparison of the two modes is given in terms of the measurement sensitivity.

After demonstrating the different measurement possibilities offered by our iNFMM, a route is proposed to further improve the system in terms of integration in chapter IV, which is related to the replacement of the conventional network analyzer by a six-port reflectometer. In fact, the iNFMM equipped with a conventional network analyzer for the signal generation and measurement is very expensive and takes a large space. To decrease the cost of the system and for integration consideration, a six-port technique can be therefore envisaged. In our case, a six-port reflectometer topology with only five couplers is chosen as a design basis. With a careful design of the coupler, a six-port reflectometer operating from 2 to 20 GHz can be achieved. Simulation results together with a simple calibration technique prove its feasibility.

As a conclusion, the interferometer-based near-field microwave microscope proposed in this manuscript is able to perform a broadband local characterization of materials with a very high sensitivity. Applications such as surface/subsurface imaging, sample physical properties measurement and non-destructive characterization are performed and tracks for a further improvement of this system are given.

Perspectives

Concerning the perspectives of this study, several ideas are considered interesting to be evaluated and potentially helpful for a further improvement of the homemade iNFMM.

The first idea is related to the continuous effort for the integration of the iNFMM. As introduced in chapter IV, the replacement of the conventional network analyzer by a six-port reflectometer is a route to consider to decrease the system cost and volume. In fact, the reduction of system volume and cost can be achieved by decreasing each component cost and volume. For example, the interferometer-based matching network in our system is now constructed by individual components including a broadband phase shifter and an attenuator. Benefitting from the advanced integrated circuits technique, these two elements can be integrated together in one PCB card and the adjustment of the system could be done automatically. For a further integration of the system, the requirements of the targeted applications have to be considered. For example, thanks to the large scanning surface provided by the high precision motorized XYZ stage, the large surface imaging applications can be realized. However, this advantage is not useful for applications such as for example the local characterization of 2D material. Thus, in this case the size of the scanning element can be reduced. According to the proposed integration method, a small and relatively low-cost iNFMM can be therefore realized.

The second perspective is linked to the performance improvement of our homemade iNFMM. In fact, this system is a homemade one which is designed to prove the potentialities of the combination of an interferometer-based matching network and the near-field microwave microscope. For design complexity consideration, as mentioned in the chapter I, one limitation of our homemade iNFMM is the lack of a feedback system. This means the distance between the sample and EMP cannot be kept constant with a high precision during the scanning and the probe has a chance to touch the sample surface if precautions are not taken, resulting in a probe/sample damage. Obviously, a feedback system will contribute in a large extent to the improvement of the system performance. After talking about the integration of the feedback system, specific probes, such as hybrid and quadaxial probes can also be implemented in our system in order to improve the

transmission efficiency and remove the effect of the coaxial shields. These two ideas are considered useful for the performance improvement of our iNFMM.

The last perspective focuses on novel applications of our iNFMM. As demonstrated in this PhD manuscript, surface/subsurface imaging and dielectric characterization are applications for which the iNFMM is a power tool thanks to its high sensitivity. Beside these two applications, the system could be advantageously used for other purposes like thermal imaging (thermography) of devices and components. In fact, the advance in microelectronics including the miniaturization, integration and increased switching speeds of electronic devices has led to a great performance improvement of the modern electronic devices. However, it also brings some issues such as the localized heating, electromagnetic interference and compatibility. To solve these problems, the study of heat dissipation and the monitoring of heat production are of great importance in validating the thermal design of the device. Compared to the traditional infrared imaging technique which is limited in spatial resolution (100 μm) and sensitivity (0.1 k), our iNFMM system could be able to further improve these two specifications with its high resolution and measurement sensitivity. The conception of the thermal imaging would be based on the fact that the material property (impedance or dielectric constant) varies with temperature. The small change of impedance will then influence the reflection coefficient compared to the calibrated value. In this case, a small thermal variation leading to a property change can be detected and the thermal characterization of devices becomes therefore possible.

List of publications

Journal:

T. Lin, Gu, S, & Lasri, T. Highly sensitive characterization of glucose aqueous solution with low concentration: application to broadband dielectric spectroscopy. *Sensors and Actuators A: Physical*, *267*, 318-326. 2017.

S. Gu, Zhou, X, **T. Lin**., Happy, H., & Lasri, T. Broadband non-contact characterization of epitaxial graphene by near-field microwave microscopy. *Nanotechnology*, *28*(33), 335702. 2017.

S. Gu, **T. Lin** and T. Lasri, "Dielectric properties characterization of saline solutions by near-field microwave microscopy", Meas. Sci. Technol. vol. 28, 014014, 2017.

S. Gu, **T. Lin** and T. Lasri, "Broadband dielectric characterization of aqueous saline solutions by an interferometer-based microwave microscope", Appl. Phys. Lett. vol. 108, 242903, 2016.

International conference:

T. Lin, Gu, S., & Lasri, T. 2-20 GHz non-uniform coupler for six-port reflectometer. In *Wireless Sensors and Sensor Networks (WiSNet), 2017 IEEE Topical Conference on* (pp. 15-18). IEEE. Phoenix, USA, January. 2017.

T. Lin , S. Gu and T. Lasri, "Experimental Investigation of the Lateral Resolution of a Homemade Near Field Microwave Microscope", 47th European Microwave Conference (EuMC), Nuremberg, Germany, September.2017.

S. Gu, **T. Lin** and T. Lasri, "Spatial resolution enhancement of near field microwave microscope", 46th European Microwave Conference (EuMC), London, UK, October. 2016.

S. Gu, **T. Lin** and T. Lasri, "Materials Characterization by Near-field Scanning Microwave Microscopy", 37th Progress in Electromagnetics Research Symposium (PIERS), pp. 1474-1475, Shanghai, China, August. 2016.

S. Gu, **T. Lin**, K. Haddadi and T. Lasri, "Saline Solutions Characterization by Near-field Microwave Microscopy", International Conference on Electromagnetic Wave Interaction with Water and Moist Substances (ISEMA), pp.51-57, Florence, Italy, May, 2016.

National conference:

T. Lin, S. Gu, and T. Lasri, "Conception et simulation d'un réflectomètre six-port ultra large bande", 19èmes Journées Nationales du Réseau Doctoral en Micro-Nanoélectronique (JNRDM), Bordeaux, France, May 2016.

ABSTRACT

Near-field microwave microscopes, which belong to the local scanning probe microscopes family, are considered today as advanced characterization tools in many applications areas including physics, biology and micro and nanotechnologies. The near-field microwave microscope that is used in the work and described in this manuscript is an instrument developed at IEMN owning a great sensitivity in a wide operating frequency band [2-18 GHz]. The potential of the microscope in terms of applications is demonstrated through the characterization of liquids with different modalities of characterization (probe in contact, non-contact and immersed in a liquid). In particular, this instrument is investigated for dielectric spectroscopy of aqueous glucose solutions.

This characterization tool that offers sub-wavelength imaging capability is also tested in different situations (surface and subsurface imaging). Imaging resolution and measurement accuracy are evaluated and easily implementable processing methods are proposed to improve the quality of imaging. Finally, a solution towards a larger compactness of the instrument is investigated through the replacement of the network analyzer by a more compact device (six-port reflectometer type).

Key words: near-field microwave microscopy, evanescent microwaves, interferometry, microwave imaging, signal processing methods, aqueous glucose solutions, complex permittivity, six-port reflectometer.

TITLE IN FRENCH:

Imagerie micro-onde et caractérisation diélectrique locale de matériaux à l'aide d'un microscope hyperfréquence à champ proche basé sur un procédé d'interférométrie

RESUME

La microscopie champ proche micro-onde, qui fait partie de la famille des microscopies à sonde locale, est envisagée aujourd'hui dans de nombreux domaines d'applications de la physique, de la biologie et des micro et nanotechnologies. Dans ce manuscrit, le microscope micro-onde à champ proche qui est exploité est un instrument développé au laboratoire IEMN bénéficiant d'une grande sensibilité dans une large bande de fréquences de travail [2-18 GHz]. Le potentiel d'applications du microscope est démontré au travers de la caractérisation de liquides avec différentes modalités de caractérisation (sonde en contact, sans contact et en immersion). En particulier, cet outil est mis en œuvre pour la spectroscopie diélectrique de solutions aqueuses de glucose.

Cet instrument qui offre une capacité d'imagerie sub-longueur d'onde est également testé pour différentes situations (imagerie de surface et de sub-surface). La résolution d'imagerie ainsi que la précision de mesure sont évaluées puis des méthodes de traitement d'images simples sont proposées pour améliorer la qualité de l'imagerie. Enfin, une piste pour une intégration plus grande de l'instrument, qui consisterait à remplacer l'analyseur de réseau par un dispositif plus compact (type réflectomètre six-ports) est explorée.

Mots clés: microscopie champ proche micro-ondes, ondes évanescentes, interférométrie, imagerie micro-onde, méthodes de traitement du signal, solutions aqueuses de glucose, permittivité complexe, réflectomètre six-port.